MULTI-SCALE CFD SIMULATIONS OF MOMENTUM AND BUOYANCY DRIVEN FLOWS IN NUCLEAR REACTOR SYSTEMS

A Dissertation

by

FATIH SINAN SARIKURT

Submitted to the Office of Graduate and Professional Studies of
Texas A&M University
in partial fulfillment of the requirements for the degree of

DOCTOR OF PHILOSOPHY

Chair of Committee,	Yassin A. Hassan
Committee Members,	Elia Merzari
	Maria D. King
	William H. Marlow
Head of Department,	Yassin A. Hassan

August 2017

Major Subject: Nuclear Engineering

ABSTRACT

The present study focuses on the validation of the multi-scale CFD simulations for the nuclear systems. It is mainly divided into the three applications; First is the validation analysis of the large scale PANDA experiment for the containment safety, Second is mainly focused on the international benchmark project GEMIX in order to quantify the level of the involved uncertainty in CFD simulations, due to the turbulence modeling, and third is the validation study for the PWR 5x5 bundle with mixing vane to investigate and validate flow structures at the downstream of the mixing vane.

The first part of the work being proposed is to conduct further analysis on the containment safety by using available scale resolved modeling such as LES. In addition to the scale-resolved simulation, available data reduction techniques such as Proper Orthogonal Decomposition is applied to extract coherent turbulent structures in the flow.

The second part, in order to quantify the level of the involved uncertainty in CFD simulations, benchmark activities have been conducted by various groups at different scales. The GEMIX test facility was used to develop benchmark data. The facility involves the mixing of two fluids that are initially separated. One of the two streams is water with sugar dissolved and other stream is distilled water, which produces density differences between the two streams. Velocity fields and concentration measurements were acquired. The velocity fields were acquired using PIV and concentrations of each fluid were acquired using LIF. The activity provided the opportunity to quantify the validation study for CFD.

The third part, the single-phase hydraulic problem presented involves the steady-state turbulent flow field modelling and resolution around a scaled PWR mixing vane grid tested by Texas A&M University. The most vital contribution of this part will be the contribution to the literature with high resolution direct 3-D experimental and computational results comparison. Additionally, validated numerical results is processed to create higher order turbulent statistics database to help turbulence modeling for the sub-channel analysis and contribute to further verification and validation studies. POD and DMD techniques are used to extract coherent turbulent structures numerically.

ACKNOWLEDGEMENTS

The author would like to acknowledge the support of author's committee: Dr. Hassan, Dr. King, Dr. Merzari, Dr. Pointer and Dr. Marlow. The author would like to thank the committee chair, Yassin A. Hasan, for his continual support, patience and guidance through the research described here.

This research is supported by Department of Nuclear Engineering at Texas A&M University. The authors acknowledge the Texas A&M Supercomputing Facility (sc.tamu.edu) for providing computing resources useful in conducting the research reported in this paper. The author would like to acknowledge the PSI and OED/NEA for the valuable experimental data. The Author would like to thank Dr. Thien Nguyen and Carlos E. Perez for the 5x5 PWR Bundle Experimental data.

CONTRIBUTORS AND FUNDING SOURCES

Contributors

Part 1, faculty committee recognition

This work was supervised by a dissertation committee consisting of Professor Yassin Hassan as advisor and chair and Professor William H. Marlow of the Department of Nuclear Engineering and Professor Maria D. King of Mechanical Engineering, Dr. Elia Merzari of Argonne National Laboratory and Dr. W. David Pointer of Oak Ridge National Laboratory.

Part 2, student/collaborator contributions

All work for the dissertation was completed independently by the student. Experimental data was supplied by Dr. Thien Nguyen and OECD-NEA Paul Scherrer Institute.

Funding Sources

Graduate study was supported by a research assistantship from Prof. Yassin Hassan, Department of Nuclear Engineering Texas A&M University.

TABLE OF CONTENTS

Page

LIST OF FIGURES

Page

LIST OF TABLES

Page

CHAPTER I

INTRODUCTION AND LITERATURE REVIEW

Validation of CFD tools and models used in nuclear reactor safety analyses is vital. During severe accident conditions in light water cooled nuclear reactors, explosive hydrogen gas can be formed due to an oxidation reaction between high temperature zirconium cladding and steam. If the hydrogen gas is released into the containment building, it is possible that a buildup in concentration of the gas occurs to such an extent that a combustible air-hydrogen mixture forms, potentially leading to a hydrogen explosion. An example of such an event is the Three Mile Island accident in 1979. After this accident, extensive research on the mechanisms that lead to this type of accident has been done at both national and international levels. Several experimental facilities around the world have been built to investigate the hydrogen buildup and distribution such as PANDA, MISTRA, TOSQAN, THAI, PHEBUS, HDR, BMC, and HYJET [1]. Furthermore, the Fukushima Daiichi accident in 2011 showed that hydrogen mitigation is an important safety problem. The accident emphasized that more studies were necessary to ascertain what the optimal positioning of hydrogen recombiners needed to be, such that hydrogen build-up in the reactor containment building could be mitigated.

Most of the hydrogen mixing studies in the literature are experimental in nature. However, CFD is the only tool that can be used to fully realize hydrogen temporal distributions in the containment building. To this end, numerical simulations have been performed using Reynolds-averaged Navier-Stokes (RANS) models [2] [3].

Problematically for RANS based simulations, a parametric influence study by [4] showed that RANS turbulence model selection has the highest impact on the hydrogen mixing. Another problem is that most of the CFD validation attempts focused on the prediction of single quantities of interest, instead of simultaneous calculations of multiple quantities like velocity, temperature or gas concentration, which are necessary for CFD grade model validation. Thus, RANS simulations were able to predict selected variables accurately, but failed when attempts were made to predict multiple variables simultaneously [5]. In this respect, Large Eddy Simulation (LES) will help to understand flow physics better than RANS. Specifically, LES is able to predict this kind of complex flow. The reason for the complexity of the current flow problem is related to the interaction between the jet and stratified layer, which has strong anisotropy and fluctuations due to buoyancy effect. LES scale studies allows for the identification of weaknesses of the two equation models in accurately predicting the interaction between jets and stratified layers. This is due to the LES methods being able to directly simulate turbulent behavior of the investigated phenomena.

The aim of this study is to validate LES methods by comparing their numerical results with PANDA IBE-3 experimental data in the form of temporal velocity, temperature and gas concentration results. As shown in [5], LES analysis predicted erosion time worse than RANS models. Additionally, the previous studies [6, 7] showed that jet velocity profile directly impacts the temporal erosion time of the stratified layer, and it was stated that careful implementation of inlet boundary condition would solve this problem. In one other LES attempt by [8], temperature effects were not considered in the

simulation, causing a ~ 3% velocity increment over the simulation due to the density difference of the injection jet and the constant mass flow rate condition. The same study found that the LES results could also not predict the helium concentration as accurately as the RANS results.

Depending on the simulation being attempted, RANS models are known to potentially over- or under-predict turbulent flow quantities. As a result, RANS models have the potential to correctly predict the concentrations of helium during the simulation, while failing to appropriately predict velocity and temperature. However, all of these parameters may have an impact on the risk of a hydrogen explosion, and must therefore be properly predicted. Moreover, one other objective is contributing to validation studies of CFD for nuclear safety applications, specifically to investigate flow structure and the physics of turbulent mass transport. Thus, some computational techniques are applied here to investigate flow physics in more detail. Proper orthogonal decomposition method (POD) is applied to extract coherent structures. Additionally, Fast Fourier Transform (FFT) is applied to check numerical grid resolution, whether it is resolving enough scale or not. In II.1, the numerical models are briefly described. In II.2 the experimental test facility, and test details are explained, followed by CFD modeling details. In II.3, FFT, temporal experimental and numerical results are presented, followed by POD. Finally, conclusions are discussed in Chapter V. Additionally, the work of this part presented here has been published by International Journal of Heat and Mass Transfer. [9]

In second part of the study, GEMIX benchmark case is studied, the present benchmark exercise on Uncertainty Quantification (UQ) in Computational Fluid

Dynamics (CFD) constitutes the first of its kind worldwide. The main objective of this exercise is to compare and evaluate different UQ methodologies, currently used to assess the reliability of CFD simulations in the presence of several sources of uncertainties. The participants of this benchmark are free to choose the uncertainty sources (e.g. boundary conditions, turbulence model coefficients and numerical errors) and the methodology to compute uncertainty bands. The selection of numerical schemes, turbulence models and computational mesh are also left to participants' discretion. The selected test facility for the benchmark is GEMIX (GEneric MIxing eXperiment), developed at the Paul Scherrer Institute in Switzerland.

Last part of the study focuses on PWR Mixing vane, critical heat flux is a key parameter in PWR, which is driven by the departure from nucleate boiling. Power uprates are causing an increment on the produced heat and therefore heat flux from fuel rod surface. Higher heat flux results in local subcooled boiling phenomena during nominal operation. As a result, crud deposition and rod failure may happen. In PWR reactors, fuel assembly is designed as 17x17 square matrix of fuel rods, due to thin structure of the rods relative to their heights, support structures, such as spacer grid and mixing vane, are needed. However, there are pros and cons associated with adding these structures to the system. The cons include the increased pressure losses, vibrations and friction between fuel rod and support structures, while the pros include, increased support structural integrity and enhancing turbulence, and thus, heat transfer. In particular, mixing vanes, are creating strong lateral swirling flow, which increase the convective heat transfer at downstream of the vane. Additionally, they also increase mass and momentum transfer

between sub-channels, which is crucial for nuclear fuel assembly due to the nature of neutron population distribution in it as it may result in the production of higher amounts of heat in the central channels of an assembly. On the other hand, the flow structures produced by the mixing vanes are significantly complex due to their small fine structure (pin to pin pitch is about 1.26 cm and pin diameter is around 0.95 cm). Also, the structure of the mixing vanes is highly detailed with its dimples, springs and wings. In a generic PWR there are more than ten thousands sub-channels. Therefore, it is a challenging geometry for both experimental work and Computational Fluid Dynamics (CFD) simulations.

Lee and Choi [10] analyzed 17x17 bundle configuration with four different mixing vanes, they calculated the pressure drop, secondary flow intensity, and heat transfer coefficient. Their y+ value is about 200, thus they used wall function for near-wall treatment with 16.3 million cells. They compared numerical results with semi-empirical correlations with low order variables. Li and Gao [11] analyzed both 5x5 and 17x17 assembly configurations. They analyzed the effect of dividing the domain in the axial direction due to the computational limitations of considering the full domain. Their analysis shows that the secondary flow intensity is affected significantly by the bundle configuration, the 17x17 configuration results in higher secondary flow intensity than the 5x5 bundle configuration. Additionally, they compared axial and lateral velocity components with experiment and have observed significant differences between experimental and computational results, especially for the axial velocity. Zhang et al. [12] analyzed the two-phase flow with mixing vane in a single sub-channel and quantified the

effect of the mixing vane on the Departure from Nucleate Boiling (DNB). Their analysis shows the pressure drop due to mixing vane and secondary flow structures induced by mixing vane. They also tried to identify hot-spots by running simulations with conjugate heat transfer option. Their numerical grid has about 2 million hexahedral cells. Bieder et al. [13] focused on the secondary flow induced by mixing vane by comparing LES, k-epsilon and AGATE experimental results at Re=96,000. Their LES results are in relatively good agreement with their experimental results and performed better than the k-epsilon model. They used about 300 million control volumes, and their conclusion regarding turbulence modeling is that the k-epsilon and the LES results are very similar near mixing vane due to dominant inertia forces, thus they recommended the investigation of turbulence modeling sensitivity to test further downstream of the mixing vane. Kang and Hassan [14] analyzed round robin benchmark case comprehensively including sensitivity of the mesh type. Their results at downstream of the spacer grid are in a relatively good agreement with experimental results for the velocity components, while it is not the case at the downstream of the mixing vane. On the other hand, they concluded that the mesh type has more effect on the results than the turbulence modeling, STAR-CCM+'s trimmer mesh models performed best in their analysis, which is the same tool that is used in this study. Chen et al. [15] conducted a research based on the sensitivity of the fuel matrix configuration by investigating the secondary flow intensity and pressure drop. Also they compared different RANS modeling versus experimental results. Lastly, they did their mesh sensitivity analysis on the different geometric parts of the mixing vane independently. Cheng et al. [16] analyzed the mixing vane by using multi-grid with a

maximum of 11 million volume elements, and they compared their simulation results against a previous experimental study, their results are not in a good agreement with experimental results, which proves the challenge of the present geometry.

Hence, 3-D CFD simulations is a must to enhance analysis capability for multi-physics coupled simulations and thus, CFD codes need comprehensive validation, especially for highly detailed mixing vane geometry. Thus extensive benchmarking with experimental results has to be done. The purpose of this chapter is to show the results obtained from the CFD calculations and their benchmarking to the experimental results observed at Texas A&M 5x5 PWR fuel bundle experimental facility using Particle Image Velocimetry (PIV) techniques. In order to perform simulation LES turbulence modeling is chosen to reduce modeling uncertainty off the two equations models. The flow is strongly anisotropic at the mixing vane downstream. In order to confirm grid resolution, Fast Fourier Transform is applied at different points in the domain to check inertial subrange. Also, before running the main simulation, the fully developed profile is obtained from time-averaged LES simulation. Proper orthogonal decomposition (POD) and Dynamic mode decomposition (DMD) techniques are applied to extract coherent turbulent structures. Additionally, standard k-epsilon modeling results and experimental results are compared quantitatively and qualitatively. All of the simulations is performed with CD-Adapco Star-CCM+ CFD code and main LES simulation has about 0.4 billion volume elements.

CHAPTER II

LARGE EDDY SIMULATIONS OF EROSION OF A STRATIFIED LAYER BY A BUOYANT JET[*]

II.1 Numerical Models

In the PANDA experiment, there are two complex flow phenomena. The first is a turbulent buoyancy-momentum driven jet and the second is the interaction of the jet and stratified layer. To model this complex flow behavior, the LES technique is used. LES directly solves the large scales of motion in a turbulent flow, while the smaller scales are modelled. Solving larger scales directly and modelling smaller scales allow for significantly less uncertainty than conventional RANS modelling, since the modelling of the smaller scales is based on the hypothesis that smaller eddies are self-similar and thus they can easily modelled due to its universal structure independent from flow geometry. In the current study, the Energy and Species Transport equation are solved as well due to the temperature variation of the gas mixture and mixing of the two different gases. The density is computed by using the ideal gas law with and the temperature computed using the energy equation. Buoyancy is accounted for in the current study due to the variable density at the stratified layer. In II.1.1, the Multi-Species Transport Equation is detailed, while the turbulence modelling details are explained in II.1.2.

---

[*] Reprinted with permission from "Large eddy simulations of erosion of a stratified layer by a buoyant jet", by F.S. Sarikurt, Y.A. Hassan, 2017, International Journal of Heat and Mass Transfer, Volume 112 354-365, Copyright 2017 Elsevier Ltd.

II.1.1 Multi-Species Transport Equation

The transport equation for the mass fraction Y_i of the i^{th}species is solved as in Eq. 1

$$\frac{\partial \rho\, Y_i}{\partial t} + \nabla.(\rho u\, Y_i) = \nabla.(\rho D_{i,m} \nabla\, Y_i \; + \; \alpha_t \nabla\, Y_i) \tag{1}$$

where D_m is the molecular diffusivity calculated using the Chapman-Enskog model Eq. 2. The diffusion coefficient for molecular diffusivity used is $7\text{x}10^{-5}\,\frac{m^2}{s}$, α_t is the turbulent diffusivity, and ρ is the density.

$$\mathrm{D}_{1,2} = \frac{1.858\text{x}10^{-3} T^{3/2}}{p\sigma^2{}_{12}\Omega} \sqrt{\frac{1}{M_1} + \frac{1}{M_2}} \tag{2}$$

where M_1, M_2 are the molecular masses of the gas components, p is the pressure, T is the temperature, σ^2 is the average collision parameter and Ω is the temperature dependent collision integral. The diffusion coefficient for helium and air mixture is $7\text{x}10^{-5}\,\frac{m^2}{s}$ at T=298 K and p= 1 atm.

II.1.2 Turbulence Modeling

CFD applications have commonly been used for turbulent flow in the last three decades. Although there are several turbulent models available, including hybrid variations, a general purpose turbulence model has not been developed yet. Each model has its own specific advantages or disadvantages according to the flow structures. Although the turbulent flow can be resolved directly by solving the Navier-Stokes equations, Direct Numerical Simulation (DNS) it is not feasible for current engineering problems due to its significant computational cost. As a compromise between accuracy and computational cost, turbulence models have been developed. Large Eddy Simulation (LES) and Reynolds-Averaged Navier-Stokes (RANS) are used extensively for most of the current engineering problems.

In the present study, LES is used to investigate its capability for a containment level safety analysis As a sub-grid scale (SGS) model, the Dynamic Smagorinsky model is used in STAR-CCM+ 10.06 [17].

The turbulent viscosity in the Dynamic Smagorinsky SGS model is defined as in Eq.3

$$\mu_t = \rho \Delta^2 S \tag{3}$$

where;

$$\Delta^2 = C_s^2 V^{2/3} \tag{4}$$

The difference between the Dynamic Smagorinsky and the Standard Smagorinsky version is that C_s is not constant and it is computed dynamically as a function of test-filtered variables to achieve a more global SGS model. Further details about dynamic SGS modelling can be found in [18].

II.1.3 Proper Orthogonal Decomposition

The POD algorithm to investigate coherent structures in turbulent flows was first proposed by Lumley [19] . The methodology is based on extracting an orthogonal set of spatial eigenfunctions from the random field. The main goal of POD is to find the optimal representation of the field by solving a Fredholm integral eigenvalue problem given in Eq.5.

$$\int R(x,x')\phi(x')dx' = \lambda\phi(x) \tag{5}$$

However, the direct solution of this problem is computationally expensive. Sirovich [20] proposes a solution to this problem, which is known as the Method of Snapshots. The method considers a set of M linearly independent flow realizations. Applying the method of snapshots results in following equation.

$$RA = \Lambda A \tag{6}$$

where A is a matrix that includes mode coefficients, Λ is a diagonal matrix with eigenvalues on the diagonal, and R is the temporal correlation matrix, which includes M

number of the flow field data. The flow field can be decomposed into a set of eigenfunctions and mode coefficients:

$$u(x, y, t_i) \approx \sum_{k=1}^{M} a_k(t_i)\, \sigma_k(x, y) \tag{7}$$

where a_k is mode coefficient and σ_k is spatial eigenfunction. In the present study, snapshots were extracted at every time step between 600 s and 620 sec. Total 8000 snapshots are collected and they are processed with a MATLAB script.

II.2 Experiment and CFD Modeling

II.2.1 Experiment

The main purpose of the experiment is investigating the erosion of a stratified layer, which is a possible post-accident scenario after a LOCA as a result of hydrogen leakage into the containment. Helium gas was used instead of hydrogen for safety reasons. At the beginning of the experiment, only helium was injected into the vessel to form a stable stratified layer. This process helped to create a helium-rich layer at the upper region of the vessel. The rest of the vessel is dominated by air. The stable layer means that the distribution of the gases is in balance due to the balance of natural forces, which are the gravity and buoyancy forces. Axial molar fractions of the gas mixture were measured before the start of the experiment as an initial condition and then they are imposed as in

initial conditions in the CFD simulation. The measured initial condition for gas mixture density can be seen in Figure 1.

The erosion of the stable stratified layer occurred by injection of the low momentum gas mixture into the vessel by using a circular pipe which has a 75.3 mm inside diameter. The mass flow rate of helium-air mixture was measured as 21.94 g/s during the experiment and it was kept constant. On the other hand, the temperature of the gas mixture increased during the experiment. More details of the experiment can be found in [5].

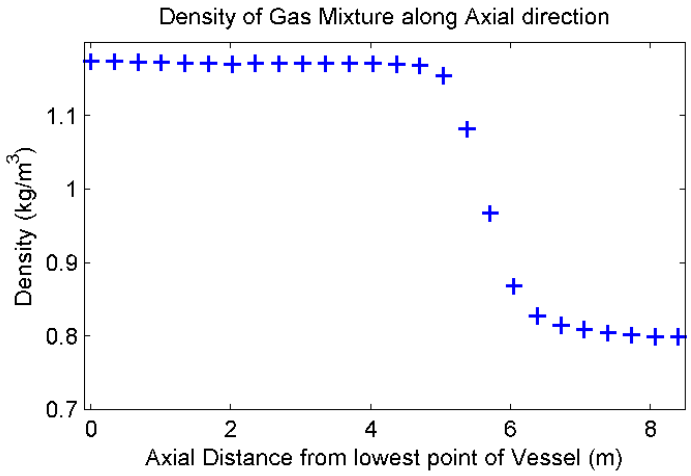

Figure 1: Initial density distribution of the gas mixture.

II.2.2 Boundary Conditions

The simulation followed the experimental boundary conditions as closely as possible. An inlet mass flow rate boundary condition was used to inject the gas mixture vertically from the bottom of the stratified layer. The parameters at the inlet boundary is calculated by using experimental data. Table I gives the details of the inlet boundary conditions.

Table I: Inlet Boundary Conditions

Air-Helium Mass Flow Rate	21.94 g/s
Air Mole Fraction	0.866
Helium Mole Fraction	0.134
Temperature	20 ^{0}C to 29.3 ^{0}C
Inlet Pipe Diameter (inner)	75.3 mm
Turbulence Intensity	7.4%
Turbulent Length Scale	2.86 mm

In the experiment, an outlet vent was used to keep constant pressure in the vessel and it was placed at the bottom of the vessel. In the CFD simulation, a pressure outlet can be used for this purpose. At the surfaces of the vessel, the no-slip wall boundary condition was applied.

The previous work [6] indicates the inlet region of the jet confined in the pipe is critical towards correct predictions of the erosion process. This is shown by the centerline velocity behavior of the jet in the previous works using RANS/LES. In order to properly account for this and to prevent large computational cost increases, we used a precursor

simulation of recycling LES to get the average profile statistics needed. Fully developed mass flux profile is obtained from independent recycling LES simulation and this profile is applied to full scale simulation without modeling the pipe region. The mesh and time averaged mass flux profile can be seen in Figure 2.

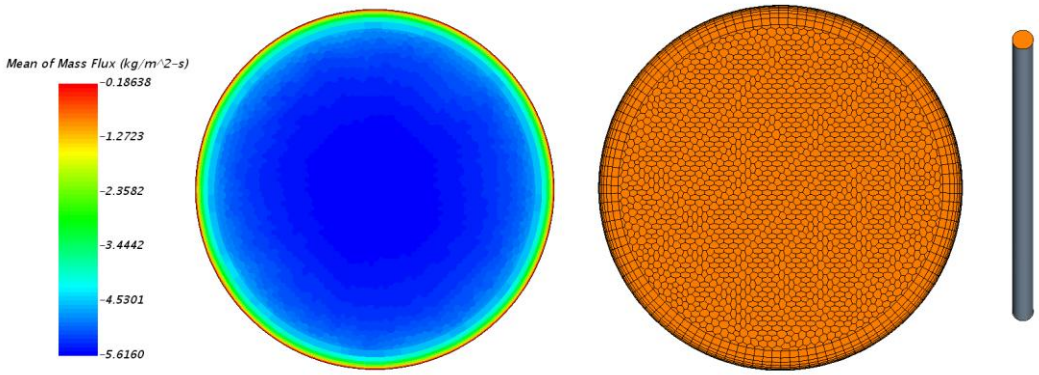

Figure 2: Averaged mass flux profile and pipe mesh.

II.2.3 Methodology of CFD

Multi-component gas modeling is used to compute the diffusion of the air-helium gas mixture. The courant number is kept about 0.5 which corresponds to a time-step of approximately 0.0025 s. All convective discretization schemes that were used are second-order in space and time. The most important modification on the CFD modeling is applied on the reference density calculation, which is used in the momentum equation to calculate the buoyancy term. The reference density is defined as constant parameter in the CFD tool, but in this study it is modified to be calculated automatically during the transient,

since the average density of the medium is changing during the transient. The other CFD modeling details are given in Table II.

Table II: CFD modeling details

Solver	Segregated Pressure-based algorithm
Pressure correction scheme	SIMPLE
Spatial discretization	Bounded-Central
Temporal discretization	2^{nd} order implicit
Time step size	0.0025 s
Equation of State	Ideal Gas
Multi-Component Gas	2^{nd} order convective
Convergence Criteria	Continuity and Momentum: 10^{-4} Energy and Mass : 10^{-5}
# of iterations per time step	20

The quality or validity of the mesh directly affects the accuracy of the numerical results. The most important factors for the quality are: skewness angle, face validity, cell quality and volume change as defined in [17]. In the present study, the geometry is not complex, which helps to sufficiently satisfy all quality criteria. The polyhedral meshing

algorithm is used to create the volume mesh. In the present study, the mesh refinements are applied along the jet axis through the interaction region of the jet and stratified layer. This is done to resolve the sharp gradient of velocity and density in this region. A plane view of the mesh and refinement regions are given in Figure 3, and Table III gives the parametric details of the mesh.

Table III: Mesh details

	Vessel	Pipe Flow
Number of cells	~ 20 Million	~2.5 Million
Cell type	Polyhedral	Polyhedral
Base Cell size	Base 30 mm Refined area 9 mm	2 mm
y+	Below 1.0	~ 1.0

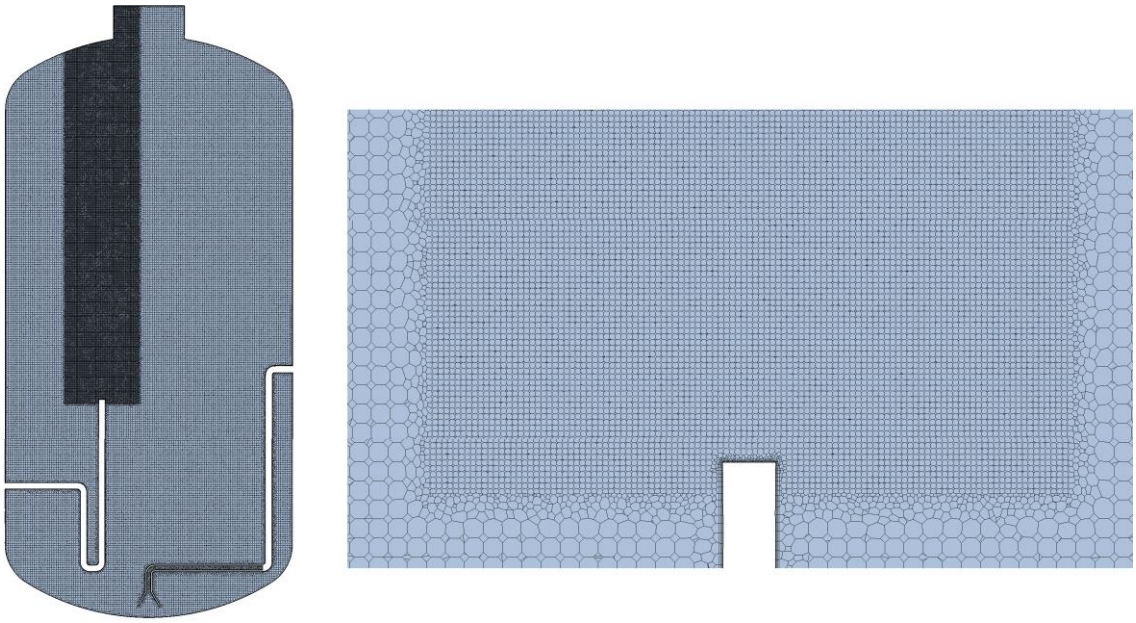

Figure 3: The plane view of the mesh and zoom to the refined area.

According to Kolmogorov's theory, there are three main regions on the turbulence spectrum. Large eddies with lower frequencies, the inertial range and dissipation range. For LES, the criteria for a grid of sufficient fineness is that it must be fine enough to resolve the inertial range to get meaningful results. Therefore, a Fast Fourier Transform (FFT) can be used to assess the numerical grid resolution by checking the turbulence spectrum. This test can be done to check for the characteristic slope (-5/3) of the inertial range according to the Kolmogorov's 5/3 theory [21]. Two points are chosen in the domain along the jet axis and axial velocity data are extracted between 600 s. and 625 s. at each time step. The first point is chosen 1.575 m above the jet and the second point is chosen to be 1.875 m above jet. According to the Kolmogorov's hypothesis, the ratio of

larger structure time scales is proportional to the Reynolds number. According to Eq. (5), it is expected to have larger time scale closer to the jet entrance.

$$\frac{t_L}{t_\eta} = Re_L^{1/2} \tag{8}$$

As shown in Figure 4, -5/3 slopes are observed and inertial subrange is resolved on grid scale. Therefore, it can be assumed that the grid resolution is sufficient. Additionally, Figure 4a shows -5/3 is on lower frequency region than Figure 4b. It is expected due to Eq.8 turbulence level is higher at Fig4a, which results in higher time-scales and lower frequency.

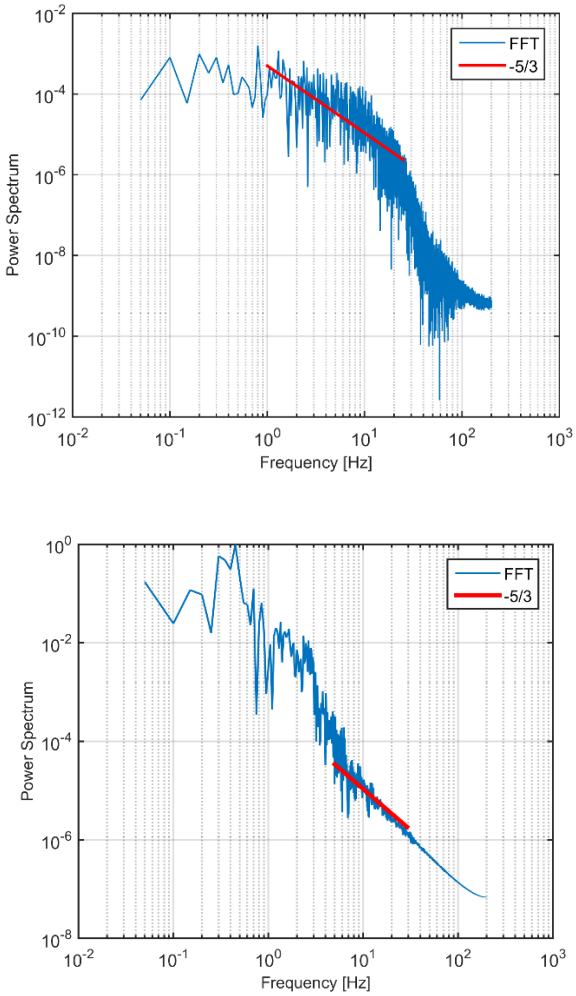

Figure 4: Fast Fourier Transform from two different points along the jet axis.

II.3 Results and Discussion

In the present study, the monitor points are created to extract the required data for comparison at the same locations at which the experimental data were recorded. The selected experimental monitor points for the present CFD study can be seen in Figure 5. This figure can be used as reference for the rest of the plots in this paper. Furthermore, visual scalar field and POD snapshots are extracted on same plane as in Figure 5.

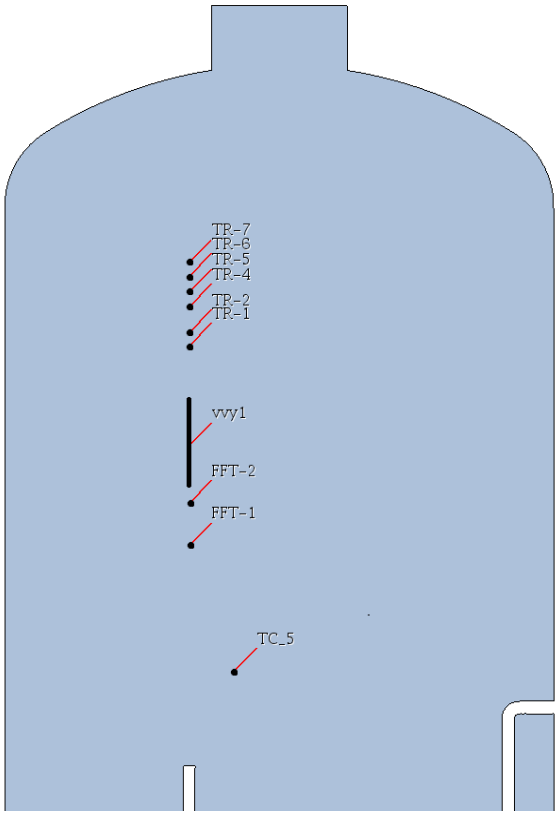

Figure 5: Monitor points and lines.

Figure 6 shows the instantaneous mole fraction of the helium-air mixture, temperature, and velocity magnitude. As the jet goes up, it interacts with stratified layer, thus the jet gradually loses its momentum due to the negative buoyancy effect. It behaves as a plume in the stratified region and cannot penetrate the layer completely due to the stronger density gradient at the higher elevation. This can be seen clearly from the helium mole fraction, and temperature results. At t=100 s. the penetration depth of the jet is deeper than at t=605 s. Since the mass transport or mixing mechanism is dominated by diffusion, it slowly erodes stratified layer over the time. Studer et al. [22] observed that the Froude (Fr) number can categorize the mixing mechanism. When Fr >> 1, the layer is eroded by global dilution, while for Fr << 1, the diffusion process erodes the layer slowly. In the present study, diffusion dominates the mixing [5]. Additionally, there is secondary effect of the jet on the mixing process, namely it causes slow diffusion above the interaction of the jet and stratified layer region.

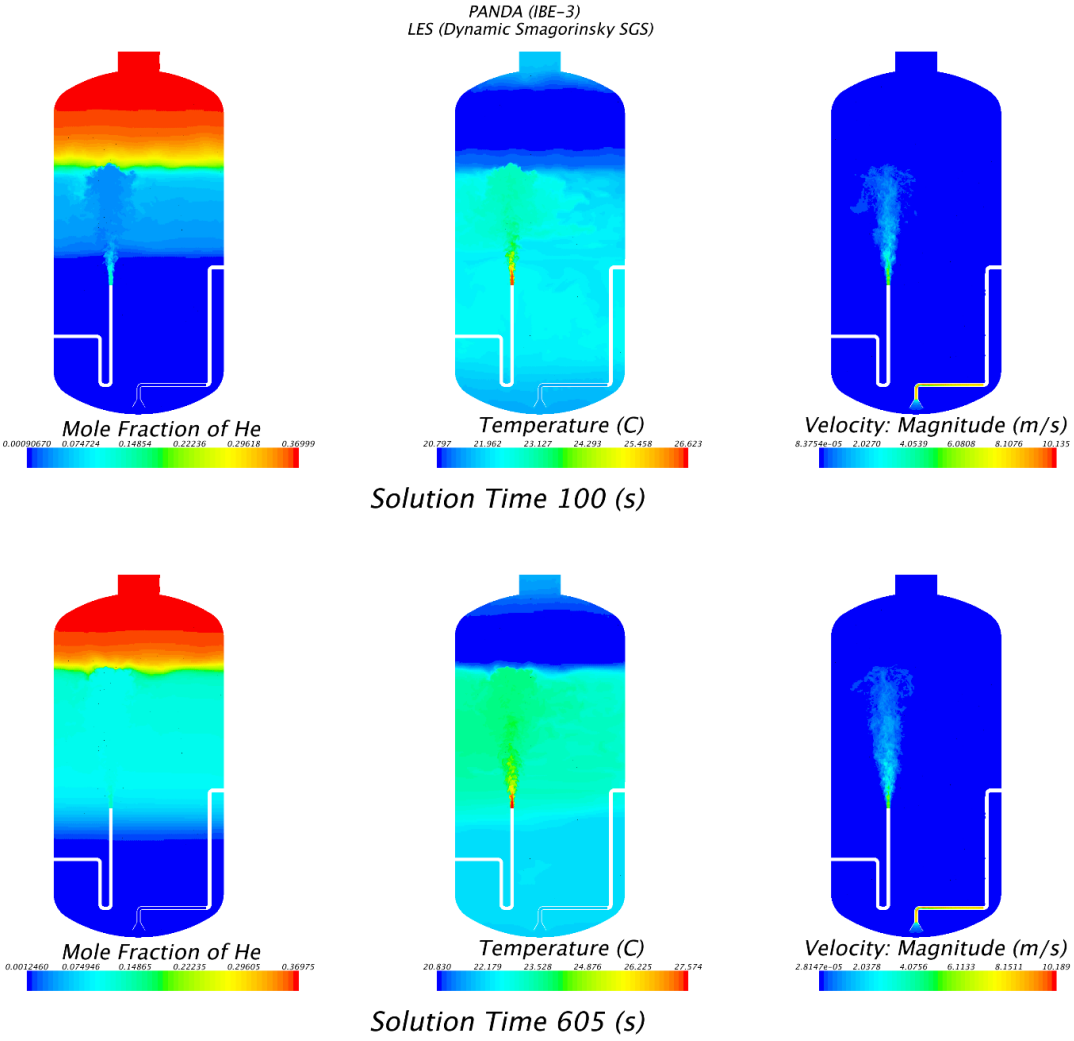

Figure 6: Instantaneous mole fraction, temperature and velocity at t=100 and 605 s.

Figure 7 shows the time histories of helium concentration at different elevations along the jet centerline. Experimental measurements were taken by mass spectroscopy with 1% error and a 226 s. sampling period. As shown in Figure 7, at the time of the erosion, there are strong fluctuations due to competition between jet momentum and buoyancy force. Once the erosion process is completed, the fluctuations disappeared as

presented in TR-1 location after t=420 s. On the other hand, at higher elevations, there are minor fluctuations due to gas diffusion and decayed fluctuation from jet interaction. Overall, the present study shows excellent agreement with the experimental gas concentration data. To the knowledge of the authors, the results presented here are the first LES results that predict all the considered parameters with reasonable agreement for a significantly long simulation time.

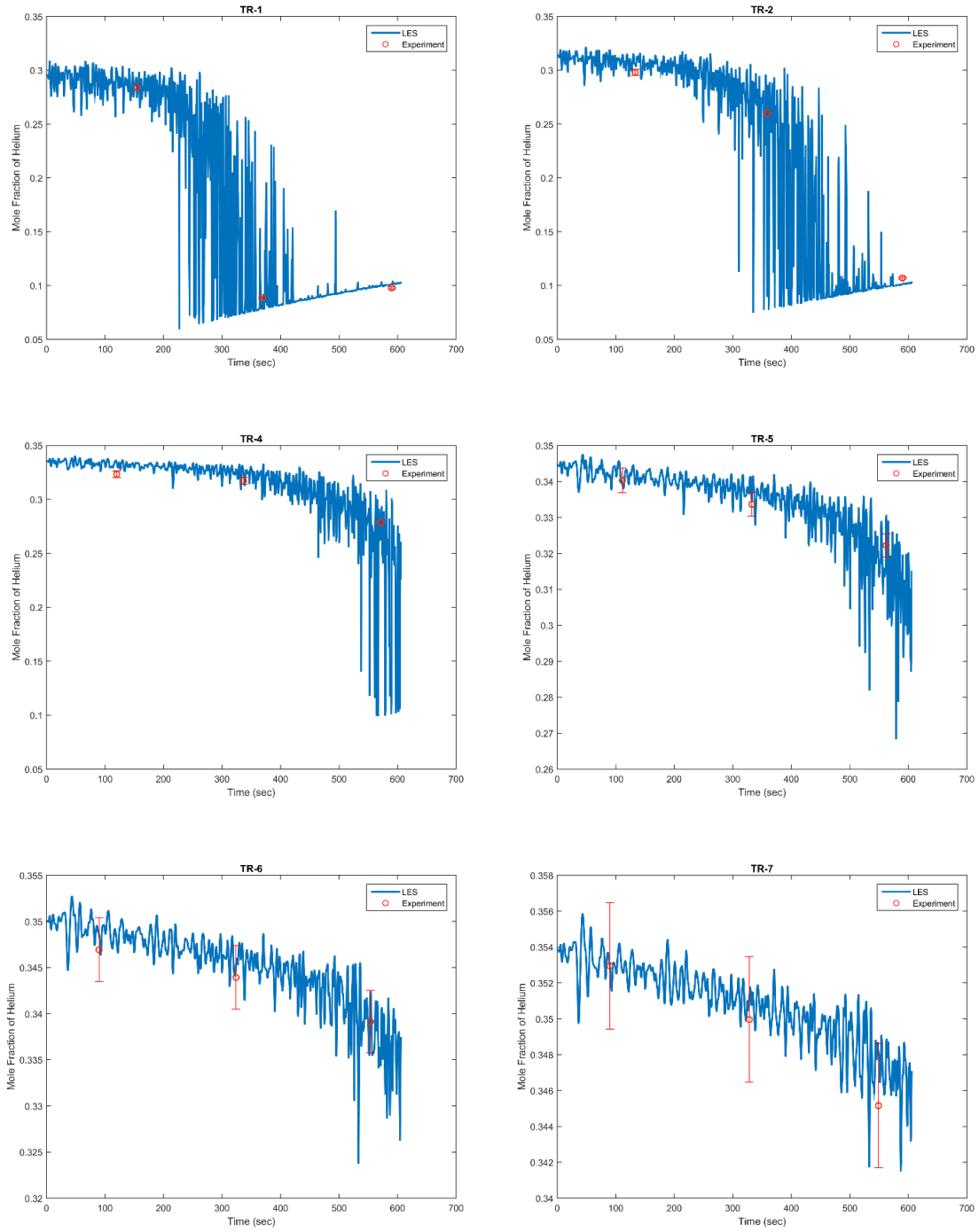

Figure 7: Mole fraction of Helium vs. Time along the jet axis to evaluate the erosion.

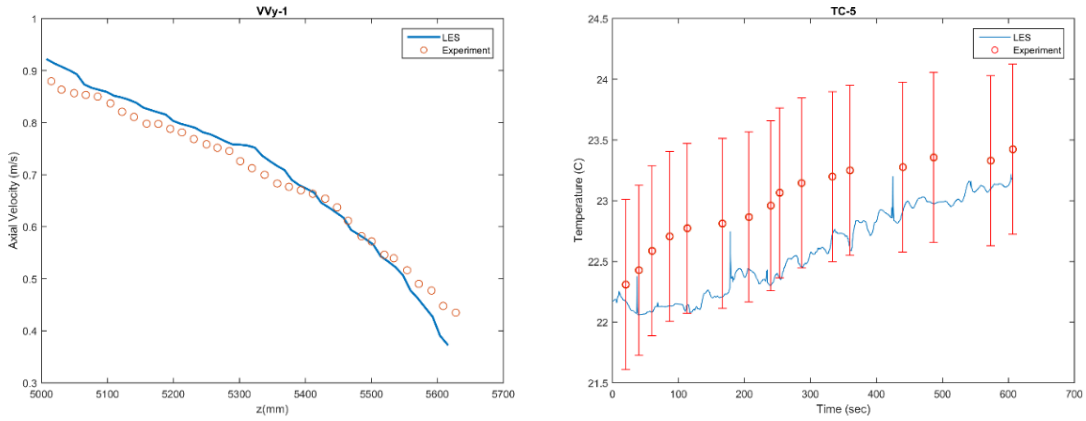

Figure 8: Time averaged axial velocity (left) and time history of temperature (right).

Since the main objective of the study is the validation of CFD for the hydrogen explosion risk situation, the hydrogen concentration is the most important factor in determining the flammability or explosion risk. In addition to concentration, the temperature and pressure affects the flammability. Thus, the LES results for temperature and velocity are compared with the data that were measured experimentally. As shown in Figure 8 (left), the axial velocities were averaged over a time period of 204 s by using PIV data. The simulation results are averaged over an equal time period. The results show good agreement with the experimental data. Figure 8 (right) shows the temporal temperature value at a single point. Even though the simulation results look like it slightly under predicts the temperature, it is still in the uncertainty range of the experiment, and both numerical simulation and experimental results follow same pattern.

II.3.1 Proper Orthogonal Decomposition

The POD modes allows for decomposing the optimal modes for the flow and capturing large-scale flow structures. In general, the first few POD modes capture 95% of the total kinetic energy. Figure 9 shows energy distribution for individual modes (left) and cumulative energy (right). Specifically, the first mode has the most significant energy, ~94%, while it drops to 0.15% in the second mode. In addition, energy per POD mode is decreasing slowly after second POD mode.

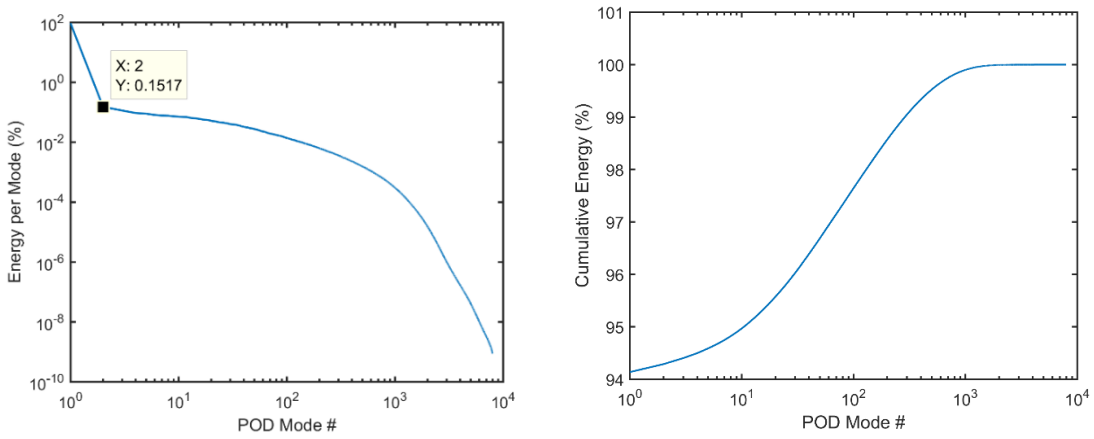

Figure 9: Energy per POD mode (left) and Cumulative Energy vs. POD mode (right)

Figure 10 shows the mole concentration of the helium by using POD snapshot method. It presents the structures of gas mixing, or in another words, turbulent mass transport. Fig.10a is the reconstructed field which is constructed by using the first three POD modes, and it represents the average mole fraction of the 8000 independent snapshots. The reconstructed field can help to understand to the turbulence mass transport,

since it clearly shows jet penetration depth and width. Figure 10 (right) shows similar trend with reconstructed field as expected due to the high-energy content of the first mode which is showing mean values. Figure 11 (left), which shows the second mode, shows interesting results. It captured the mass transport mechanism for the erosion process between the incoming jet and the stratified layer. The black boxes in Fig.10c shows the self-mixing in the stratified layer due to density gradient and fluctuations from jet-layer interactions, while white box depicts the mass transport due to jet's influence on the layer. Additionally, it shows qualitatively similar behavior with the buoyancy term, which is used as source term for turbulent kinetic energy equation of the two-equation models. This can be seen in Figure 11 (left). Further discussions about the source term can be found in [3] and [7]. Figure 11 (right) shows the third mode of the POD and it presents similar structures when compared with the second mode that shows the mixing mechanism on the stratified layer.

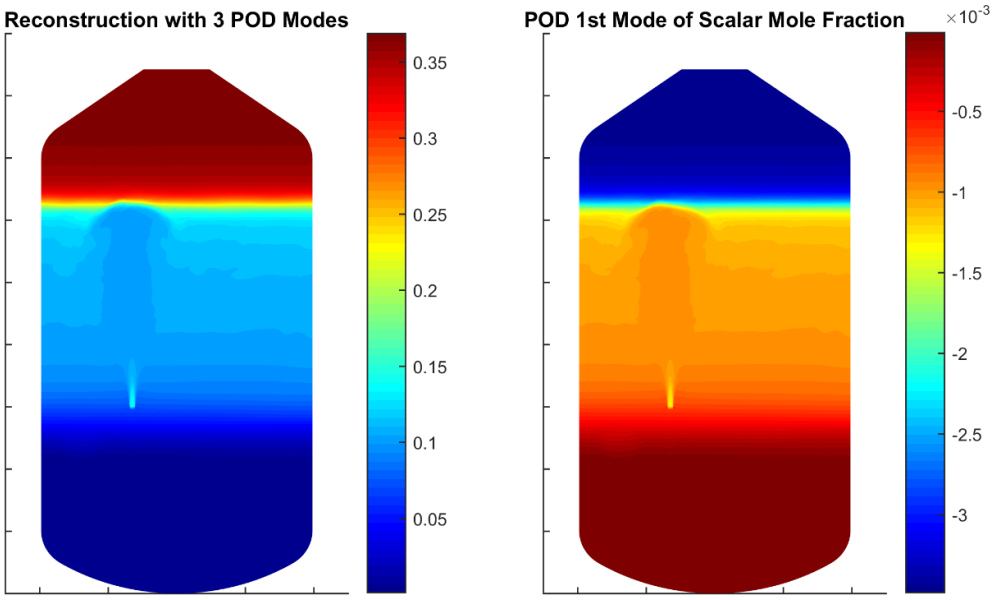

Figure 10: Helium gas concentration (scalar) POD modes

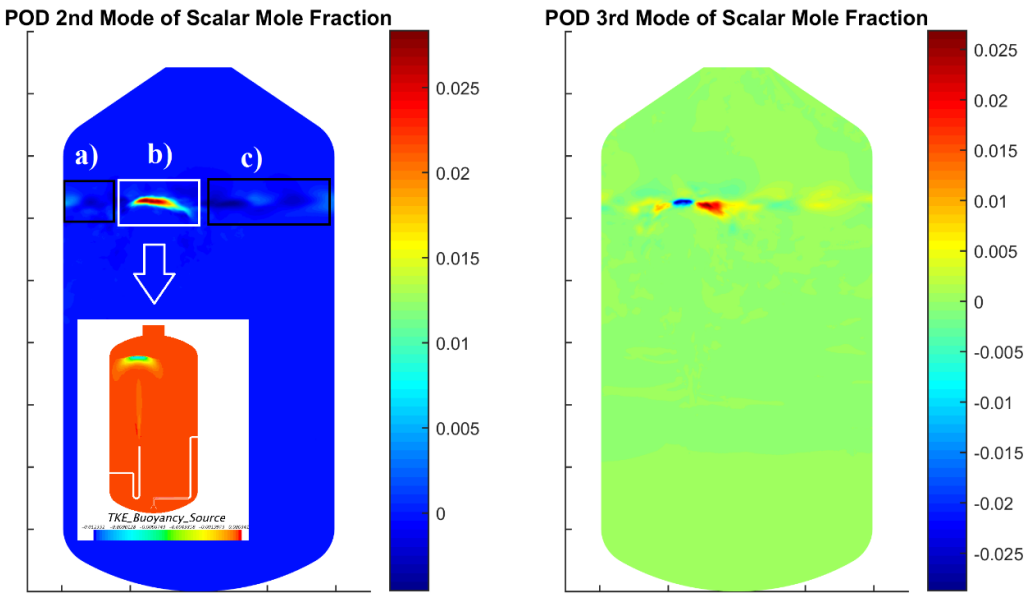

Figure 11: Helium gas concentration (scalar) POD modes

Figure 12 shows the axial (left) and lateral (right) velocity fields produced by the POD, including the reconstruction with first three modes, first mode and third mode. As seen in the scalar field before, the first mode represents the average flow field and its coherent flow structure. The Axial velocity field shows the jet flow structure and decay of the jet at the stratified layer as a turnover away from the layer to a downward direction. The third mode of the axial velocity shows the formation of a Kelvin-Helmholtz instability due to both density differences and shear layer. For the lateral velocity component, an instability structure near the jet expansion due to the density difference and backward flow from layer is observed.

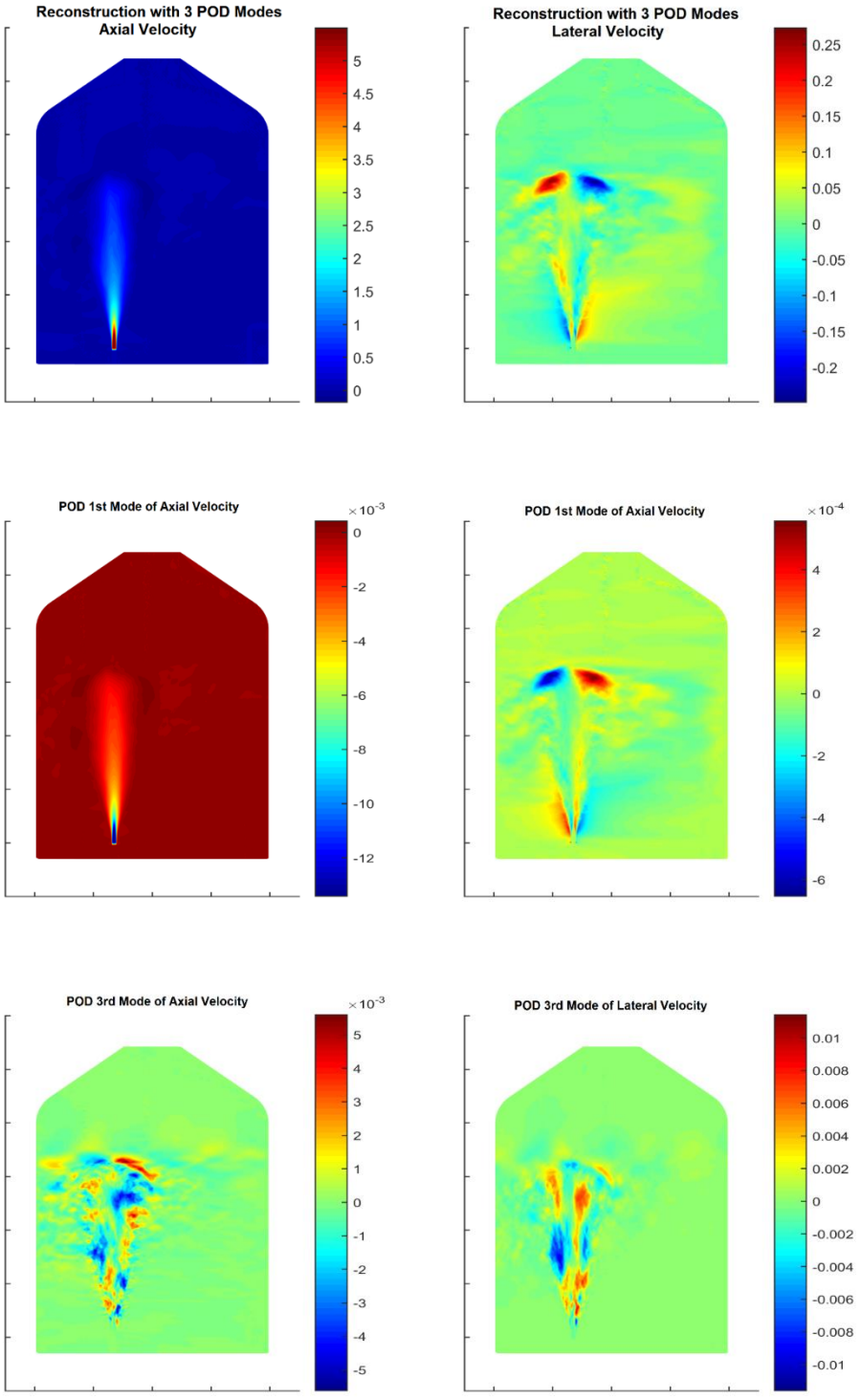

Figure 12: POD modes of axial and lateral velocity.

Vorticity on POD modes are given in Figure 13 for the first and second mode. In the first mode, one can observe that strongest vortices occurred close to the orifice due to the shear is created between incoming jet and quiescent ambient gas. In this case, a Kelvin-Helmholtz instability played a role due to both shear layer, and density difference. The second mode of vorticity shows smaller scale vortices starting from jet entrance along the downstream of the jet. As shown in the contour plot, the smaller scale vortices are more dissipative than larger scale vortices.

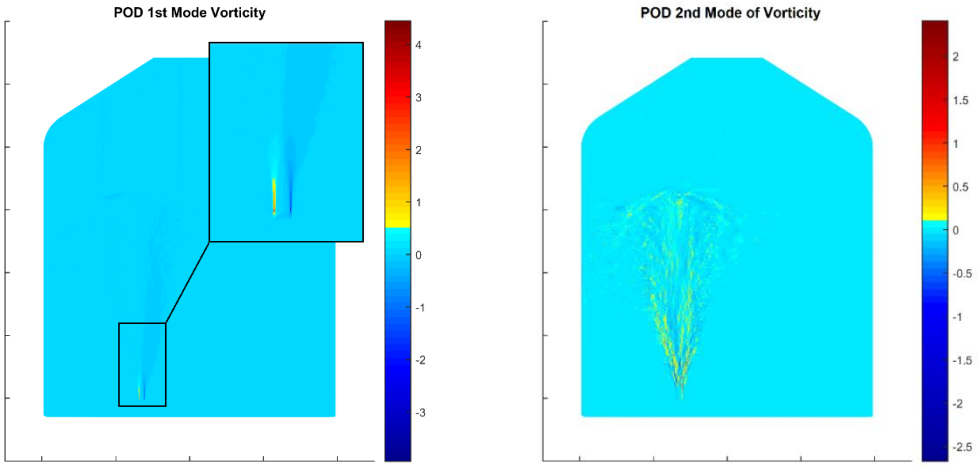

Figure 13: POD modes for Vorticity.

Vortex structures are analyzed by using Lambda2 criterion and the Q-criterion. The Lambda2 method is a detection tool to identify vortices from three-dimensional velocity. Lambda2 is defined as the second eigenvalue of the matrix $S_{ik}S_{kj} + \Omega_{ik}\Omega_{kj}$, where S_{ij} strain-rate tensor and Ω_{ij} is the spin tensor. Values of $\lambda_2 < 0$ can be interpreted

as vortex regions. [4]. The Q-criterion is similar to the Lambda2 criterion. The scalar value is defined by $Q = \frac{1}{2}(|\Omega|^2 - |S|^2)$. For positive values, the flow is vorticity-dominated, whereas a negative value indicates the flow being strain-dominated. In the previous part, strong vorticity was observed near the jet orifice from first mode of the POD. As shown in Fig. 13, horseshoe shaped structures are observed from both Lambda2 and Q-criterion isosurface plots. In the literature, similar structures are observed for buoyant jets both in experimental and numerical studies [23]. Creation steps of these vortices are discussed in details by [21]. The present study successfully reproduced the expected physical flow structure. Further investigation can be done on those vortices, which can shed light on their development in the downstream region, their lifetime before dissipation or bifurcation, and the effects on the scalar mass transport. The scale mass transport occurs by the variation of the density difference between ambient gas and jet density. Since these type of vortices are observed near wall, and here quiescent ambient gas behave similar to wall effect, which causes vortex production.

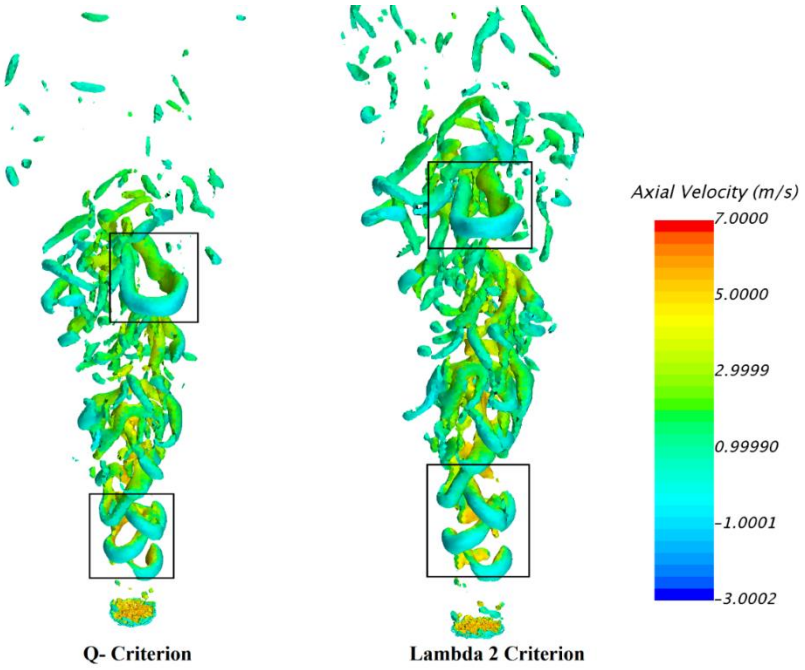

Figure 14: Instantaneous isosurfaces of buoyant jet by Q and Lambda 2 criterion.

CHAPTER III

GEMIX

III.1 Experimental Setup

The confined wake flow water mixing experiments in the GEMIX facility, focus on the basic turbulent mixing mechanisms for non-stratified and stably stratified conditions. A simplified schematics of the test rig are shown in Figure 15 and 16. The flow channel is made of acrylic glass to enable optical access, except for the last 80mm of the splitter plate, which is made of stainless steel to avoid deformation of the splitter plate tip. The main design parameters for the GEMIX flow channel are listed in Table IV. The coordinate system to describe the velocity and concentration fields is located at the tip of the splitter plate and its origin is placed in the middle of the channel. The x-coordinate represents the streamwise direction, the y-coordinate the crosswise and the z-coordinate the spanwise direction.

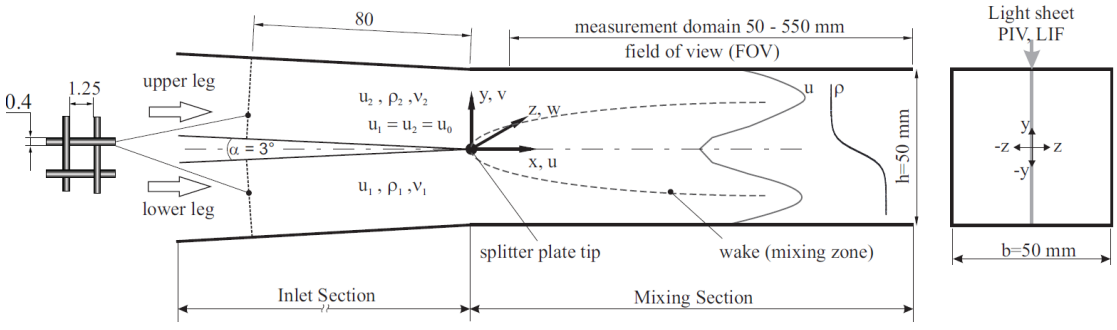

Figure 15: Schematic of the GEMIX test rig. (Reprinted from [24])

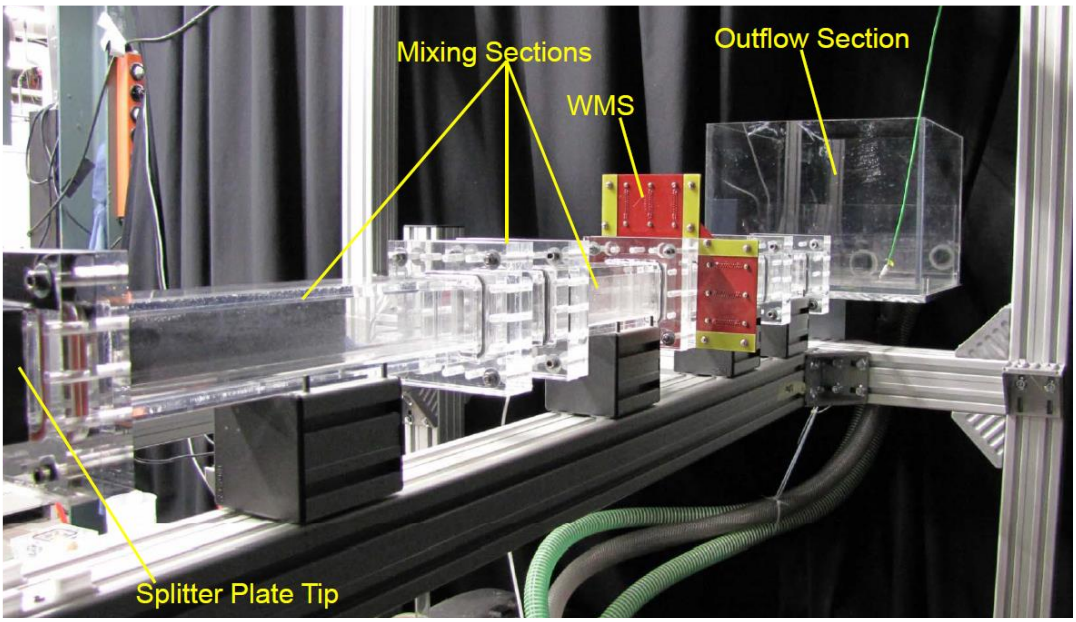

Figure 16: Experimental Mixing section. (Reprinted from [24])

Table IV: Main design parameters of the GEMIX flow channel.

Inlet section length	1250
Inlet section height × width	25×50 (2×)
Splitter plate angle	3˚
Honeycomb d = 2, l = 50	@ x = -670
1. Grid d = 1, w = 4	@ x = -520
2. Grid d = 1, w = 4	@ x = -300
3. Grid d = 0.4, w = 1.25	@ x = -80
Mixing section length	550

Table IV: Continued

Mixing section height × width	50×50
Total channel length	3000
Nominal inlet velocities	0.2-1.2 m/s
Re-Numbers in mixing section	10,000 – 60,000
Volumetric flow rate	15 – 90 l/min
Density difference	0 – 10%
Temperature difference	0 – 50K
Viscosity difference	0 – 100%
Streamwise turbulence level	≈ 5%

Geometrical information of the CFD domain is provided in Figure 17. Comparison between simulations and experimental results will be carried out using several profiles at the center plane of the mixing section.

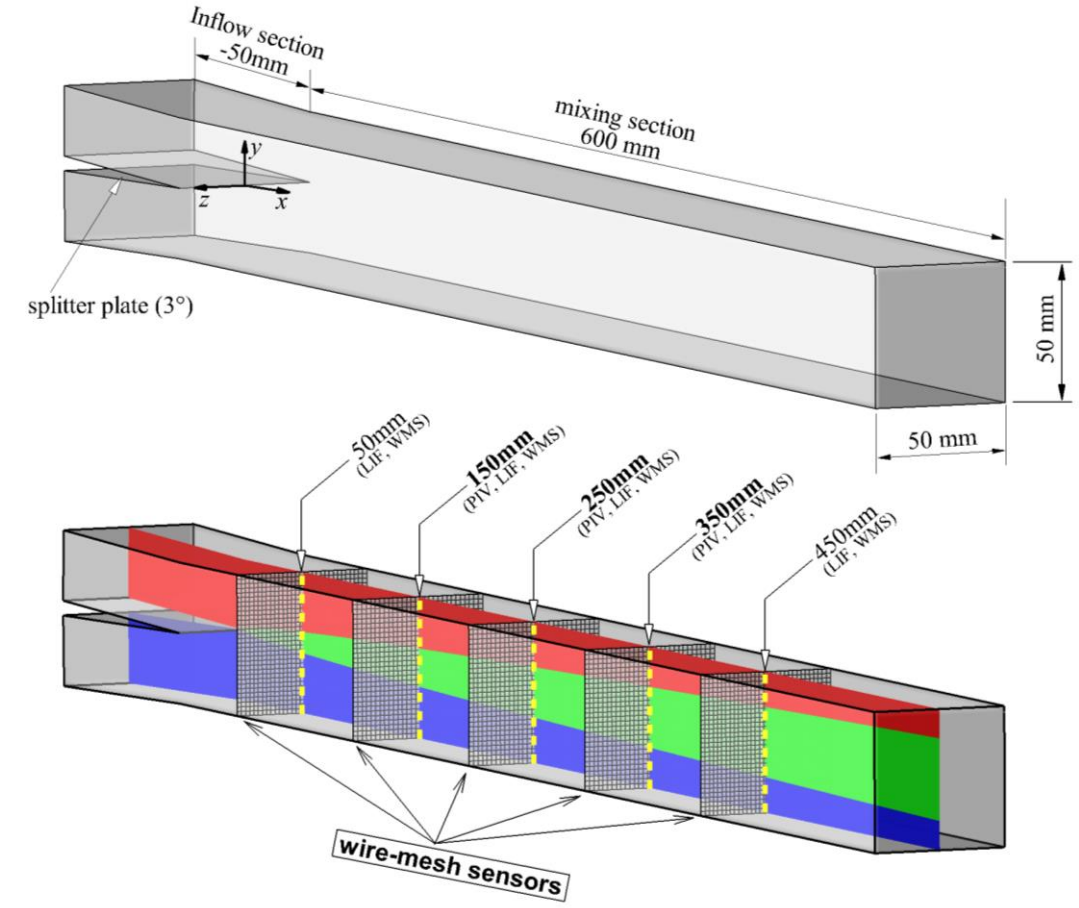

Figure 17: Schematic of GEMIX.

III.2 Numerical Grid Details

The GEMIX domain was modeled using the provided experimental dimensions [24] and shown in Figure 18. The experiment is characterized by two inlet channels which connect to a square mixing region. Both inlet sections are 25 mm tall, 50 mm wide. Since the inlet velocity boundary condition is fully developed, a longer section to develop the flow was unnecessary in the main simulation. The mixing section is 600 mm long and

starts where the inlets connect. The inlets are separated at a 1.5° angle from the horizontal axis of the mixing region.

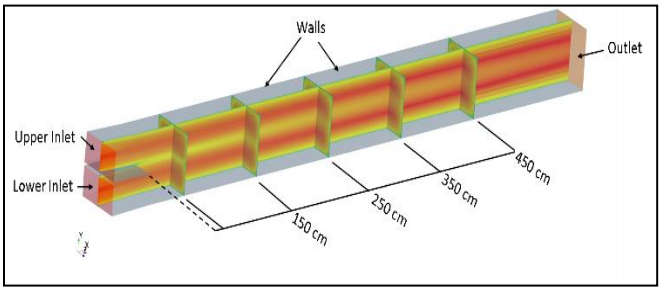

Figure 18: GEMIX Computational Domain and Surfaces. (Reprinted from [25])

The mesh was created using the built-in Star-CCM+ meshing tool with the following mesher. The trim grid generator was selected to mesh the mean flow while the prism layer mesh was used to develop near wall cells. The trimmer is a hexahedral grid generator that trims cells near wall/surface regions [17]. Volumetric refinement regions were created at the two inlets to resolve the inlet profile to a sufficient degree. In addition, volumetric refinements were added around mixing interface to resolve the effects due to the mixing. These regions were anisotropically refined in order to properly resolve the higher gradients due to density difference. Mesh sensitivity studies were conducted on three sets of grid. Coarse mesh was created by using 2.5 mm base size and 1.25 mm refinement size and resulted in 1.7 million cells were produced, for intermediate mesh base size was set as 1.5 mm and refinement size was set as 0.75 mm and resulted in 6.5 million cells. Finally, fine mesh is created by using 1.0 mm base size and 0.5 mm

refinement size and it has 19 million cells. In addition to that, finer mesh was used for periodic rectangular channel by using LES to achieve fully developed and higher fidelity inlet boundary profiles for the simulations. Time-averaged velocity profile from periodic channel is shown in Figure 19.

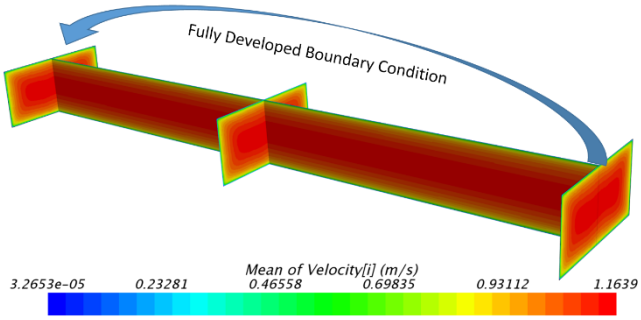

Figure 19: LES of Periodic Channel for Fully Developed Boundary Condition.

III.3 CFD Modeling Setup

The independent LES (Dynamic Smagorinsky Sub-grid model) simulation was used to obtain fully developed inlet profile for both upper and lower inlets. The main purpose of the periodic LES simulation was getting higher resolution data to prevent any bias on the grid refinement study. The comparison of LES and experimental inlet profiles were found in good agreement and applied to all simulations in the present study.

The corresponding Reynolds numbers for each inlet was ~33,000 based on the hydraulic diameter of each inlet. The mixing effects were accounted for by defining a different density at each inlet.

The segregated steady state solver is used with full buoyancy modeling by activated gravity and multi-component and then two different components are defined for bottom and top streams. Since density difference between components is $\Delta\rho=1\%$ and temperature difference is $\Delta T=2.5K$.

Buoyancy effects were accounted by enabling the gravity model in the "y-direction". It automatically adds source term into the momentum equation and also for turbulent kinetic energy and dissipation transport equations.

In this study, several turbulence models were compared against experimental data with same boundary and grid. Selected models are; *AKN k-ε, Realizable k-ε, Standard Non-linear Cubic k-ε, SST k-ω, Reynolds Stresses Model (RSM)* and *Spalart-Allmaras.* All of these models include buoyancy production and dissipation terms in the turbulence transport equations as default except, *SST k-ω* and *Spalart-Allmaras.*

Also those models are not recommended by CFD solver manual for the flow that has buoyancy.

In second part of this study, effect of the Turbulent Schmidt number was investigated by modifying default value from 1.0 to 0.8 and 1.3. Additionally, grid independence study is conducted by using three different grids. Finally, the convergence criteria were defined as the reduction of x, y, and z momentum, energy, species transport, and continuity residuals by at least 7 orders of magnitude.

III.4 Results

The experimental data was provided at several points downstream from the initial point of mixing the two fluids. In the experiment concentration and velocity profiles were measured at five different locations at 50 mm, 150 mm, 250 mm, 350 mm, and 450 mm and measurement plane are shown in Figure 18. The results from 50 mm, 250 mm and 450 mm are presented here. Some portions of following results are presented in [26].

III.4.1 Turbulence Model Sensitivity

Turbulence model effects are investigated on the coarse mesh, while some of them will be further analyzed in the following grid independence section. The velocity profiles along the vertical height of the channel with experimental and simulation are shown in Figure 20. The general trends of the experimental and simulation results comparable favorably for the k-ε models. On the other hand, RSM performed best as expected due to anisotropic approach, which flow has anisotropy due to density gradient in y-direction. Interestingly, Spalart-Allmaras model predicts better than most of the two-equation models.

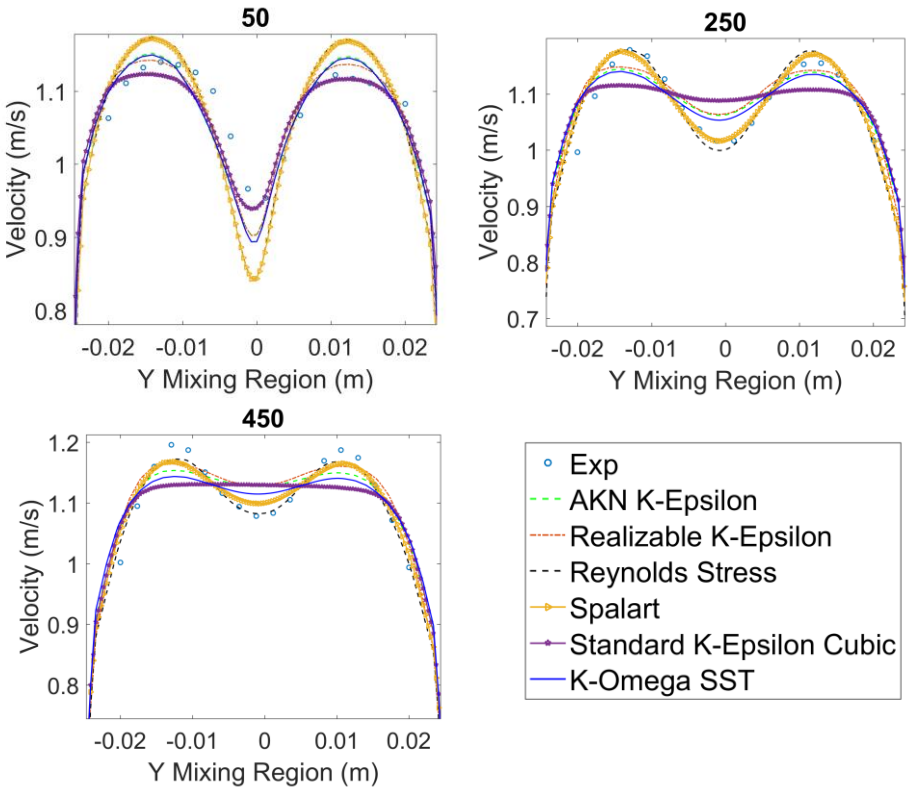

Figure 20: The velocity profiles along the channel.

The concentration profiles along the vertical height of the channel with experimental and simulation are shown in Figure 21. It can be seen that all models are matched with reasonable agreement except non-linear cubic model due to coarse grid. On the other hand, realizable *k-ε* presented best performance and Spalart-Allmaras performed well even with simpler approach. The *SST k-ω* shows less performance than other models due to lack of the buoyancy term in the TKE equation.

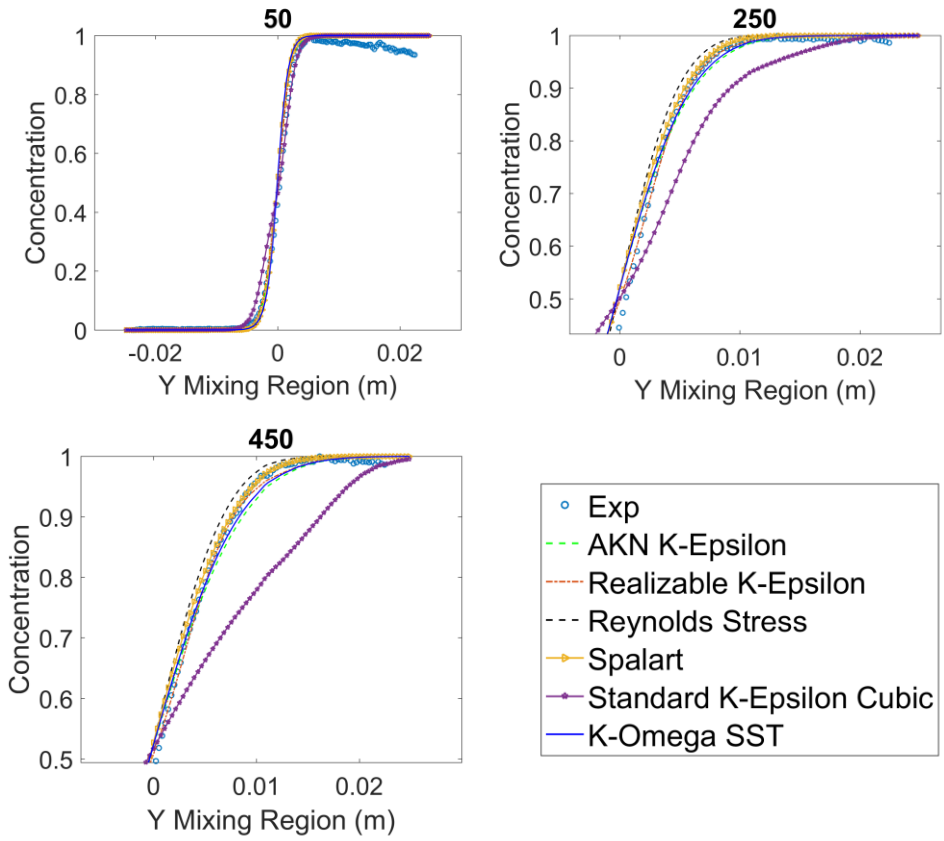

Figure 21: The concentration profiles along the channel.

III.4.2 Sensitivity on Turbulent Schmidt Number

Turbulent Schmidt number is a non-dimensional number, which is the ratio between the rates of turbulent transport of momentum and the turbulent transport of mass and in this case, it is affecting mixing of two streams due to turbulence. As it can be seen in Figure 22, uncertainty from Schmidt number is growing at downstream and most clear at 450 mm. Higher Schmidt number enhance turbulent mixing and creates steeper concentration, while lower Schmidt number causes less mixing and smoother concentration profile. Finally, turbulent Schmidt number has important effect on the mass

transport process and its effect can be higher than turbulence model selection, it should be carefully studied for benchmark studies.

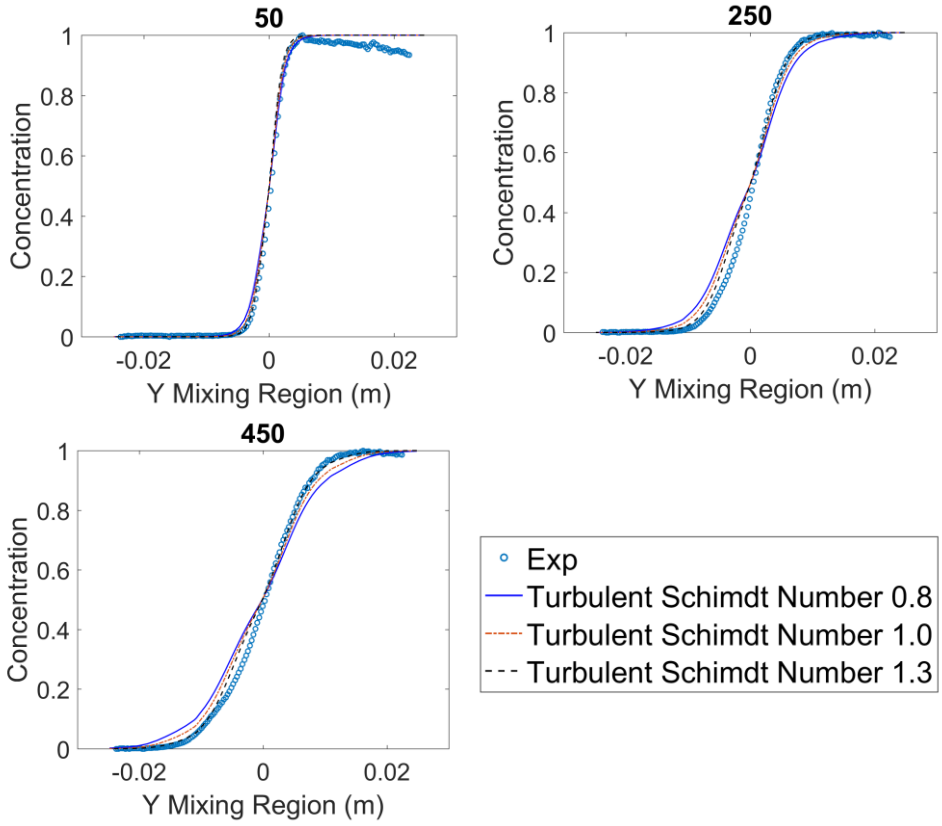

Figure 22: The concentration profiles for the turbulent Schmidt number sensitivity.

III.4.3 Grid Independence Study

In present study, there are two main objectives of the grid independence study, one is that to prove grid independence is obtained for the turbulence model sensitivity part that previously discussed. Second, non-linear cubic model showed non-reasonable results against other models. It was not expected due to its theory, which accounts anisotropy.

Only possible reason was the coarse mesh usage for this model. As shown in Figure 23, both realizable *k*-*ε* and standard *k*-*ε* cubic model matched each other for both velocity and concentration parameters except coarse cubic model, which proves that it needs finer mesh than other models. On the other hand, anisotropic approach is not showing significant difference than its peers.

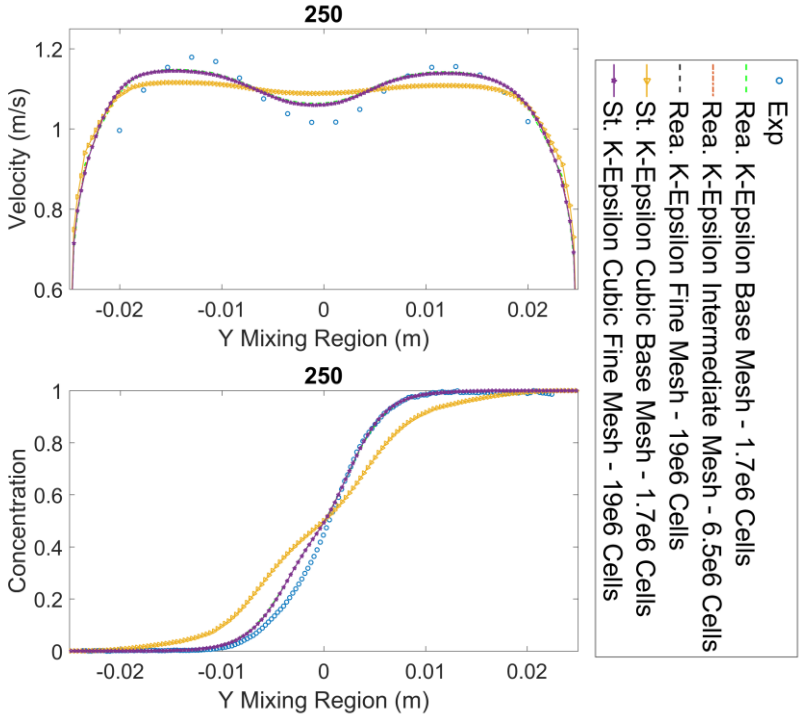

Figure 23: The velocity and concentration profile at line 250 mm.

CHAPTER IV

LARGE EDDY SIMULATION OF 5X5 PWR FUEL BUNDLE WITH MIXING VANE

IV.1 Geometry and Discretization

The geometry in question is the scaled test PWR 5x5 rod bundle by Westinghouse, where all the critical dimensions like bundle pitch (12.6 mm), rod diameter (9.5 mm), and grid features (dimples, springs, and mixing vanes) are identical to the full scale 17x17 PWR rod bundle. The only difference is the 5x5 lattice arrangement versus the 17x17 arrangement is that spacer grid assemblies are used to maintain the distance between the fuel rods in a PWR nuclear reactor core, to prevent rod vibration, and to provide lateral support for them by the use of grid springs and protuberances (dimples) formed in or attached to the metal grid. The installation of the mixing vanes part at the top of the conventional spacer grid improves the heat transfer efficiency of the fuel bundle. Geometry is shown in Figure 24.

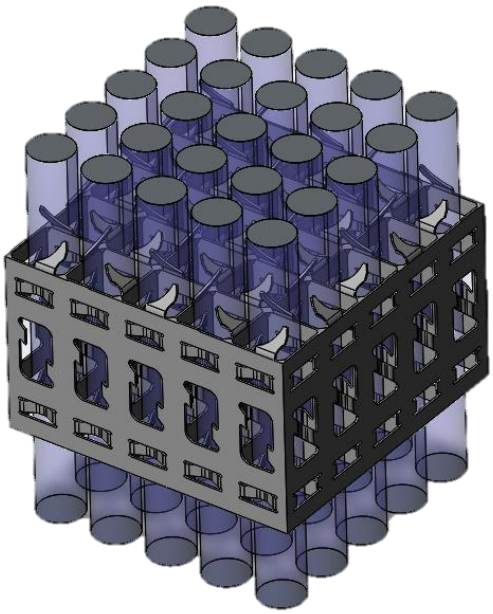

Figure 24: PWR 5x5 Mixing Vane with Fuel Rods.

In order to be able to reduce numerical diffusion, we used the hexahedral mesh by using pre-processing tools of the CFD Software Star-CCM+, and mesh quality criteria such as quality, volume change and, most importantly, skewness angle are carefully diagnosed for optimum mesh quality. In the LES study, two meshes were created for both the periodic channel and the actual simulation with mixing vane by using the same base size to keep the convective courant number as 0.5 (Δt= 7.8E-5 s, Δ= 0.2 mm along the horizontal direction and Δ= 0.4 mm in the vertical direction) which results in 131 Million hexahedral cells. Grids are shown in Figure 25 and Figure 26. For the main simulation, the base size is set as 0.4 mm with a refinement close to grid region with 0.18 mm with 10 prism layers in near wall, which results in y+= 0.4 from overall spatial and temporal average. Time step for main simulation is significantly lower than periodic bundle

simulation to limit maximum courant and average courant number in the domain, time step is 2 microseconds (Δt= 2.0 E-6 s). A full-scale mesh representation of the full-scale geometry, with a node number of 390 million.

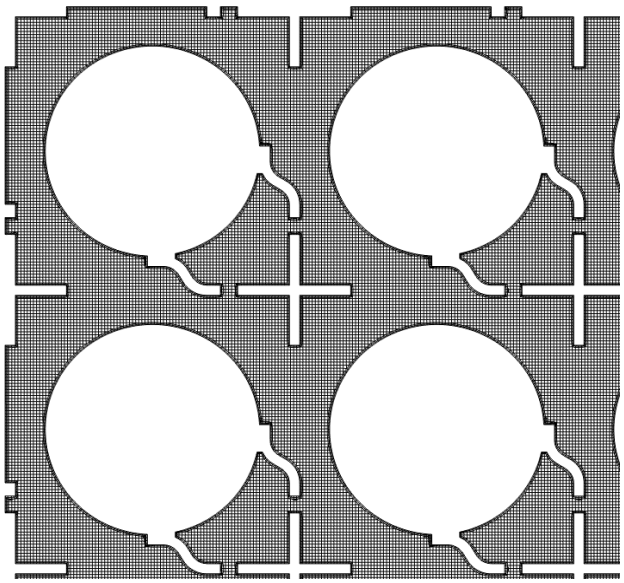

Figure 25: Mesh planar view from top of Mixing Vane.

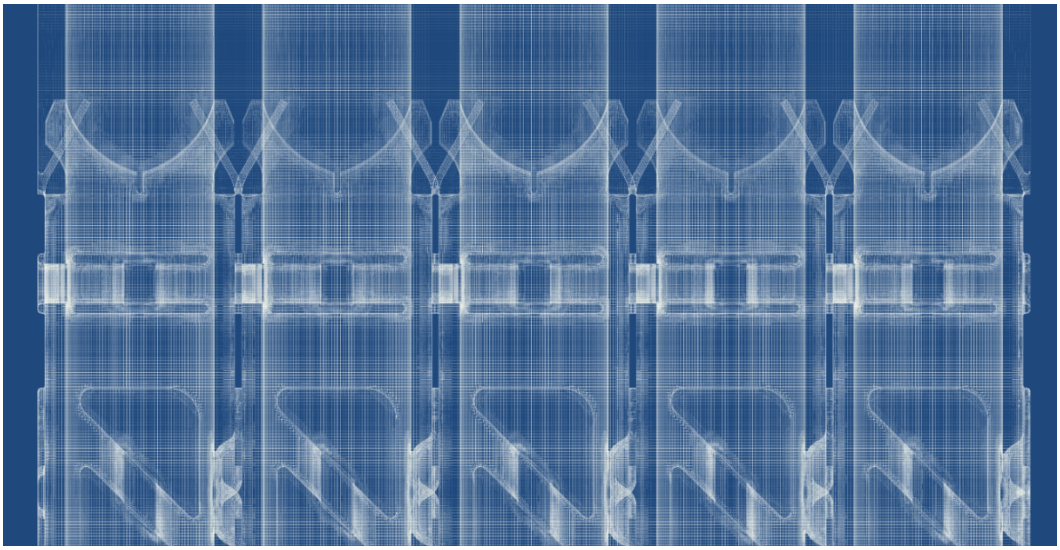

Figure 26: Mesh planar view from side of Mixing Vane.

IV.2 CFD Modeling

The benchmark experimental data were from Texas A&M Nuclear Engineering Department. The flow field has been measured with high-resolution particle image velocimetry. The flow field is well within the range of fully developed turbulent flow since the Reynolds number for the experiment was Re=14000.

CFD applications have commonly been used for turbulent flow in the last three decades. Although there are several turbulent models available, including hybrid variations, a general purpose turbulence model has not been developed yet. Each model has its own specific advantages or disadvantages according to the flow structures. Although the turbulent flow can be resolved directly by solving the Navier-Stokes equations, Direct Numerical Simulation (DNS) it is not feasible for current engineering problems due to its significant computational cost. As a compromise between accuracy

and computational cost, turbulence models have been developed. Large Eddy Simulation (LES) and Reynolds-Averaged Navier-Stokes (RANS) are used extensively for most of the current engineering problems.

Large Eddy Simulation Model, since this approach solves the large turbulent scales directly (resolvable scales) it is most likely to be able to model the turbulence physics better. Once the sub-grid model for the sub-grid scales has been selected after the spatial filtering process, we need a model for the sub-grid stresses. The selected model in this case is the WALE (wall-adapting local eddy viscosity) sub-grid scale model. As mentioned before, the LES with WALE SGS model is used for the simulation of boundary conditions and for the full-scale simulation.

As a sub-grid scale (SGS) model, the WALE model is used in STAR-CCM+ [17] .The fuel bundle and mixing vane has two main challenges, the strong secondary flow and geometry. The WALE sub-grid model was selected since it can capture the rotating flow features and the walls effect with right asymptotic behavior. The WALE sub-grid is different than other sub-grid models mainly since the eddy-viscosity model is defined using the rate of strain and rotation rate of strain as show in Eq. 9-11.

$$v_t = (C_w \Delta)^2 \frac{(S_{ij}^d S_{ij}^d)^{\frac{3}{2}}}{\left(\overline{S_{\iota J}}\,\overline{S_{\iota J}}\right)^{\frac{5}{2}} + (S_{ij}^d S_{ij}^d)^{\frac{5}{4}}} \tag{9}$$

$$S_{ij}^{d} = \overline{S_{\iota J}}\,\overline{S_{\iota J}} + \overline{\Omega_{\iota J}}\,\overline{\Omega_{\iota J}} - \frac{1}{3}\delta_{ij}(\overline{S_{mn}}\,\overline{S_{mn}} - \overline{\Omega_{mn}}\,\overline{\Omega_{mn}}) \tag{10}$$

$$\overline{\Omega_{\iota J}} = \frac{1}{2}\left(\frac{\partial \overline{u_{\iota}}}{\partial x_j} - \frac{\partial \overline{u_J}}{\partial x_i}\right) \tag{11}$$

LES – WALE model is used for both precursor simulation to obtain fully developed boundary condition and for the main simulation. The results from periodic case is applied to standard k-epsilon method to estimate the two-equation modeling capability. The fully developed analysis part is the key point of this work. The goal was to get the most reliable and accurate inlet boundary conditions relying on the turbulent statistics given by LES, such as average velocity components, Reynolds stresses, and all the derived turbulent quantities. Good predictions of the inlet boundary for the LES and RANS models were obtained and then, in the latter case, the sensitivity of the simulation results on the inlet boundary (velocity and turbulence) were shown. An attempt was made to demonstrate that the simple RANS approach to turbulence modelling coupled with accurate turbulent boundary conditions can predict with a good estimate complex turbulent flows. The validation of the results will demonstrate the capabilities of the two approaches to turbulence in predicting the main and the secondary flow patterns.

In the following section, grid resolution will be analyzed due to the necessity of resolving enough scales on the turbulence spectrum, well-refined grids are used for LES

model and point data are extracted to apply fast Fourier transfer (FFT) to quantify the characteristic -5/3 scope for inertial subrange, since any LES simulation that cannot resolve inertial subrange cannot be considered as proper LES.

In order to create good time statistics, recirculation boundary condition was imposed in order to reach a fully developed flow field, mass flow rate is set as 3.00679 kg/s ,which is taken from experimental volumetric flow rate and Re=14,000, which results in about 1.335 m/s surface average velocity. For turbulence development, random eddies was imposed as initial condition. This is also called the synthetic eddy method (SEM), which consists of an addition of random flow field fluctuations to the mean velocity field. Time-averaged components of three velocities and six components of the Reynolds stresses are collected in the precursor periodic simulation. The results from this first simulation then have been applied as boundary conditions for the full scale LES and RANS simulation.

The precursor simulation for the fully-developed boundary condition was run long enough to achieve a statistically stationary state [27]. In this point, the surface-averaged friction velocity was calculated at one instantaneous time frame and then was used to calculate the required time for seven flow-through times along the domain, which corresponds about 11 s of simulation time. The instantaneous and time-averaged velocity results are shown in Figure 27.

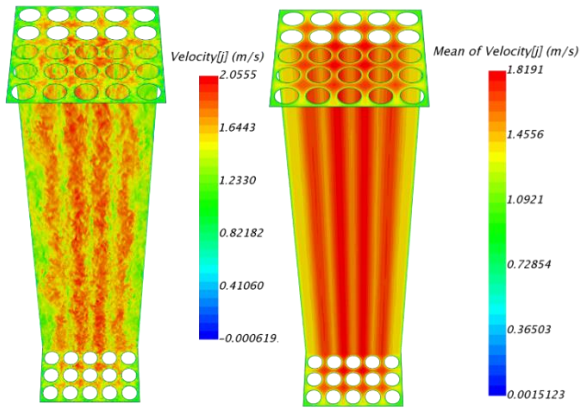

Figure 27: Instantaneous axial velocity and Time-averaged axial velocity.

In addition to velocity parameters, time-averaged turbulent kinetic energy (TKE) can be seen in Figure 28 and it also show line profiles for the Figure 29, which shows the velocity magnitude on three different line profiles.

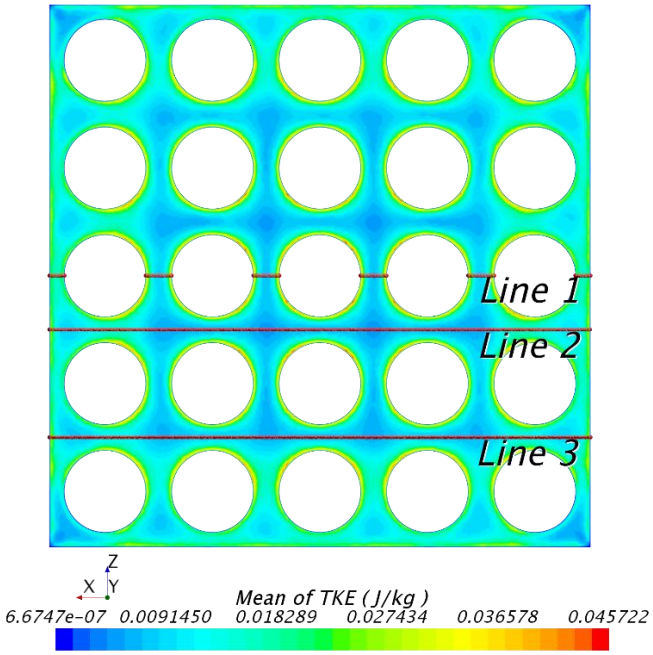

Figure 28: Mean of Turbulent Kinetic Energy (J/kg).

It is well-known that turbulence is diffusive and dissipative. As shown in Fig.6, the TKE is stronger near assembly walls and weaker in the center as expected due to the wall effect. The velocity profile on line 2 is sharper than line 3 since there is more diffusion on line 3 due to higher turbulence, and as shown in Fig.7 it is even sharper in the centerline (line 1).

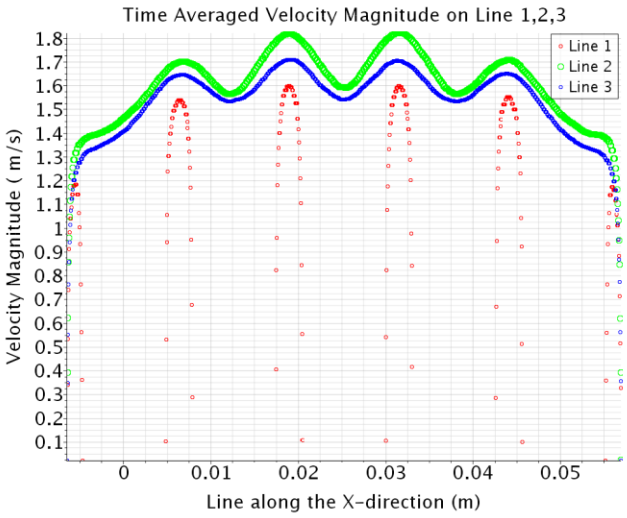

Figure 29: Time-averaged of Velocity Magnitude (m/s).

IV.3 Fast Fourier Transform Analysis

According to Kolmogorov's theory, there are three main regions on the turbulence spectrum. Large eddies with lower frequencies, the inertial range, and dissipation range. For LES, the criteria for a grid of sufficient fineness is that it must be fine enough to resolve the inertial range to get meaningful results. Therefore, a Fast Fourier Transform (FFT) can be used to assess the numerical grid resolution by checking the turbulence spectrum. This test can be done to check for the characteristic slope (-5/3) of the inertial range according to the Kolmogorov's 5/3 theory [21]. Several points are chosen in the domain along the channel and axial velocity data are extracted at 1500 time step. The location of the points are shown in Figure 30.

Figure 30: FFT points in the domain.

As shown in Figure 31, -5/3 slopes are observed and inertial subrange is resolved on grid scale. Therefore, it can be assumed that the grid resolution is sufficient. Additionally, as shown in the figure, inertia forces are dominant close the mixing vane region, which was captured at lower frequency region with higher power amplitude due to the dominant inertial forces.

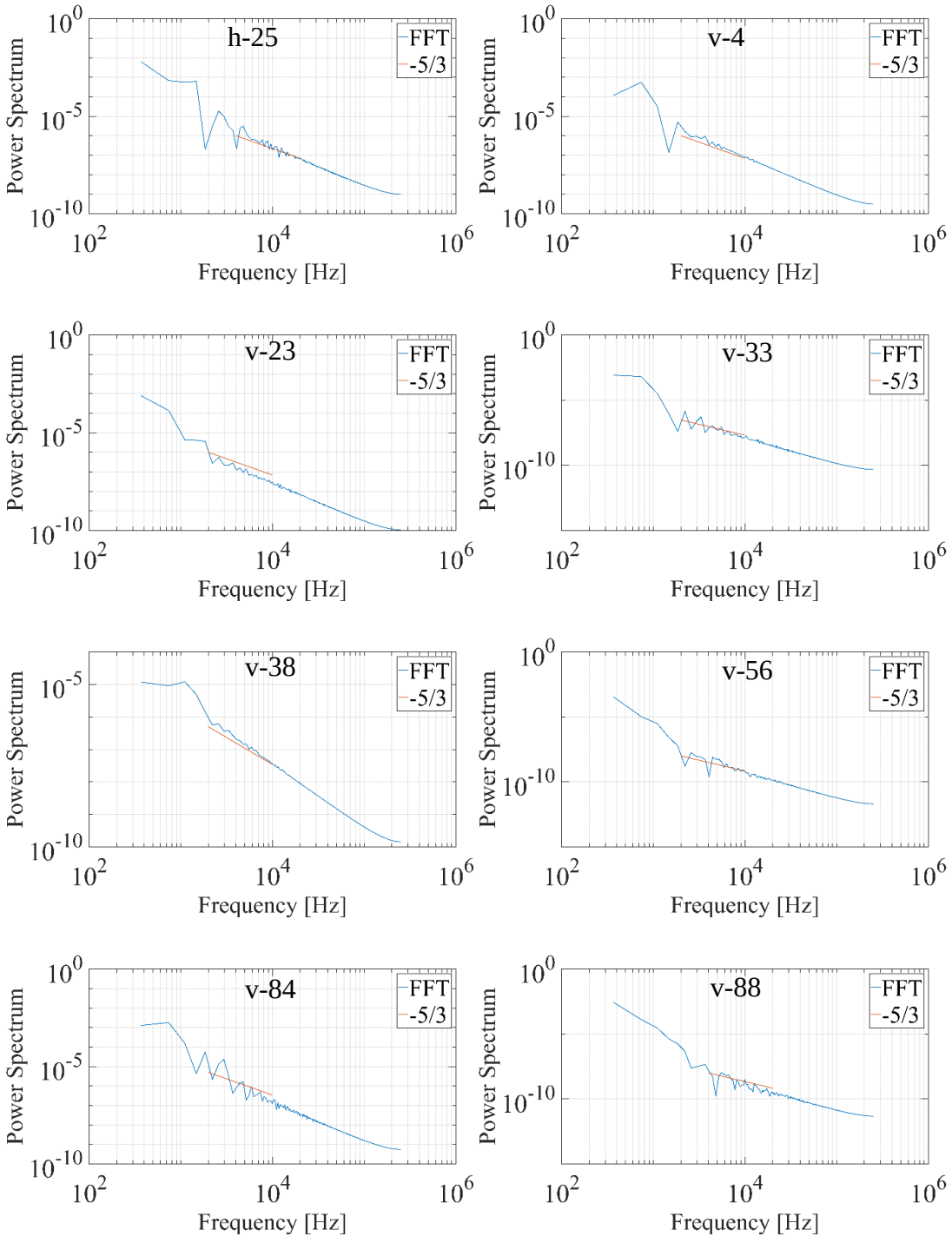

Figure 31: FFT Results on different points and -5/3 slope.

IV.4 Large Eddy Simulation Results

IV.4.1 Surface Averaged Analysis

Secondary flow intensity is an important parameter for the mixing vane design and analysis both experimentally and numerically since the main purpose of the mixing vane is enhancing heat transfer through higher secondary flow intensity. In the present study, the full domain length is 588 mm, the mixing vane starts at 84 mm downstream from the inlet, and the top point of the wing is at 128 mm from the inlet. After time averaged is done for pressure and velocity components. 32 horizontal planes are created with equal space through axial direction. Then both lateral components of the velocity are surface averaged as given:

$$I_{sec} = \frac{1}{A}\sum_i \frac{A_i\sqrt{{V_x}^2 + {V_z}^2}}{\overline{V_y}} \tag{12}$$

where V_x and V_z are time averaged lateral velocity components, A_i is cell surface area and $\overline{V_y}$ is time and surface averaged axial velocity. The result of this analysis can be seen in Figure 32. It captures the secondary flow from the mixing vane and the maximum value is in well agreement with references that are analyzed in Introduction chapter, which is mostly between 27% and 34% depends on the vane design, bundle configuration, and Reynolds number.

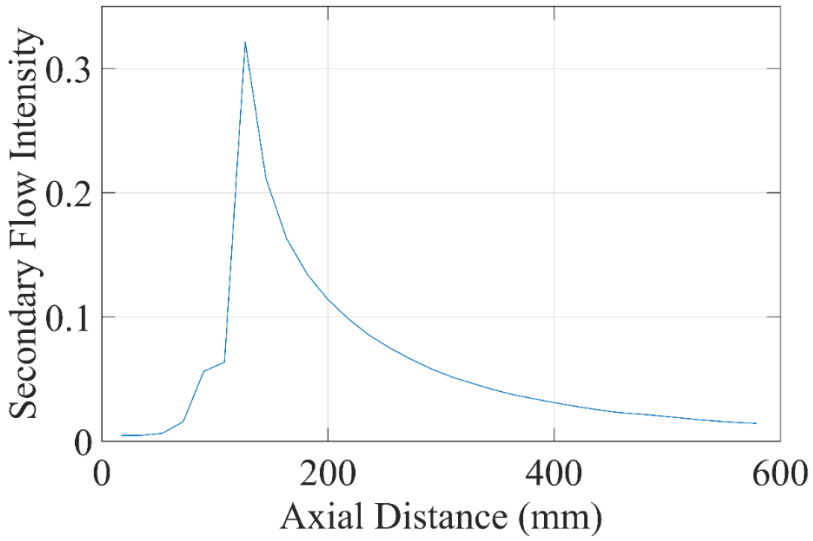

Figure 32: Secondary flow intensity vs. axial distance from inlet.

After time averaging is done for pressure at the whole domain. Same 32 horizontal planes are used to calculate surface averaged pressure as given by the equation:

$$\overline{P} = \frac{\sum_i A_i P_x}{A_{sum}} \tag{13}$$

where A_i is cell surface size and A_{sum} is total surface area of horizontal plane and P_x is the time averaged total absolute pressure. As shown in Figure 33, the pressure drop has a linear relation as expected in the domain except within the mixing vane area. The mixing vane is increasing losses by increasing the pressure drop while enhancing the turbulent mixing.

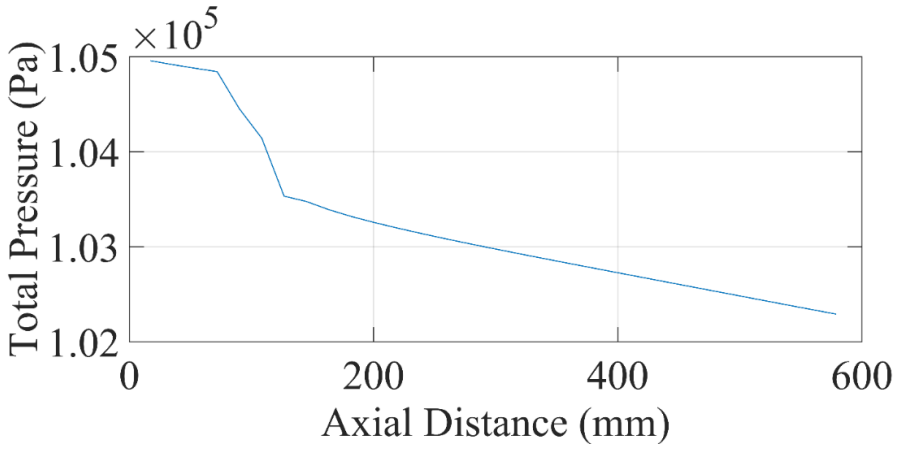

Figure 33: Total Absolute Pressure vs. axial distance from inlet.

As it can be seen in Figure 34, at the point where the head loss caused by mixing vane ended, the secondary flow has its peak, then it decays exponentially along the domain, while the pressure drop continues to drop linearly.

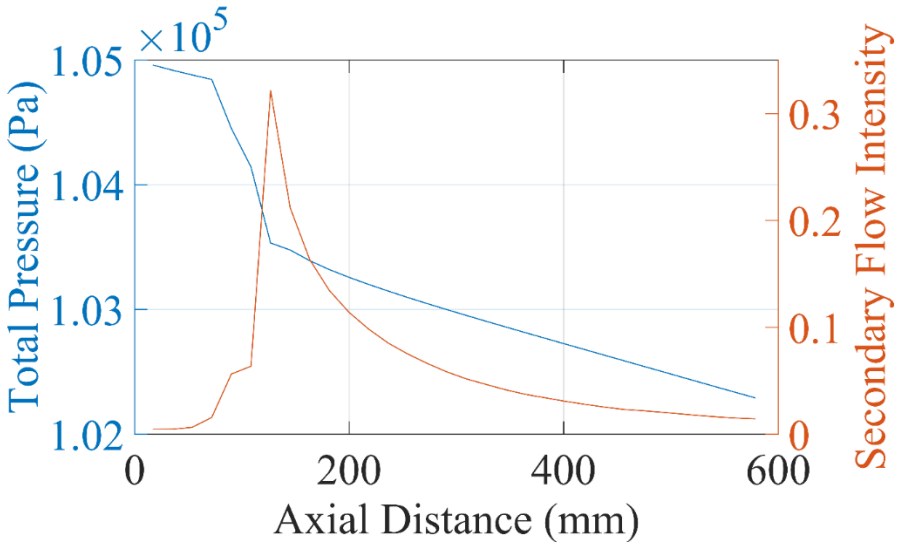

Figure 34: Pressure and Secondary Flow intensity vs. axial distance from inlet.

IV.4.2 LES and RANS Quantitative Comparisons

For a RANS vs. LES comparison, an independent simulation has been conducted [28] by using standard k-epsilon modeling. Before starting the comparison, the experimental measurement planes and CFD measurement planes needs to be discussed. In Figure 35, experimental measurement planes and their coordinate systems are shown. Plane 1 and Plane 2 are defined in Figure 35(c). Same planes are created in the CFD simulation and the presented results throughout the rest of the subsections refer to those two vertical planes. These planes are located in the center between the rod pitches. On the other, Y axis is defined as axial direction both in experiment and CFD simulation, while X axis on experiment is equivalent for Z axis on CFD simulation and vice versa for Z axis. Coordinate transformation will be done only when experimental and LES results are compared. The rest of the CFD results are given its own coordinate system.

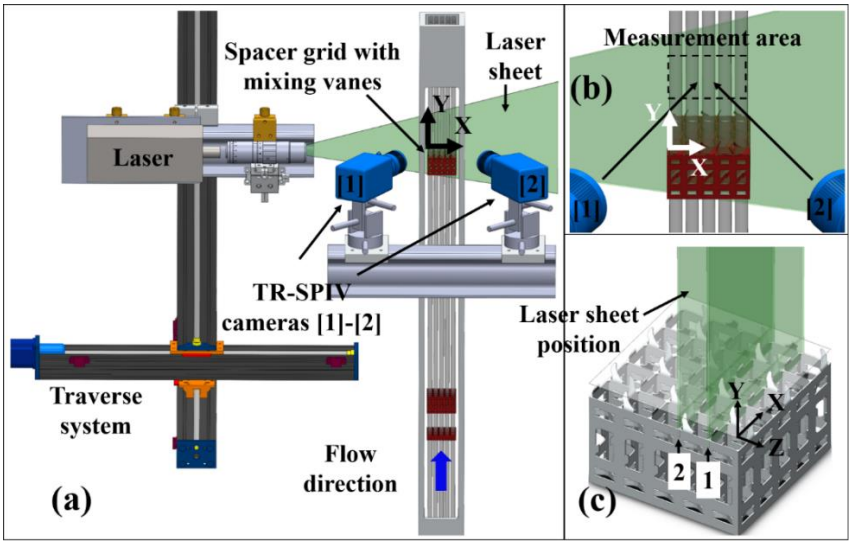

Figure 35: Experimental measurement planes 1-2.

In addition to experimental vertical Plane 1 and Plane 2, horizontal planes are defined as Horizontal 1 and Horizontal 2, where placed 0.5 hydraulics diameter (=4.5mm) and 2 hydraulics diameter (=18 mm) downstream from the top of wings, respectively. The top of the wings are also axial reference point for experimental measurements, which is y=0 at the top of the wings. It is also taken as reference point for CFD simulations. The planes are shown in Figure 36.

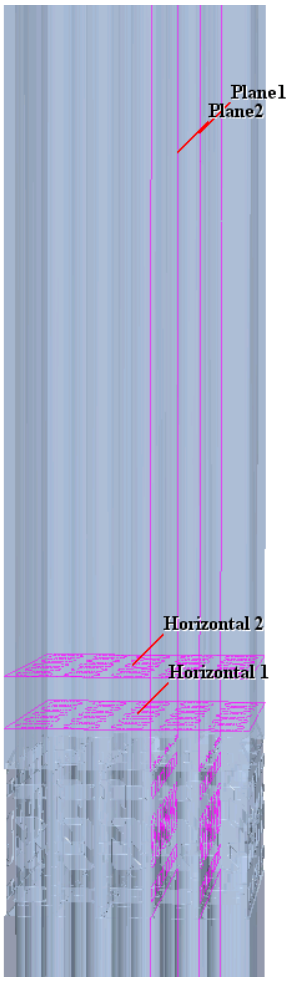

Figure 36: Measurement planes on the CFD domain.

As previously explained the location of measurements, they are used for the following figures for RANS vs. LES comparisons. As shown in Figures 37 – 42, the velocity components are in good agreement, with small difference mainly in the lateral components due to strong secondary flow. The reason of capturing flow structures closely, in this region, is that inertia forces are dominant, where viscous forces play less important role. As previously mentioned in the literature review, turbulence modeling sensitivity needs to be done further downstream, the velocity profile here is used for statistical convergence verification.

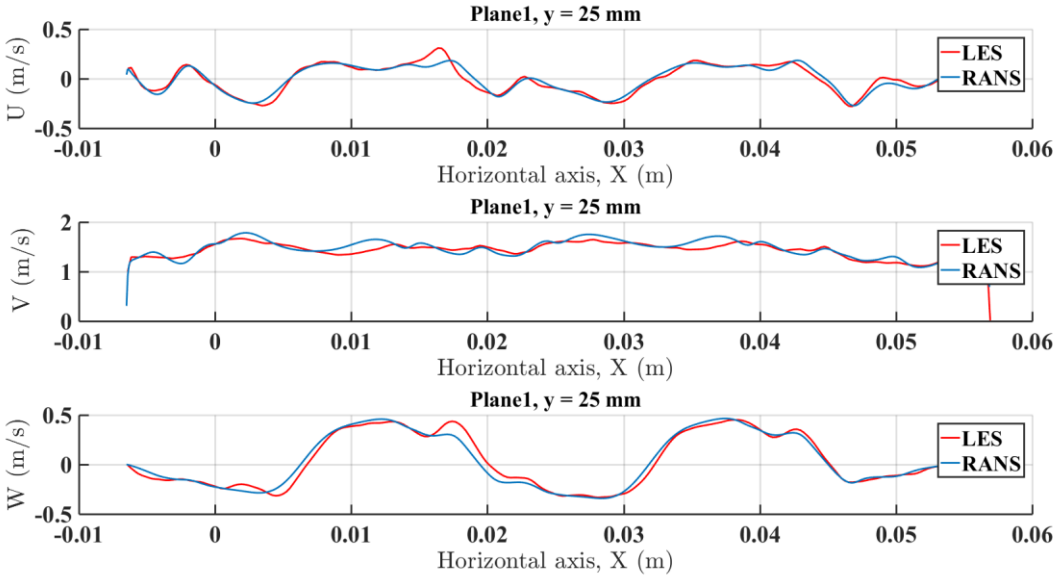

Figure 37: Velocity components comparison of LES vs. RANS at plane 1 at y=25mm.

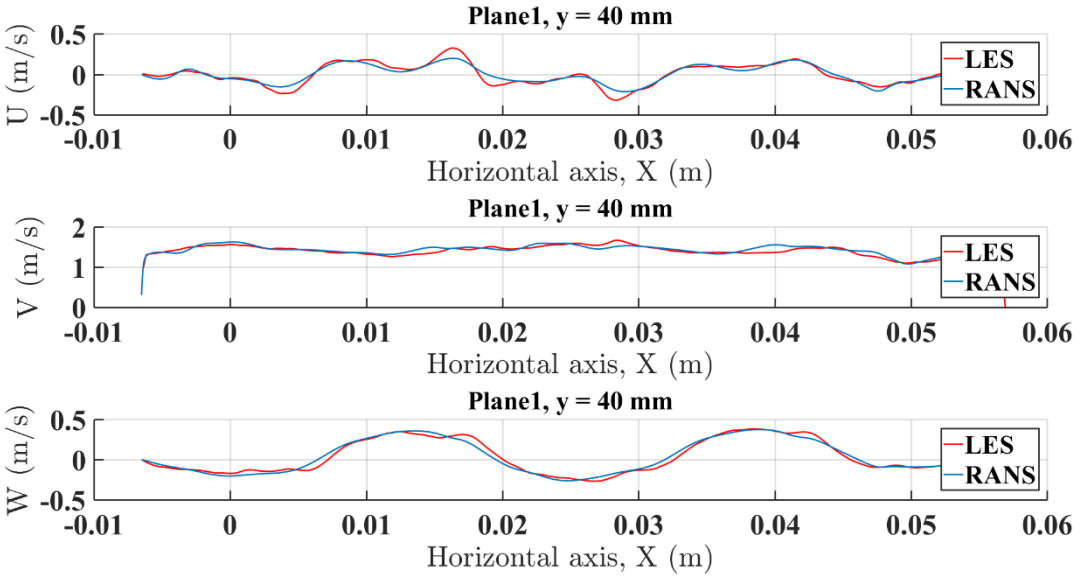

Figure 38: Velocity components comparison of LES vs. RANS at plane 1 at y=40mm.

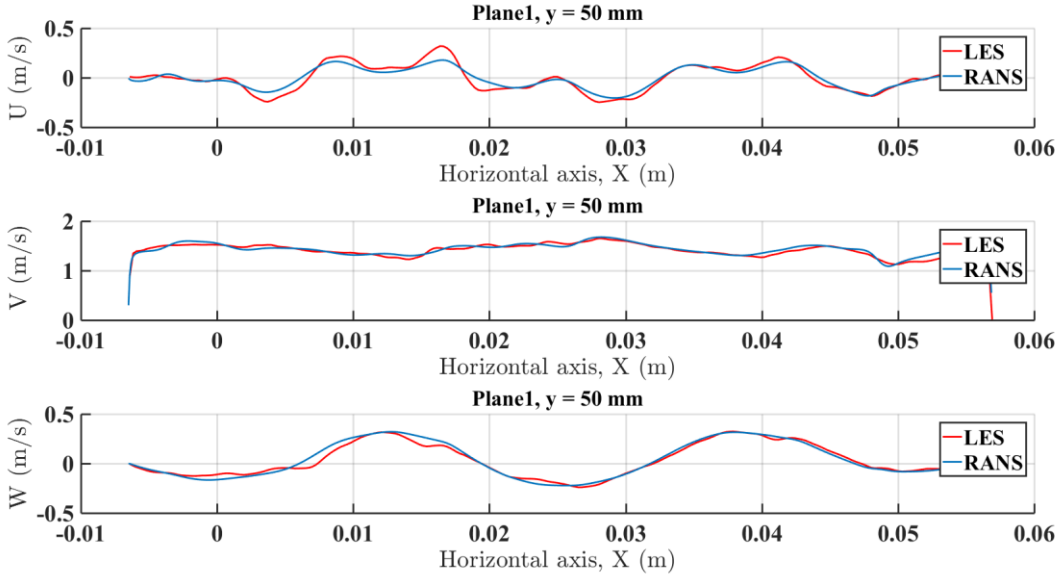

Figure 39: Velocity components comparison of LES vs. RANS at plane 1 at y=50mm.

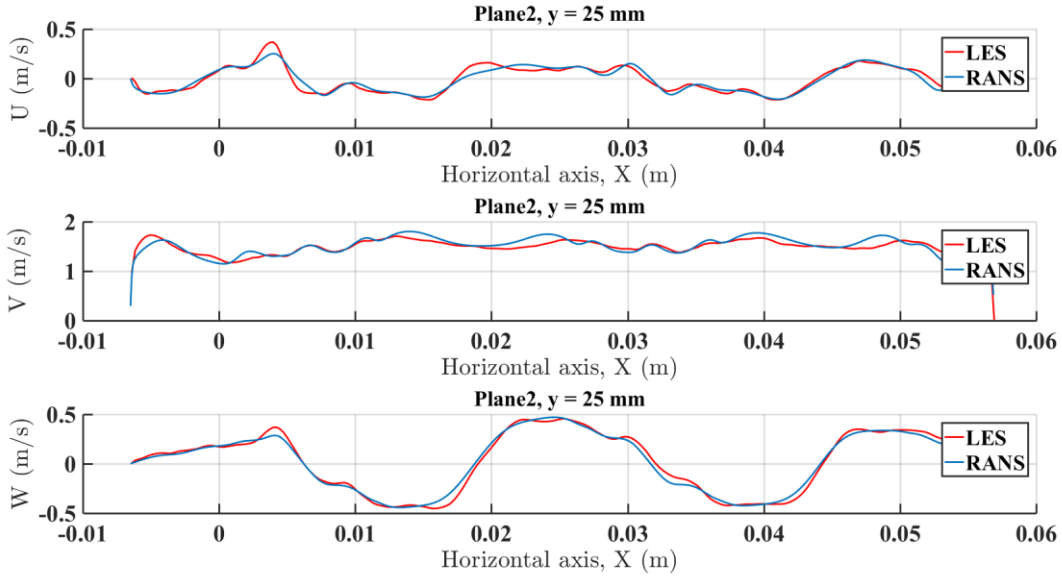

Figure 40: Velocity components comparison of LES vs. RANS at plane 2 at y=25mm.

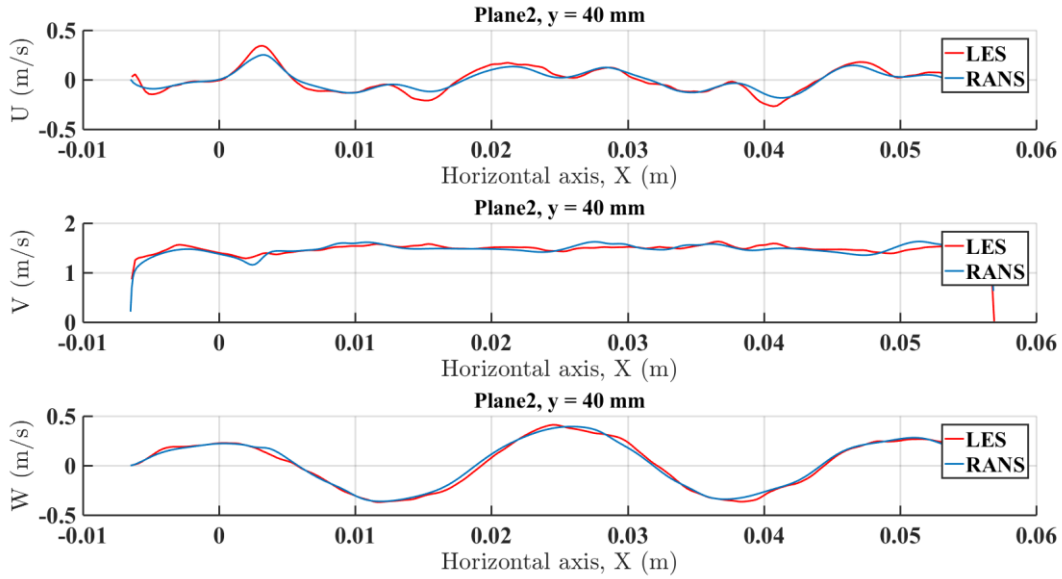

Figure 41: Velocity components comparison of LES vs. RANS at plane 2 at y=40mm.

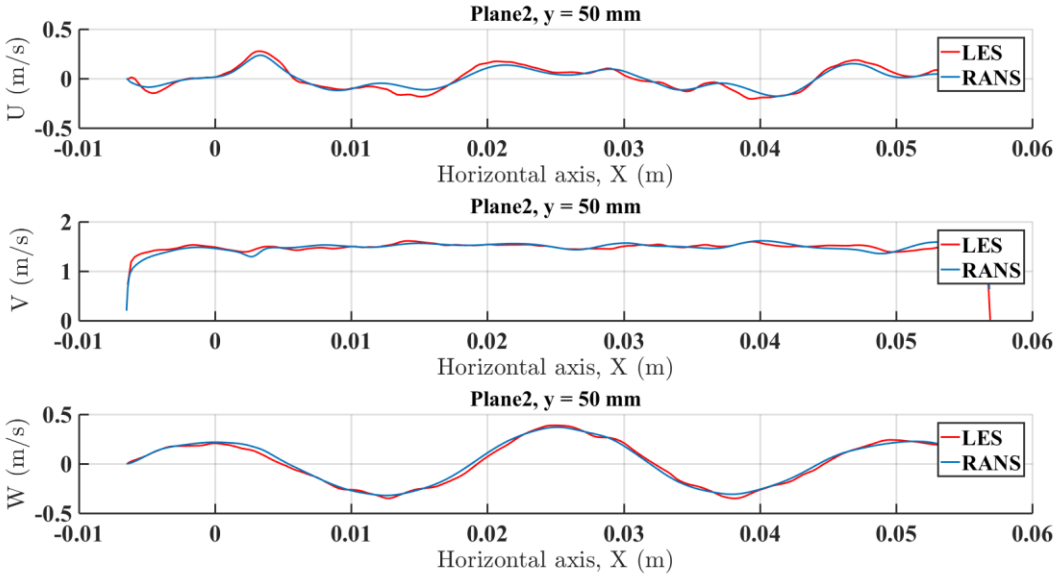

Figure 42: Velocity components comparison of LES vs. RANS at plane 2 at y=50mm.

While velocities are found to be in very good agreement between RANS & LES, this is not the case for the turbulent kinetic energy (TKE) values as shown in Figure 43 and Figure 44. The dominant inertia forces were causing less sensitivity for the modeling of the velocity profile. However, the flow is strongly anisotropic and fluctuations are relatively high. Therefore, TKE presents different magnitudes, but still, the general trend is similar. On the other, when the results are taken further downstream from mixing vane, the results are getting closer with LES and RANS as shown in both Figure 43 and Figure 44 at y=50 mm.

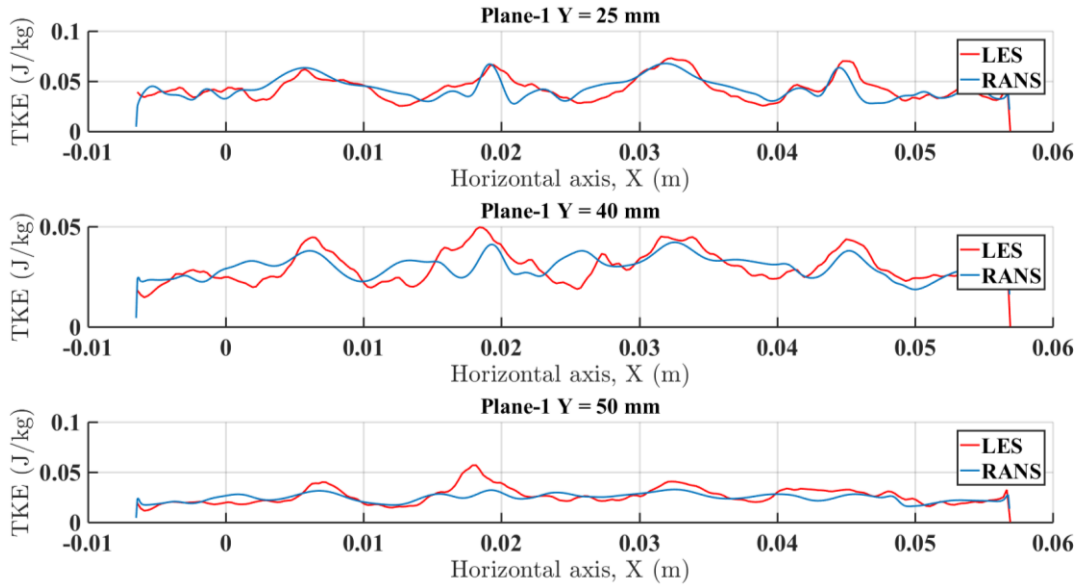

Figure 43: Turbulent Kinetic Energy comparison of LES vs. RANS on plane 1.

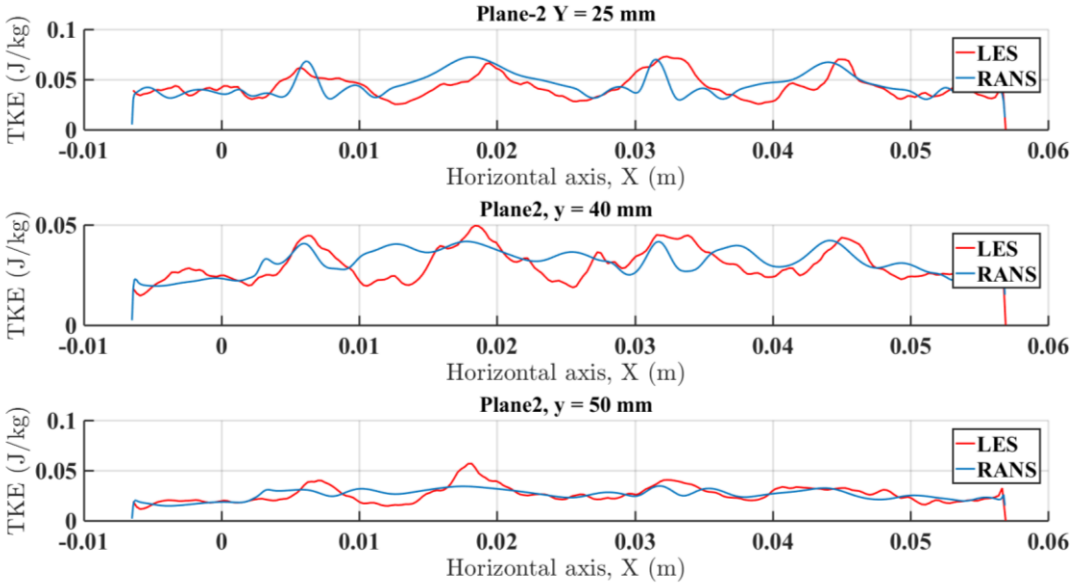

Figure 44: Turbulent Kinetic Energy comparison of LES vs. RANS on plane 2.

IV.4.3 Qualitative LES Results

After comparison with RANS results. In this part of chapter, time averaged parameters are shown to observe flow development along the fuel bundle. Also to present as future reference for steady-state simulations. As previously explained, the location of measurements, same notations are used here. As shown in Figure 45, velocity magnitude has its peak right after mixing vane wings due to high swirling flow. It should be also noted that the profile of the velocity is recovered after about 9-10 hydraulic diameters from the mixing vane. So the region of experimental interest for measurement within the value of these diameters for the better validation of the CFD codes. Also the mixing vane has higher contribution to the mixing close to the centerline channel due to more swirling from neighbor wings than the plane close to the wall (plane 1). Figure 46 and Figure 47 show the TKE and the secondary flows respectively, one should note that the TKE and secondary flow have similar structures, since the turbulence is enhanced by secondary flow in this area and, as mentioned before, they decay exponentially and the effect of mixing vane is almost negligible in about 10 hydraulic diameter.

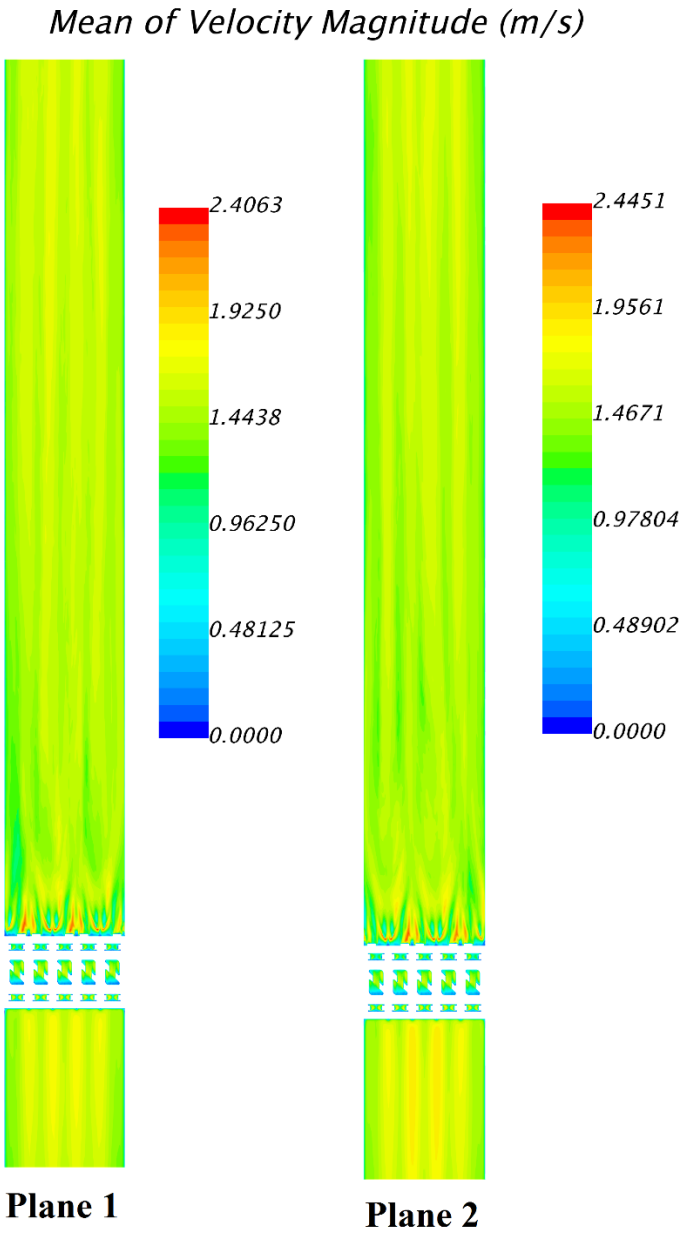

Figure 45: Time-averaged velocity magnitude (m/s).

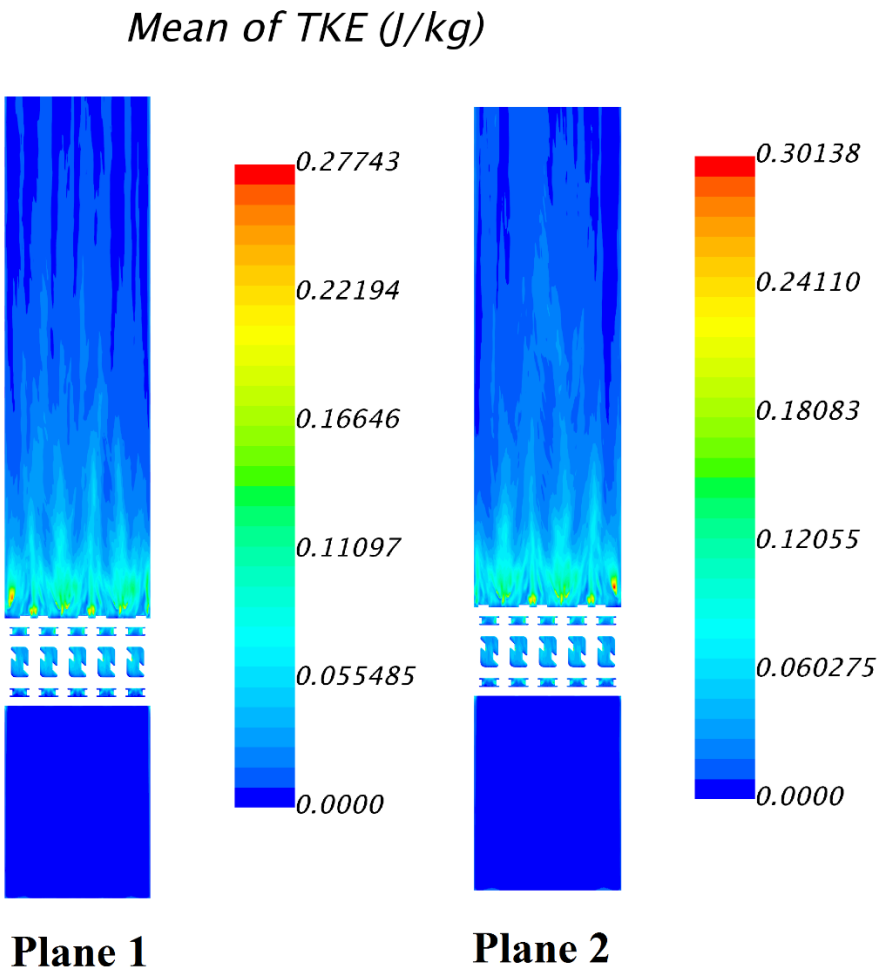

Figure 46: Time-averaged TKE (m^2/s^2).

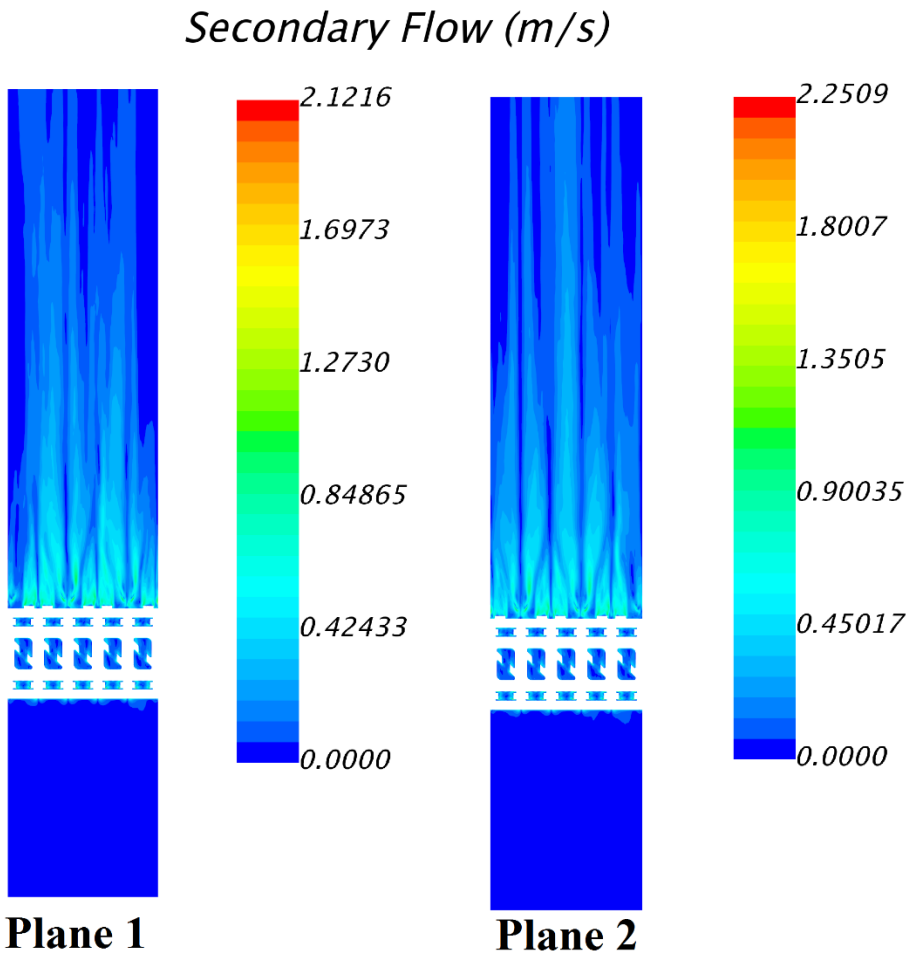

Figure 47: Time-averaged secondary flow (m/s).

As shown in Figure 48 and Figure 49 velocity structures changes significantly even within 1.5 hydraulic diameter distance. Also secondary flow dominance can be seen close to the vane on Figure 48. Additionally, it can be noted that the symmetrical structures are showing the temporal convergence of the simulation. In Figure 50 and Figure 51, it shows the evolution of the TKE between two horizontal planes. While it has sharper gradient at 0.5 hydraulic diameter, it has smoother TKE profile at 2 hydraulic downstream of the

mixing vane. It is showing how structures of turbulence decays between sub-channels through axial direction, also the order of magnitude is more than half for the peak TKE values between two planes, which shows the importance of the uncertainty on the location of the experimental measurements for the statistical value measurements.

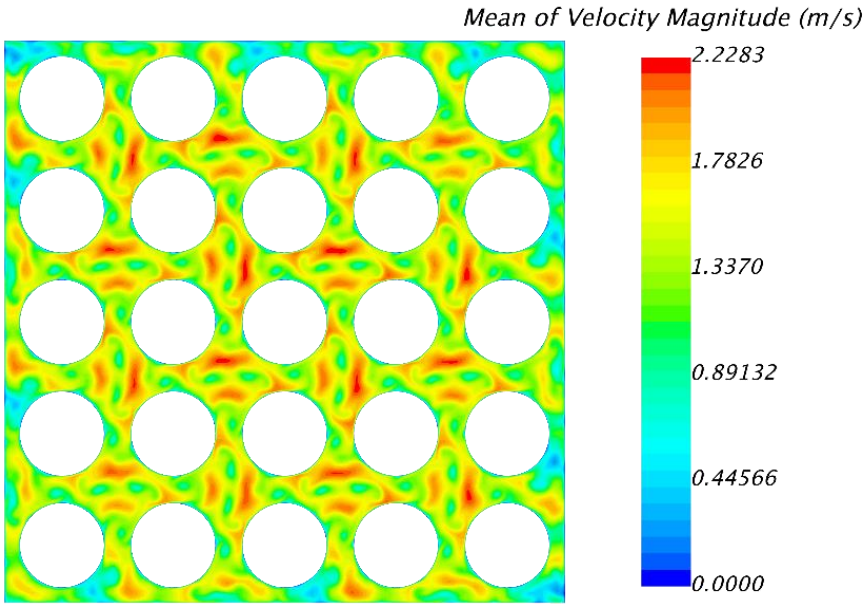

Figure 48: Time-averaged velocity magnitude on Horizontal-1 (0.5 Dh).

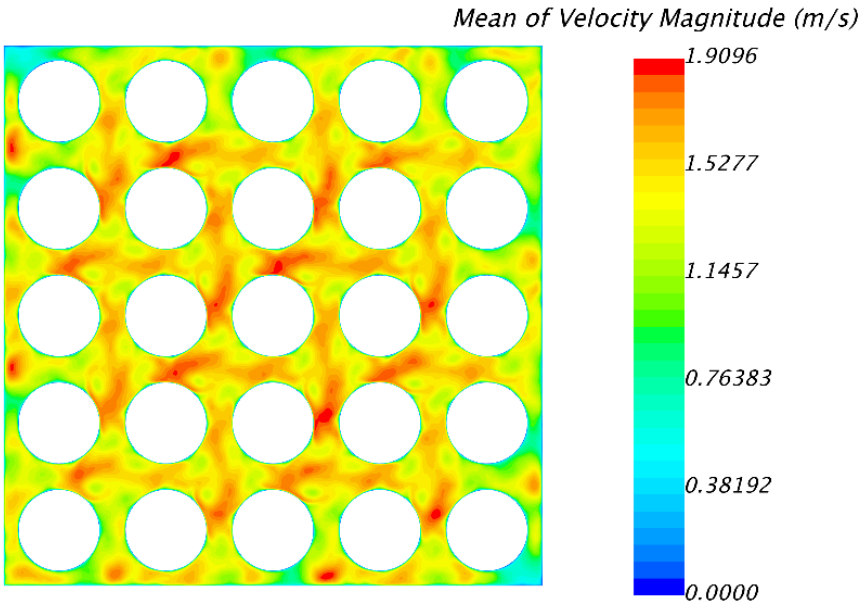

Figure 49: Time-averaged velocity magnitude on Horizontal-2 (2 Dh).

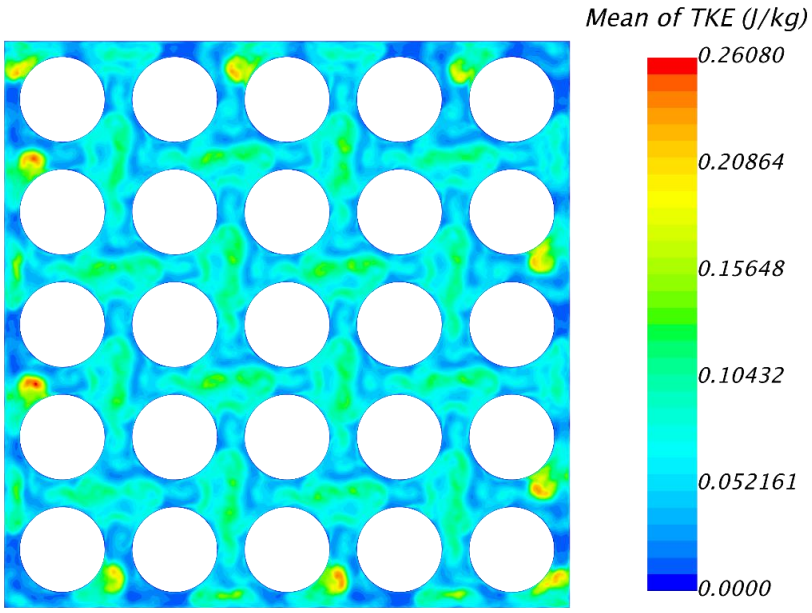

Figure 50: Time-averaged Turbulent kinetic energy on Horizontal-1 (0.5 Dh).

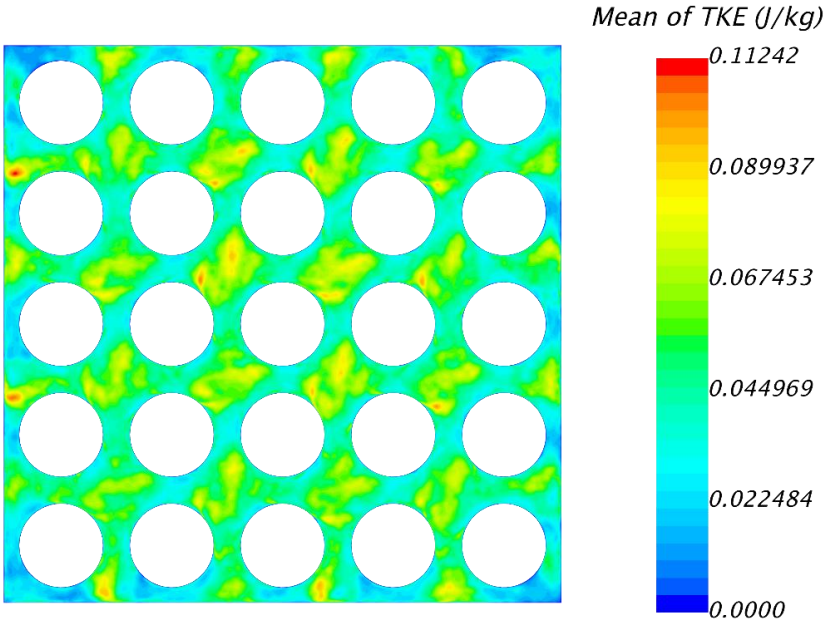

Figure 51: Time-averaged Turbulent kinetic energy on Horizontal-2 (2 Dh).

Figures 52, 53 and 54 are showing secondary flow from planar velocity, which is commonly visualized in the literature and it reveals same flow structures here with available experimental and computational flow structures. In Fig. 30, the secondary flow is higher near fuel rod surface in the neighborhood of the central sub-channel, which is desirable for the design purposes due to power shape distribution in the fuel assembly.

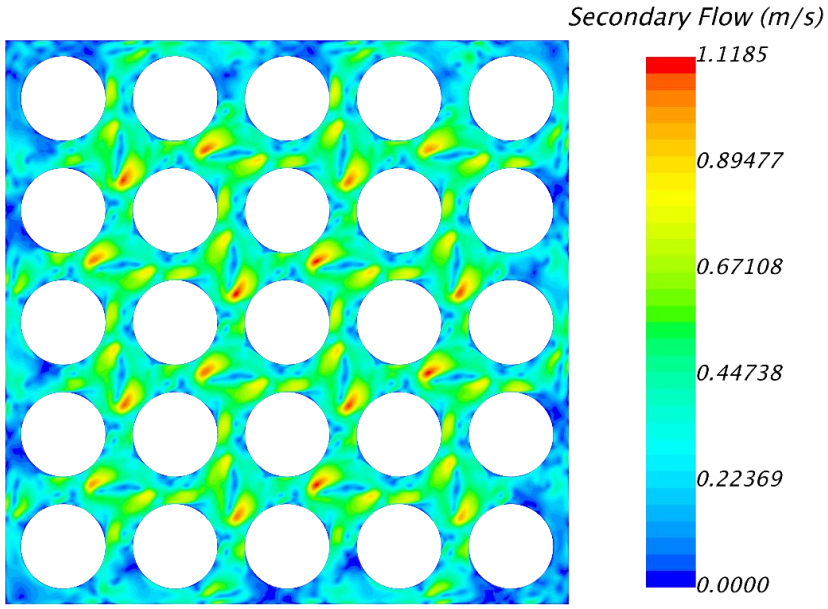

Figure 52: Time-averaged Secondary flow on Horizontal-1 (0.5 Dh).

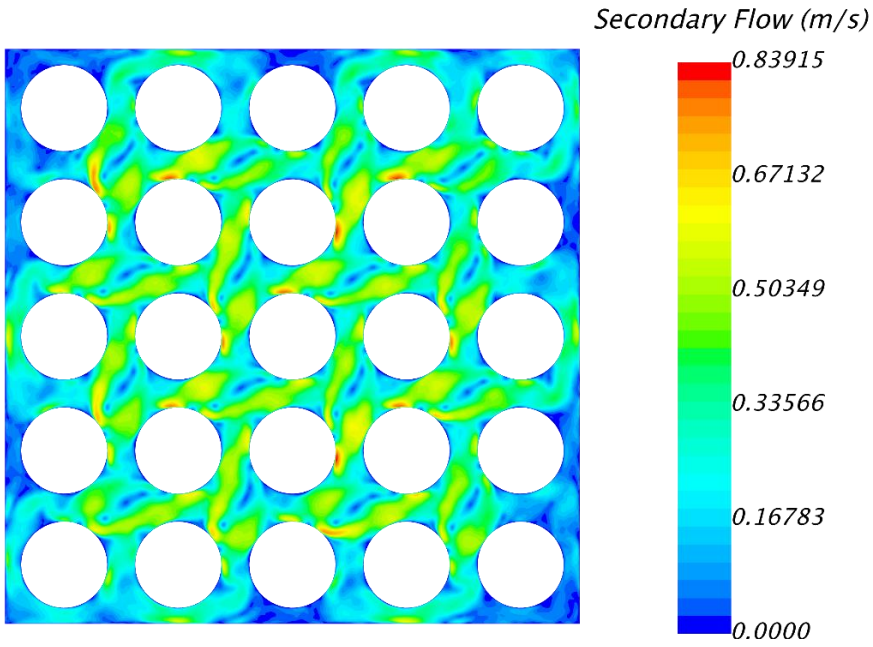

Figure 53: Time-averaged Secondary flow on Horizontal-2 (2 Dh).

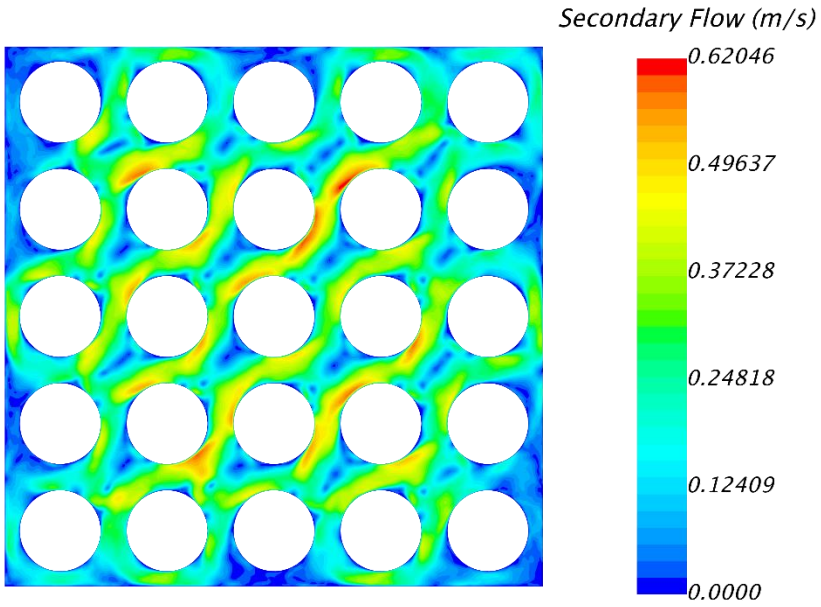

Figure 54: Time-averaged Secondary flow on Horizontal-3 (4 Dh).

IV.5 Proper Orthogonal Decomposition

The POD algorithm to investigate coherent structures in turbulent flows was first proposed by Lumley [19] . The methodology is based on extracting an orthogonal set of spatial eigenfunctions from the random field. The main goal of POD is to find the optimal representation of the field by solving a Fredholm integral eigenvalue problem given in Eq.14.

$$\int R(x,x')\phi(x')dx' = \lambda\phi(x) \tag{14}$$

However, the direct solution of this problem is computationally expensive. Sirovich [20] proposes a solution to this problem, which is known as the Method of Snapshots. The

method considers a set of M linearly independent flow realizations. Applying the method of snapshots results in following equation.

$$RA = \Lambda A \tag{15}$$

where A is a matrix that includes mode coefficients, Λ is a diagonal matrix with eigenvalues on the diagonal, and R is the temporal correlation matrix, which includes M number of the flow field data. The flow field can be decomposed into a set of eigenfunctions and mode coefficients

$$u(x, y, t_i) \approx \sum_{k=1}^{M} a_k(t_i)\, \sigma_k(x, y) \tag{16}$$

Where a_k is mode coefficient and σ_k is spatial eigenfunction. In the present study, snapshots were extracted at every time step. Total 1350 snapshots are collected and they are processed with a MATLAB script.

The POD modes allows for decomposing the optimal modes for the flow and capturing large-scale flow structures. In general, the first few POD modes capture 95% of the total kinetic energy. Figure 55 and Figure 56 show energy distribution for individual modes on horizontal and vertical plane. Specifically, the first mode has the most significant energy, ~91.76%, while it drops to 2.79% in the second mode. In addition, energy per POD mode is decreasing slowly after second POD mode. Figure 56 shows the

energy distribution for the vertical plane, while its first mode has 98.12% energy. It can be concluded that, the flow structure between snapshots is changing less significant on the vertical plane than on the horizontal plane. This behavior is the main reason of resolving more energy in the first mode of the vertical plane.

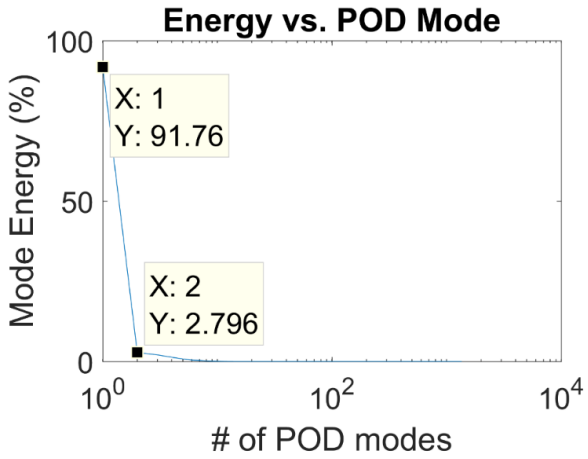

Figure 55: Mode energy vs. # of POD modes for horizontal plane.

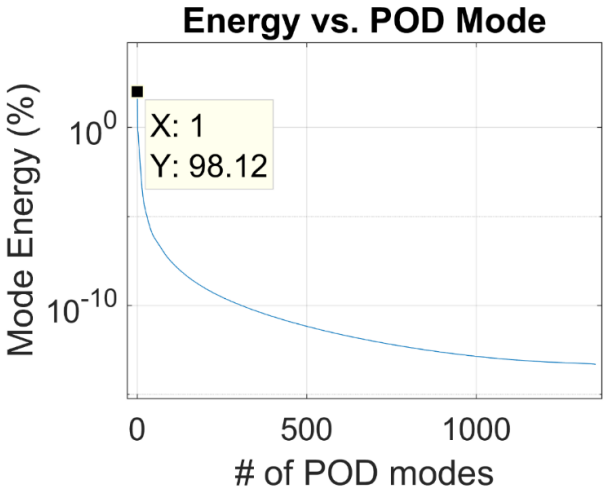

Figure 56: Mode energy vs. # of POD modes for vertical plane.

Figures 57- 61 show the first 5 most energetic POD modes of the secondary flow. The POD allows the extraction coherent turbulent structures and their evolution at lower energy modes. First mode is giving mean flow field of the snapshots, while the rest of the modes are giving dominant structures. In the second mode, it captures 2.8% energy, and some of structures that are induced by the wings are spotted. The rest of the modes shows lower energies, which is the decaying mechanism of the secondary flow. Since it stabilized at the downstream locations.

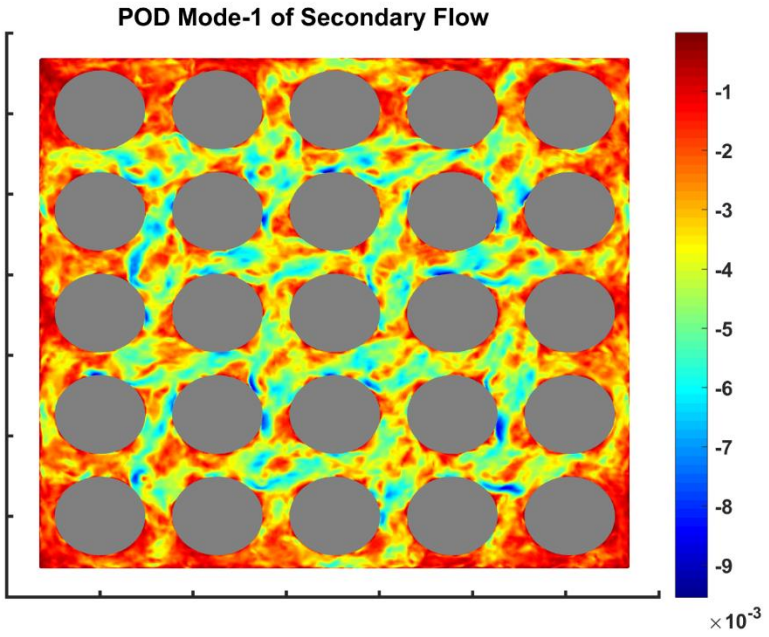

Figure 57: 1st mode of the POD for Secondary flow.

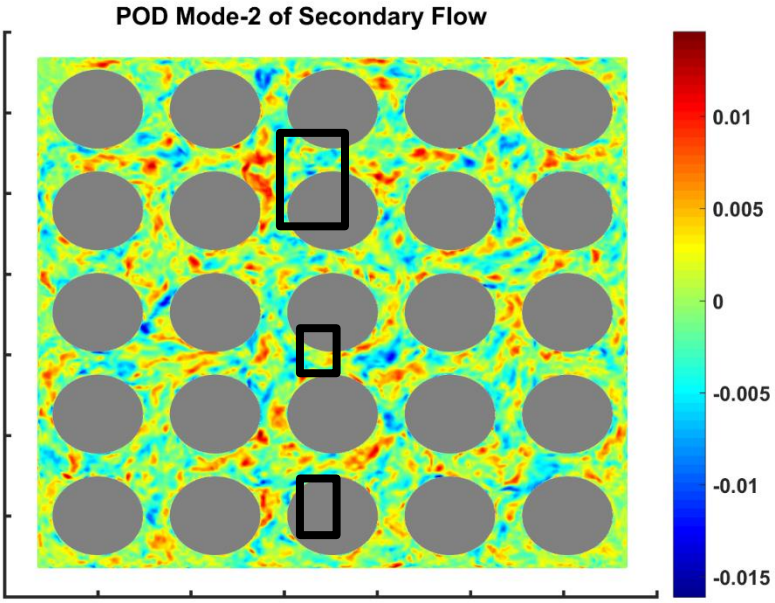

Figure 58: 2nd mode of the POD for Secondary flow.

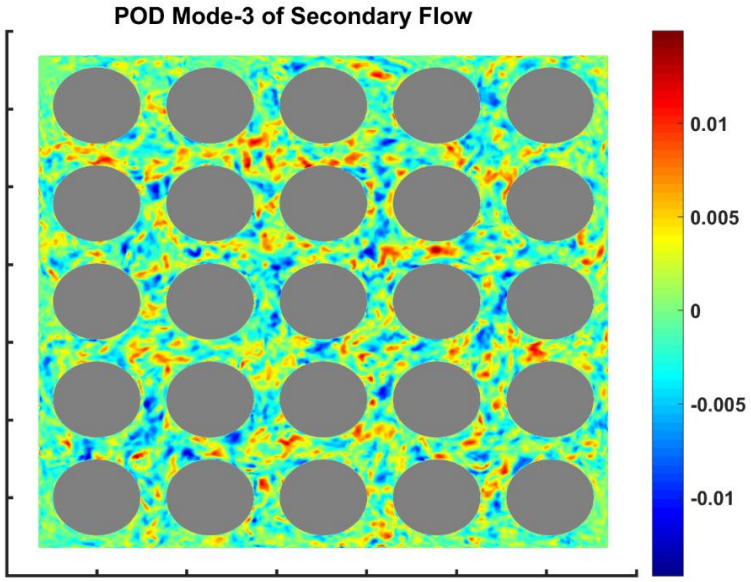

Figure 59: 3rd mode of the POD for Secondary flow.

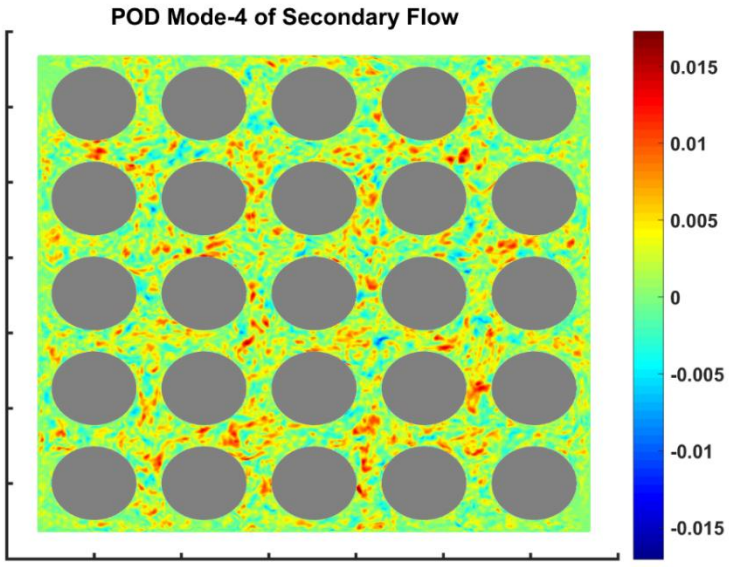

Figure 60: 4th mode of the POD for Secondary flow.

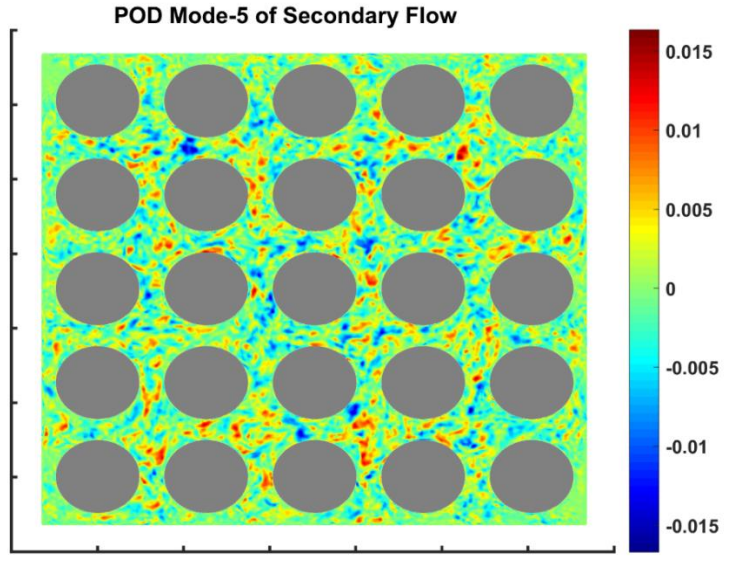

Figure 61: 5th mode of the POD for Secondary flow.

Figures 62- 66 show the first 5 most energetic POD modes and reconstruction with first two modes of the axial velocity. First mode is giving the mean flow field of the snapshots, while the rest of the modes are extracting dominant structures. The flow structures show the evolution of the axial velocity modes and the recovery of the axial velocity from secondary flow. Additionally, POD modes can serve for experimental data mode extraction and its higher resolution comparisons.

Finally, in Figure 67 shows the reconstruction from POD modes, mainly for verification purpose of the POD algorithm.

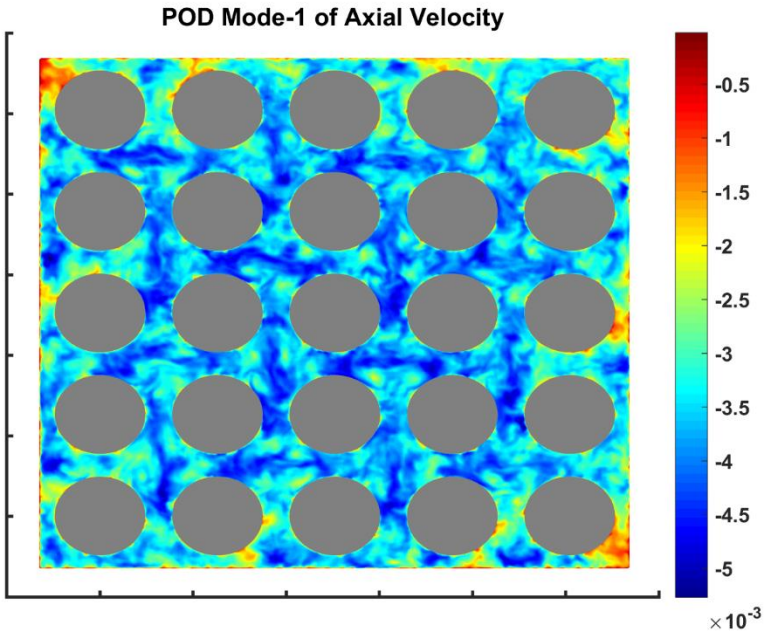

Figure 62: 1st mode of the POD for Axial Velocity.

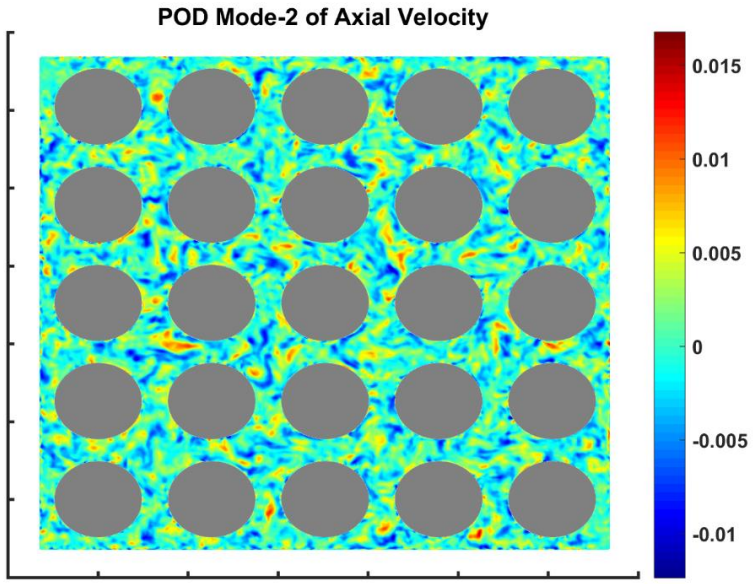

Figure 63: 2nd mode of the POD for Axial Velocity.

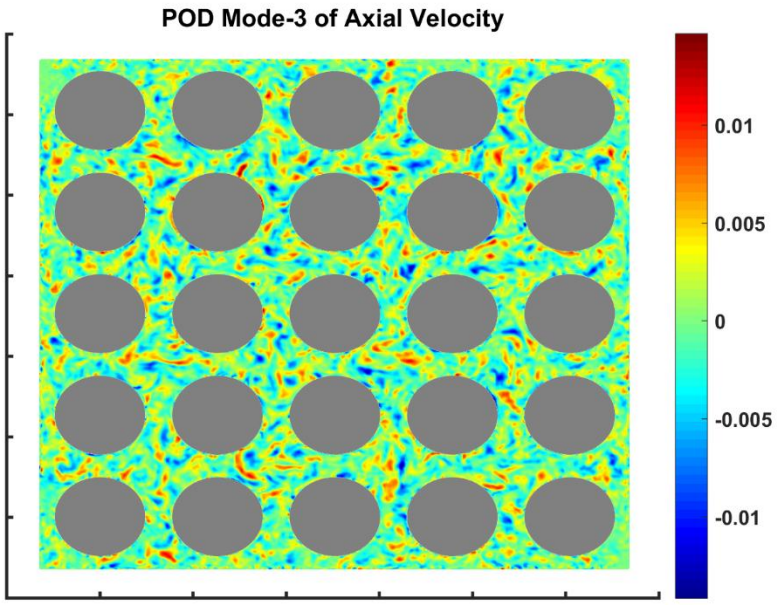

Figure 64: 3rd mode of the POD for Axial Velocity.

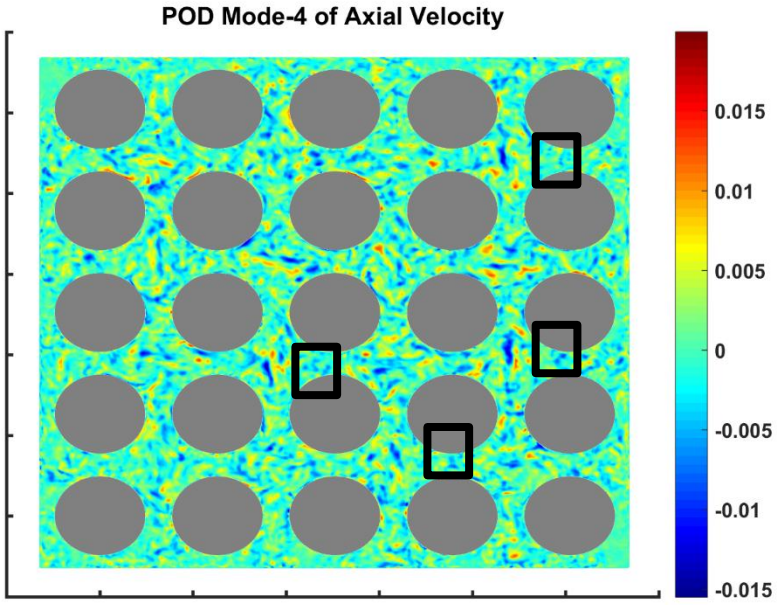

Figure 65: 4th mode of the POD for Axial Velocity.

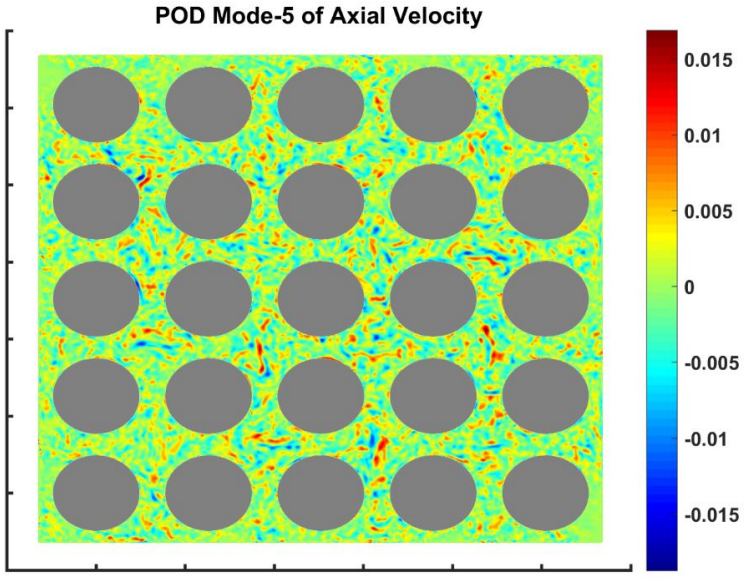

Figure 66: 5th mode of the POD for Axial Velocity.

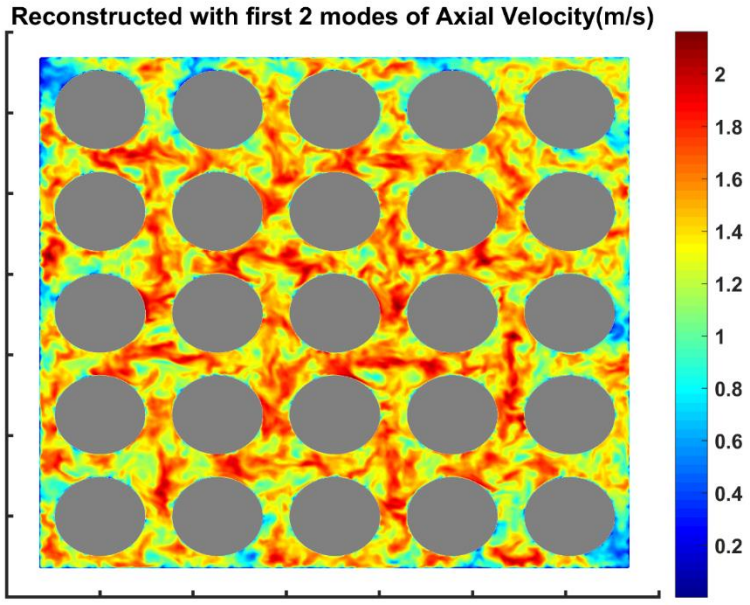

Figure 67: Reconstructed with 2 POD Modes for Axial Velocity.

In Figure 68, it can be seen that the most energetic mode is the mean of the axial velocity from snapshots. Other two modes shows less energetic modes, which extract the decay of the axial velocity. They are more significant downstream of the wing. The domain of the vertical plane in axial direction starts from top of the wing till at the end of the channel, which is 0.5 meter downstream from the top of the wing.

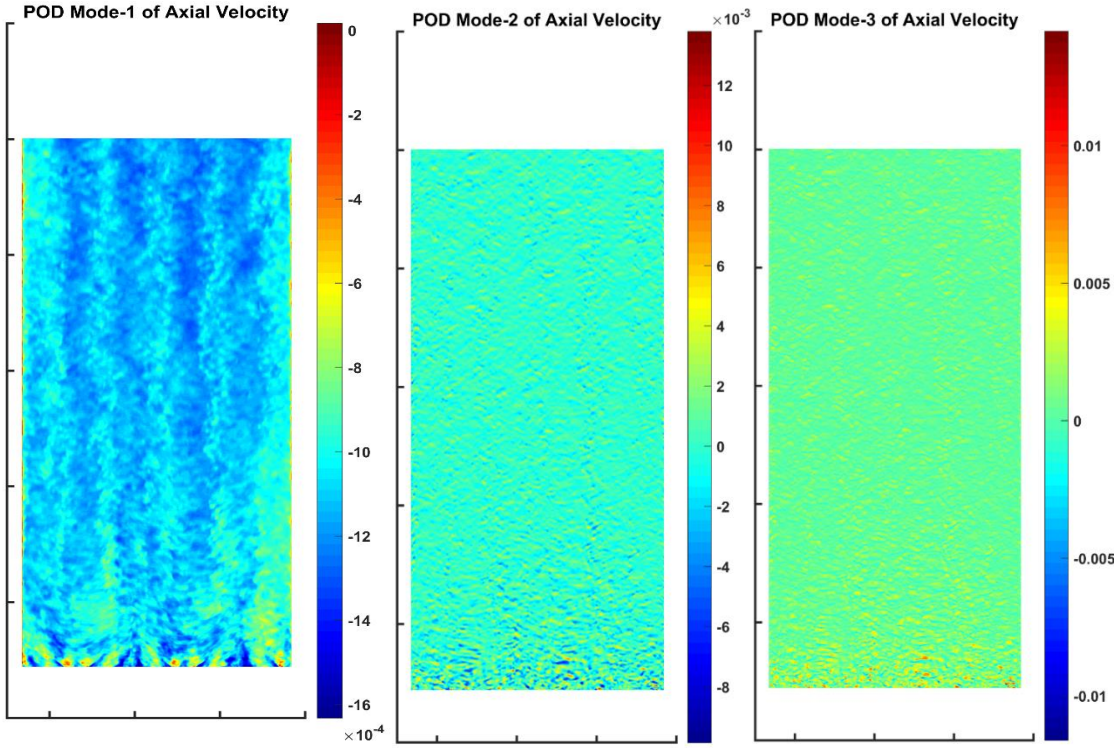

Figure 68: First 3 POD Modes for the Axial Velocity on Plane 1.

IV.6 Dynamic Mode Decomposition

Dynamic Mode Decomposition (DMD) is a technique that allows for a modal analysis of a flow field without using a numerical solver or an underlying model [29]. For a nonlinear flow, the decomposition produces modes that express the dominant dynamic behavior captured in the snapshots of the flow field. Defining a temporal linear operator **A** which advances our snapshot basis V(t) such that V(tn+1) = **A**V(tn); the DMD algorithm is able to extract eigenvalues and eigenmodes of a reduced-order representation of the linear operator **A** from the data sequence. For enough long sequences, each DMD-mode is linked to a single temporal frequency [30]. In this manner, DMD differs from the Proper

Orthogonal Decomposition which does not provide direct information concerning the frequency of the modes. First step for DMD, set of flow fields collected by sampling at sequential time steps as sequence of snapshots. Then snapshots should be ordered in the form of a snapshot sequence as given.

$$D_i^N = (d_1, d_2, \dots, d_N) \tag{17}$$

where *d* has the i-th flow field and data must have a constant sampling time Δt.

It is stated as linear mapping between d_i and d_{i+1} as given:

$$d_{i+1} = \mathbf{A}\, d_i \tag{18}$$

The assumption of a constant mapping between the snapshots allow for formulating flow field as a Krylov sequence

$$D_1^N = (d_1, A\, d_1, A^2 d_1, \dots . A^{N-1} d_1) \tag{19}$$

with enough number of the snapshots d_N will be linearly independent which in a matrix form as follows

$$d_N = D_1^{N-1}\, \mathrm{a} + r \tag{20}$$

with $\mathrm{a}^{\mathrm{T}} = (a_1, a_2, \ldots . a_{N-1})$ is the vector of the linear combination coefficients and r the residual vector. Using above relations, it is possible to write in matrix form as

$$\mathrm{A}\ \mathrm{D}_1^{N-1} = \mathrm{D}_2^N = \mathrm{D}_1^{N-1}\mathrm{S} + \mathrm{r}\ \mathrm{I}_{N-1}^{\mathrm{T}} \tag{21}$$

where the matrix S states a companion matrix

$$\mathrm{S} = \begin{bmatrix} 0 & & & a_1 \\ 1 & 0 & \cdots & a_2 \\ \vdots & 1 & \ddots & \vdots \\ & & \cdots & a_{N-2} \\ & & 1 & a_{N-1} \end{bmatrix} \tag{22}$$

The only unknown in S are the **a** coefficients, which is given above as linear approximation of last sample d_N in terms of previous samples. Full rank matrix can be calculated D_1^{N-1} as given $\mathrm{a} = \mathrm{R}^{-1}\mathrm{Q}\ \mathrm{d}_{\mathrm{N}}$ with $\mathrm{D}_1^{N-1} = \mathrm{QR}$.

Even decomposition on companion matrix S is correct, practical implementation produces singularity, which only allow to extract only first one or first two modes. As a solution a more robust method is used to compute full matrix $\tilde{\mathrm{S}}$ via similarity transformation. The robustness requirement is achieved by a singular value decomposition of the data $\mathrm{D}_1^{N-1} = \mathrm{U}\Sigma\mathrm{V}^{\mathrm{H}}$, it can be obtained as $\tilde{\mathrm{S}} = \mathrm{U}^{\mathrm{H}}A\mathrm{U} = \mathrm{U}^{\mathrm{H}}D_2^N\mathrm{V}\Sigma^{-1}$. Dynamic modes can be obtained as below.

$$\Phi_i = \mathrm{U}\Lambda_\mathrm{i} \quad \text{with} \quad [\Lambda_i, \lambda_i] = eiv(\tilde{\mathrm{S}}) \tag{23}$$

where Λ_i as the i-th eigenvector of $\tilde{\mathrm{S}}$, $\tilde{\mathrm{S}}\Lambda_i = \lambda_i\Lambda_i$ and U as the right singular vectors of the snapshot sequence D_1^{N-1}.

Figure 69 shows that nearly all the Ritz values are on the unit circle indicating that the snapshots lie on an attracting set. The growth rate of each DMD mode is plotted versus its frequency in Figure 70. The spectrum appears symmetric with respect to the imaginary axis at origin 0, which is a consequence of processing real-valued data. Indeed, in that particular case, the eigenvalues and associated eigenvectors are real or complex conjugate. At this point, the Ritz eigenvectors are available for the design of a reduced-order model. The most amplified mode (mode 1) corresponds to the mean flow at the origin.

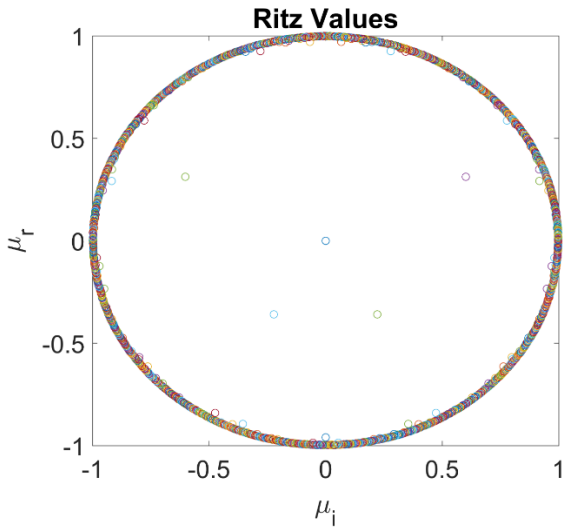

Figure 69: Ritz values.

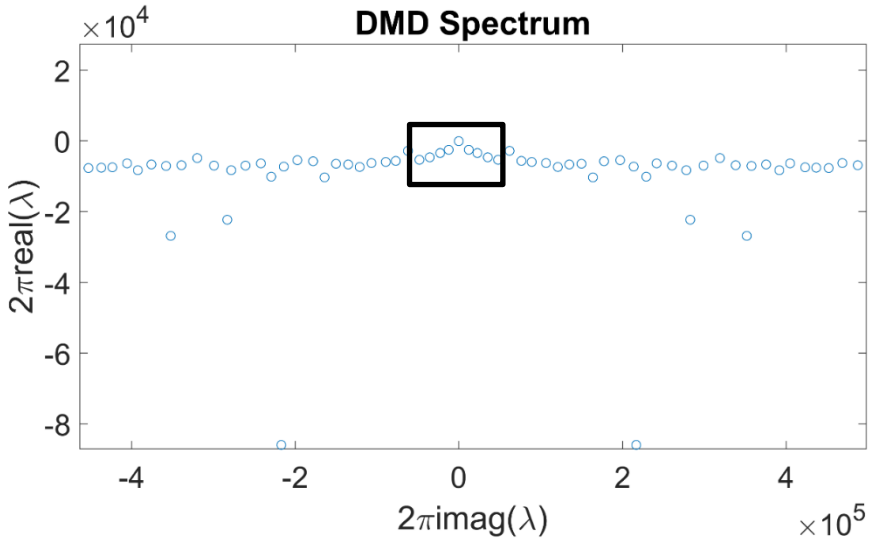

Figure 70: DMD spectrum imaginary vs. real eigenvalues.

DMD modes are ordered and amplitude vs. mode number is plotted in Figure 71, which can be extracted also from Figure 72.

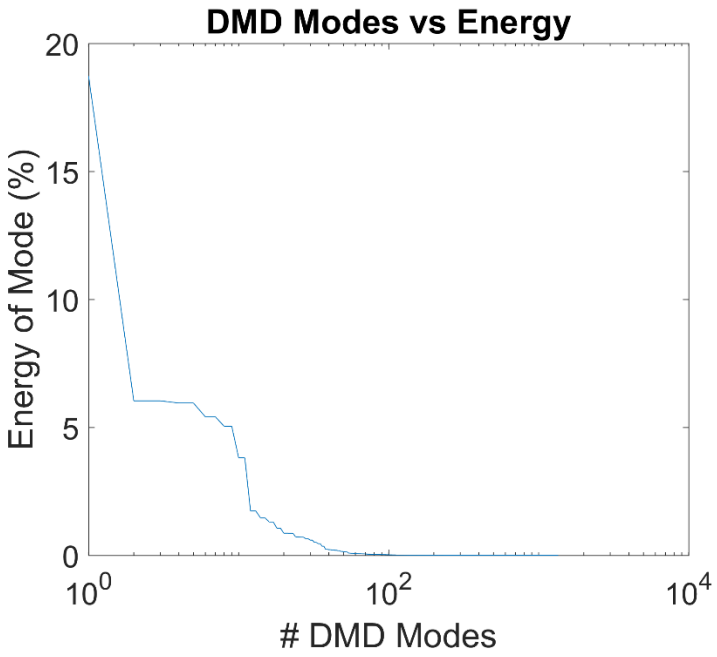

Figure 71: DMD Modes vs. Energy.

In Figure 72, the amplitude of the DMD modes are plotted against frequency of the mode itself. It shows dominant mode at frequency 2x10^5 Hz. Also it proves that the inertial subrange is resolved due to characteristic slope of the inertial subrange of the turbulence. This methodology is similar to FFT, which was done previously on different points. This method allows to do global spectrum analysis on all of the available grid points.

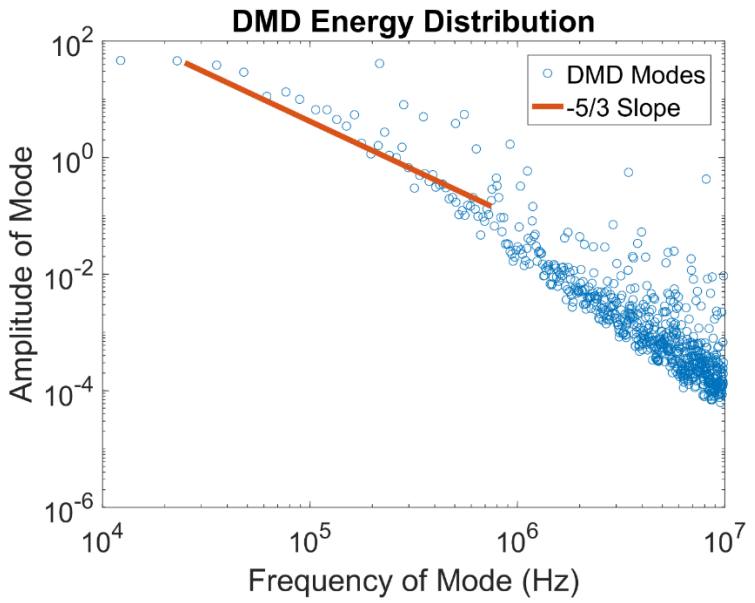

Figure 72: DMD mode Energy distribution vs. Frequency of Mode.

Figures 73-77 show the first 5 most energetic DMD modes of the axial velocity. The DMD allows to extract coherent turbulent structures and their temporal evolution, which is main difference from POD. Since POD is only able to extract spatial dominant structures, while the DMD is extracting temporal evolution of the dominant structures. First mode is giving mean flow field of the snapshots, while the rest of the modes are giving dominant structures. The first two modes are very similar to POD modes, while the rest of the modes have different behaviors than POD modes. Especially, the structures from POD mode-4 are not captured on DMD mode-4, on the other hand similar structures can be observed at DMD mode-5.

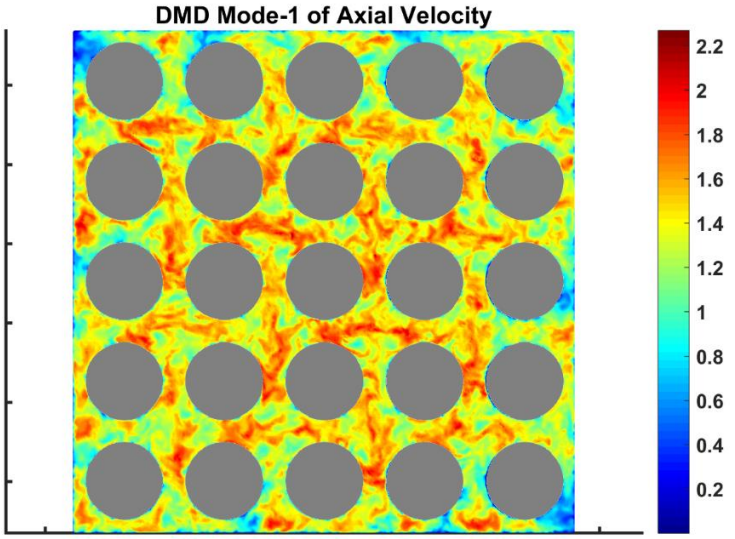

Figure 73: 1st mode of the DMD for Axial Velocity.

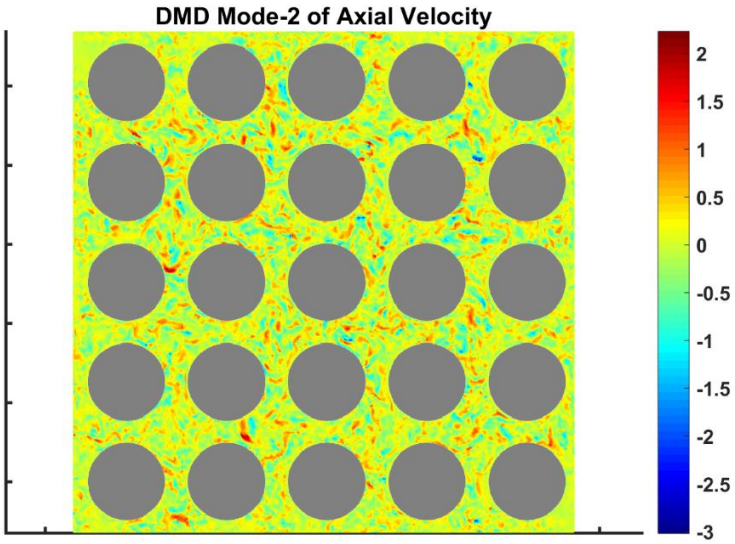

Figure 74: 2nd mode of the DMD for Axial Velocity.

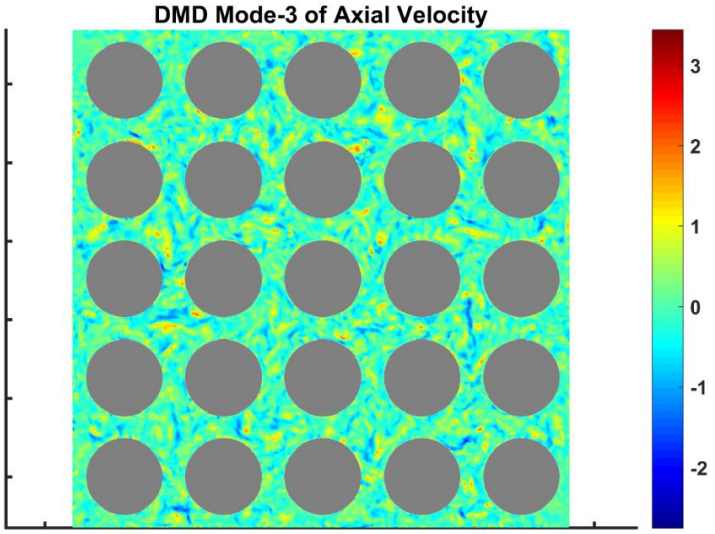

Figure 75: 3rd mode of the DMD for Axial Velocity.

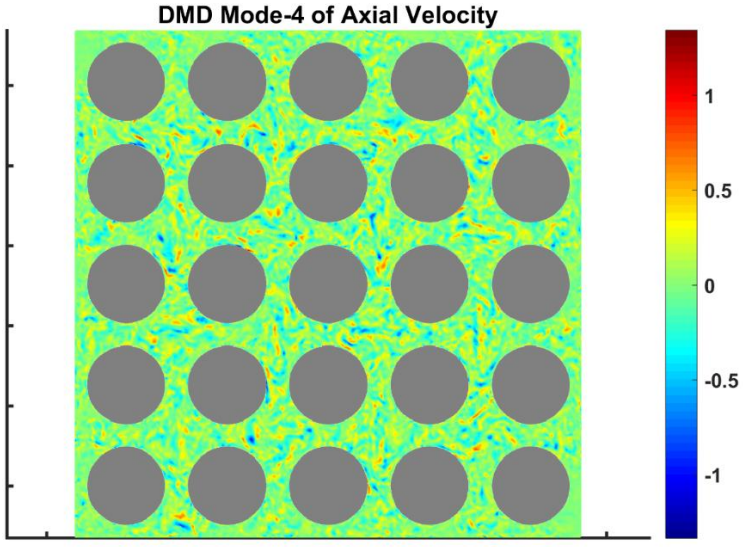

Figure 76: 4th mode of the DMD for Axial Velocity.

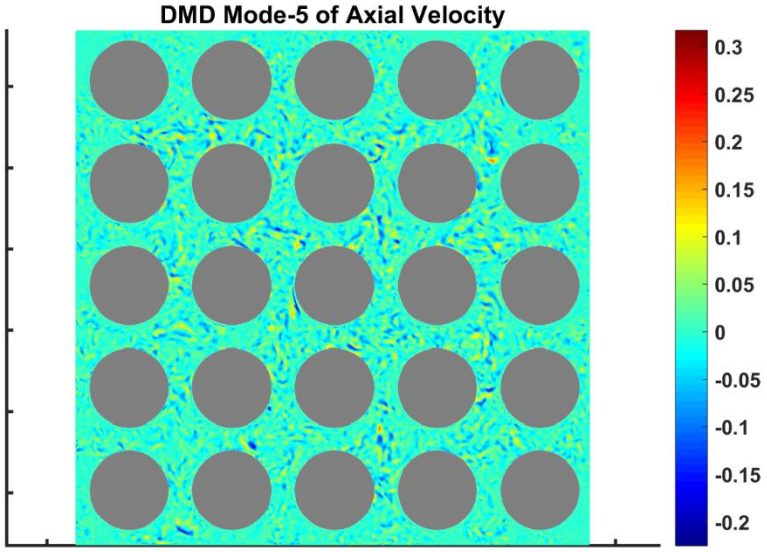

Figure 77: 5th mode of the DMD for Axial Velocity.

Figures 78-82 show the first 5 most energetic DMD modes of the secondary flow. The DMD allows the extraction of the coherent turbulent structures and their temporal evolution, which is the main difference from POD. POD is only able to extract spatial dominant structures, while the DMD is extracting temporal evolution of the dominant structures. The first mode of DMD is giving mean flow field of the snapshots, while the rest of the modes are giving dominant structures. The first two modes are very similar to POD modes, while the rest of the modes have different behaviors than POD modes.

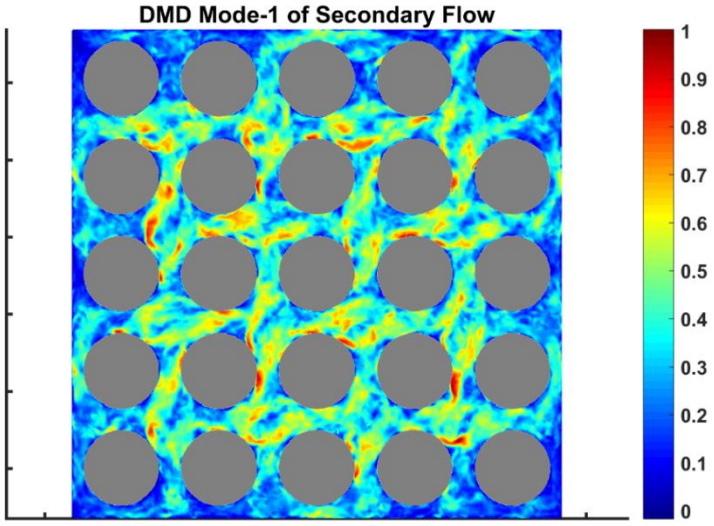

Figure 78: 1st mode of the DMD for Secondary Flow.

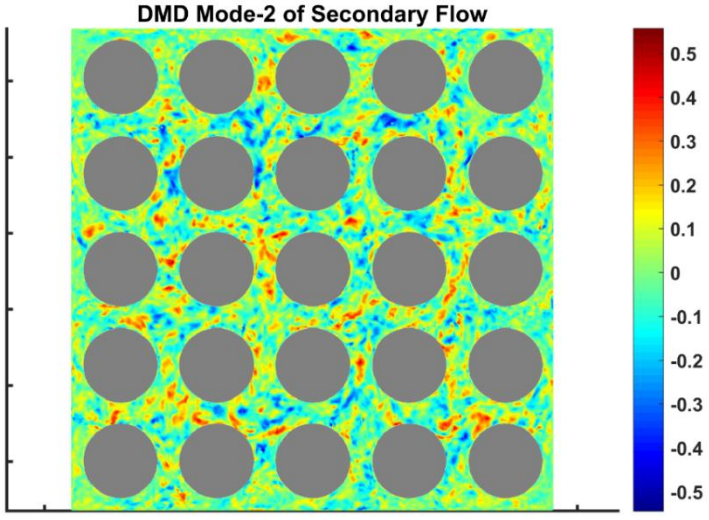

Figure 79: 2nd mode of the DMD for Secondary Flow.

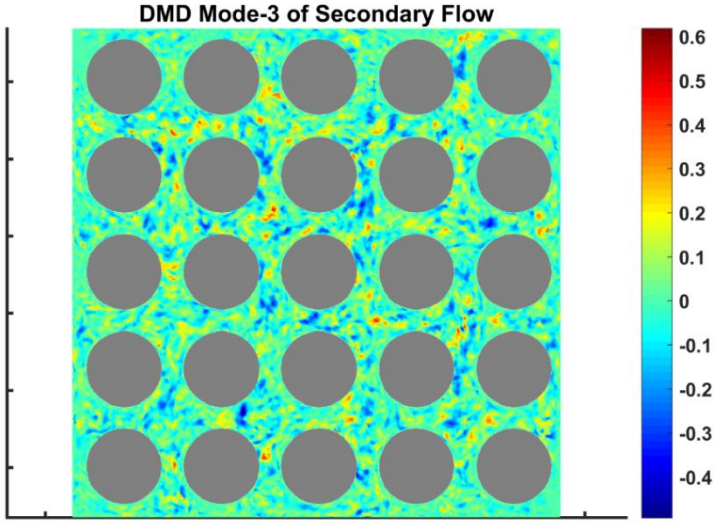

Figure 80: 3rd mode of the DMD for Secondary Flow.

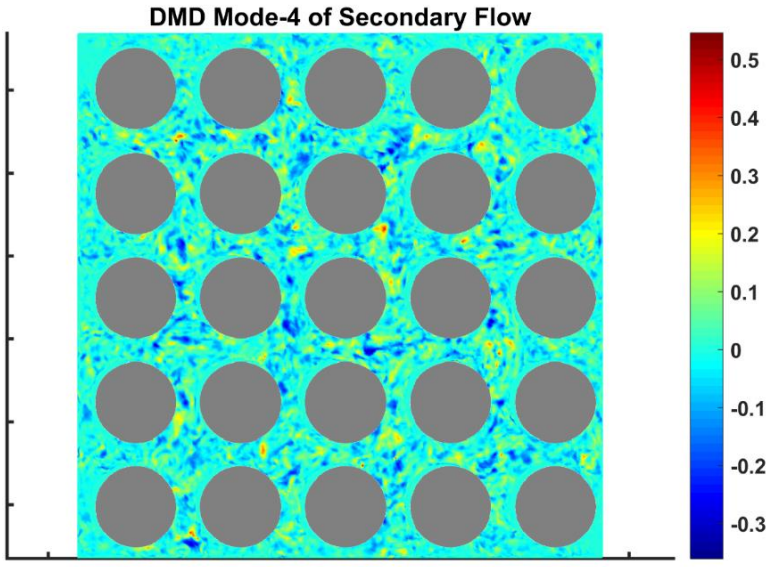

Figure 81: 4th mode of the DMD for Secondary Flow.

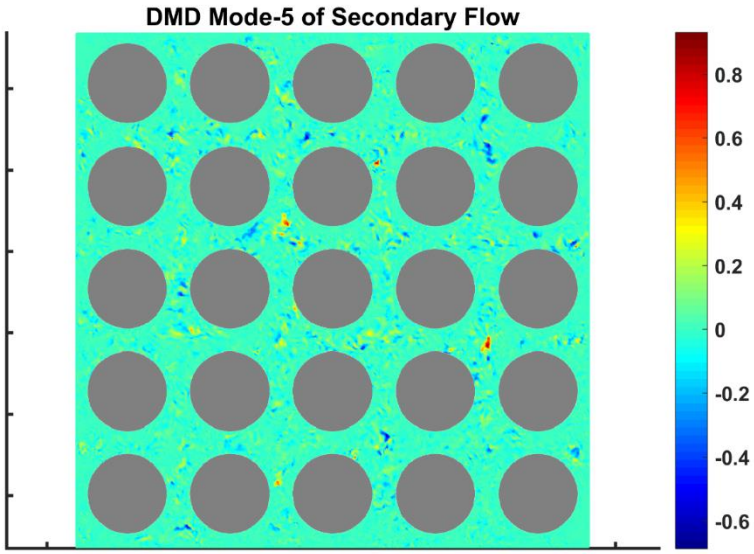

Figure 82: 5th mode of the DMD for Secondary Flow.

In Figure 83 shows that most energetic mode as mean of the axial velocity from snapshots. Other two modes shows less energetic modes, which extract the decay of the axial velocity. There are more significant at downstream of the wing. The domain of the vertical plane in axial direction starts from the top of the wing till the end of the channel, which is 0.5 meter downstream from the top of the wing. The dominant modes are captured in similar locations with POD modes, but as shown in Figure 84, the structure of the flow is slightly different than POD modes due to temporal evolution of the structures.

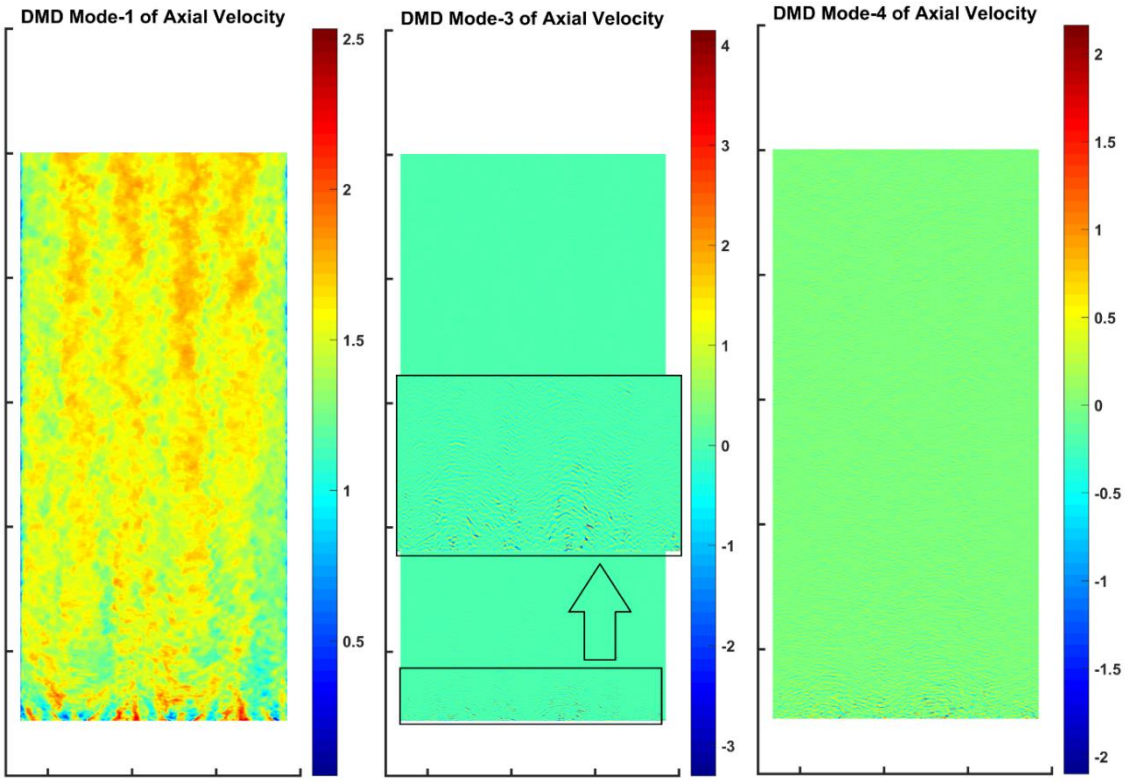

Figure 83: DMD modes for Axial Velocity on Plane 1.

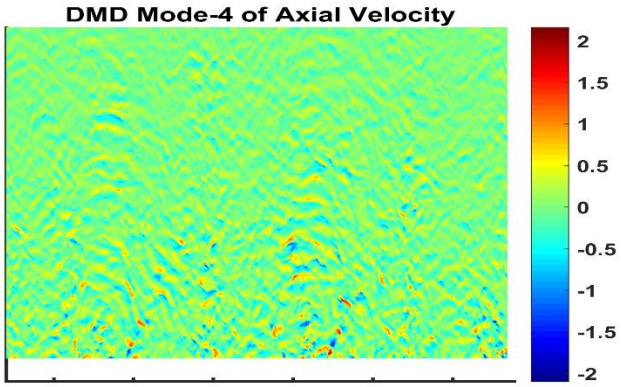

Figure 84: Zoom in on 4th mode of Axial Velocity.

IV.7 Experimental and Simulation Results

IV.7.1 Quantitative Comparison

In CFD grade validation, local values in high gradient region of the flow have to be analyzed with point by point comparison. Presents study focused on measurements on most challenging region of the flow domain. It starts 2.77 hydraulic diameter downstream of the mixing vane and up to 5.55 hydraulic diameter. In fluid mechanics, first order parameters such as velocity, pressure or temperature can be converge to their mean values faster than any higher order values such as variances or covariance of the first order parameters. On the other, while it is crucial to have right values of the first order parameters, higher order statistics are vital for multi-physics applications such as fluid structure interaction or conjugate heat transfer. Thus, first order parameters are analyzed as three dimensional velocity components. In addition to that, square root of the variances of the velocities, which is root mean square velocity, are compared against experimental data.

In Figures 85-90 shows velocity components along horizontal axis from both experiment and LES at every 5mm on plane 1. In general, lateral components has good agreement regarding the shape of the flow structure and magnitude of the values. When the comparison line moves downstream direction, overall agreement between experiment and LES is increasing. One of the possible reasons is that the flow has less swirling at downstream location, which may reduce experimental uncertainty at downstream location. U and W components of the velocity are capturing most of the peaks in both experimental and numerical simulations, while it does not have the same performance in axial direction.

One of the possible reasons is that the magnitude of the axial velocity is significantly higher in axial direction, which may cause higher experimental uncertainty.

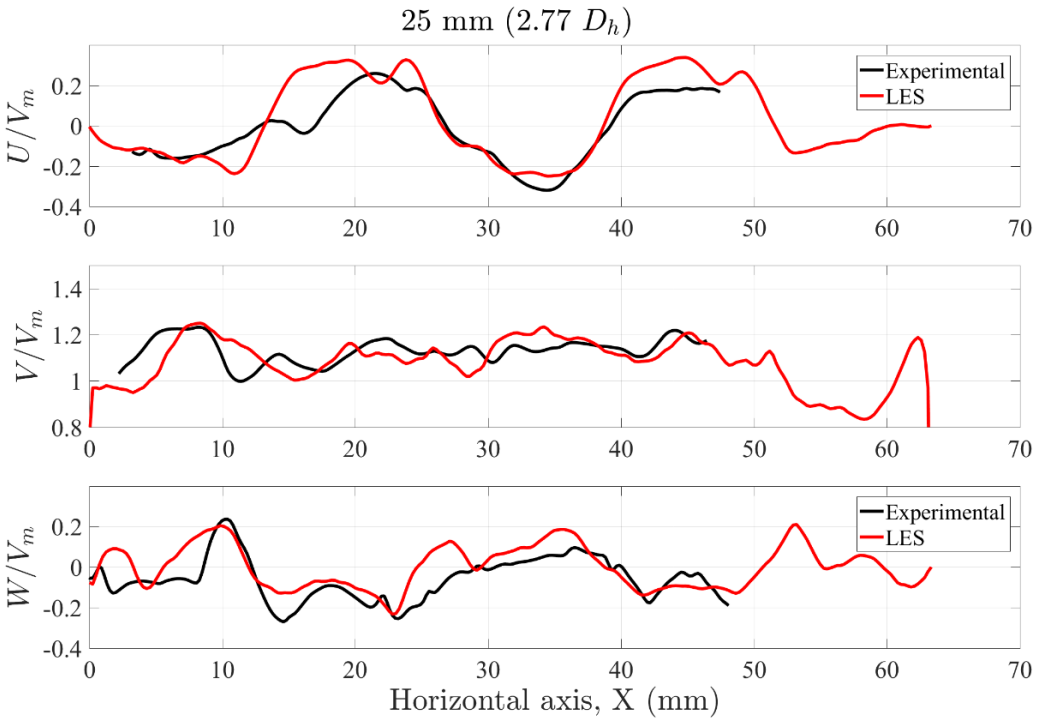

Figure 85: Experimental vs. LES Velocity comparison on plane 1 at 25 mm.

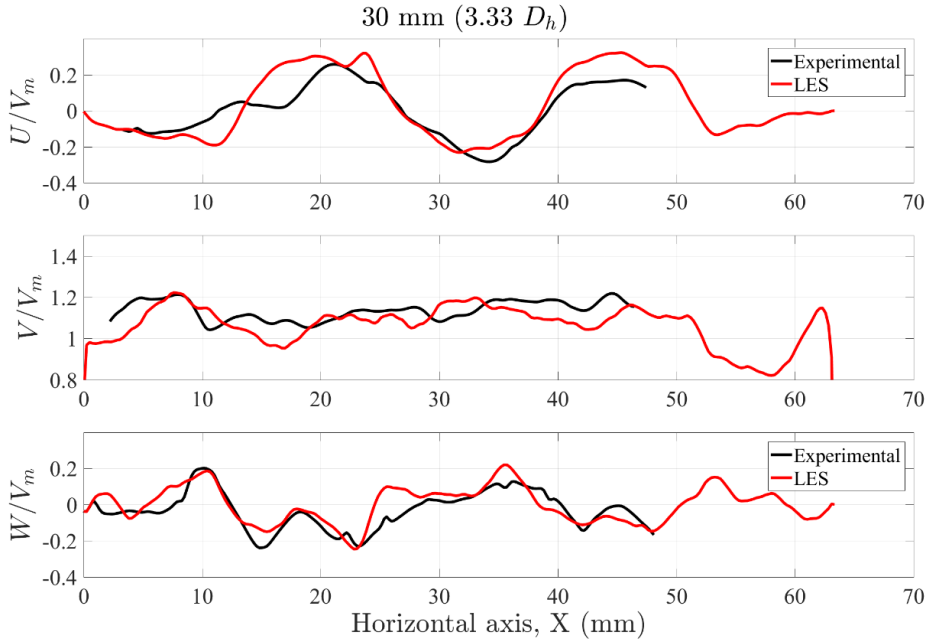

Figure 86: Experimental vs. LES Velocity comparison on plane 1 at 30 mm.

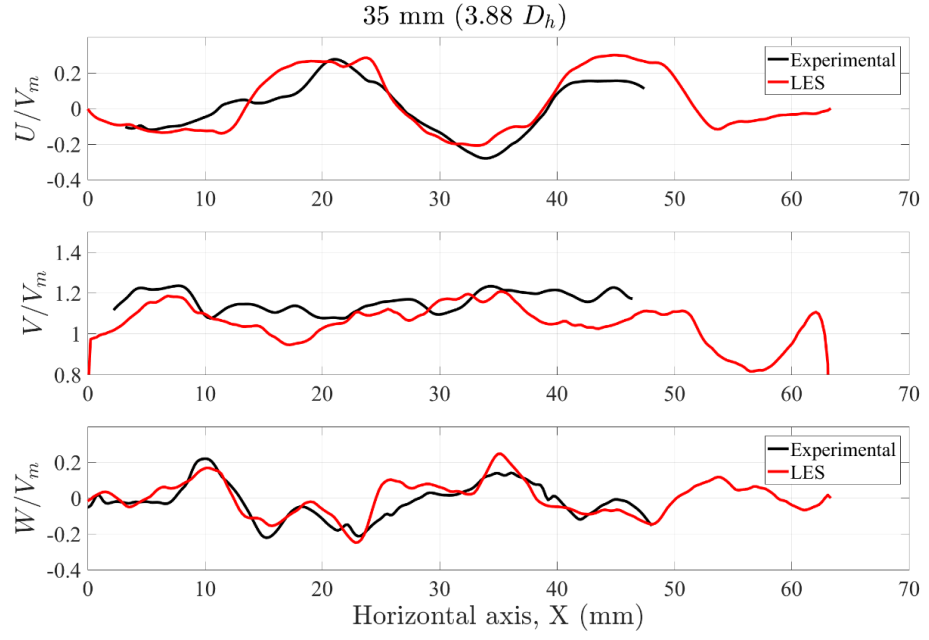

Figure 87: Experimental vs. LES Velocity comparison on plane 1 at 35 mm.

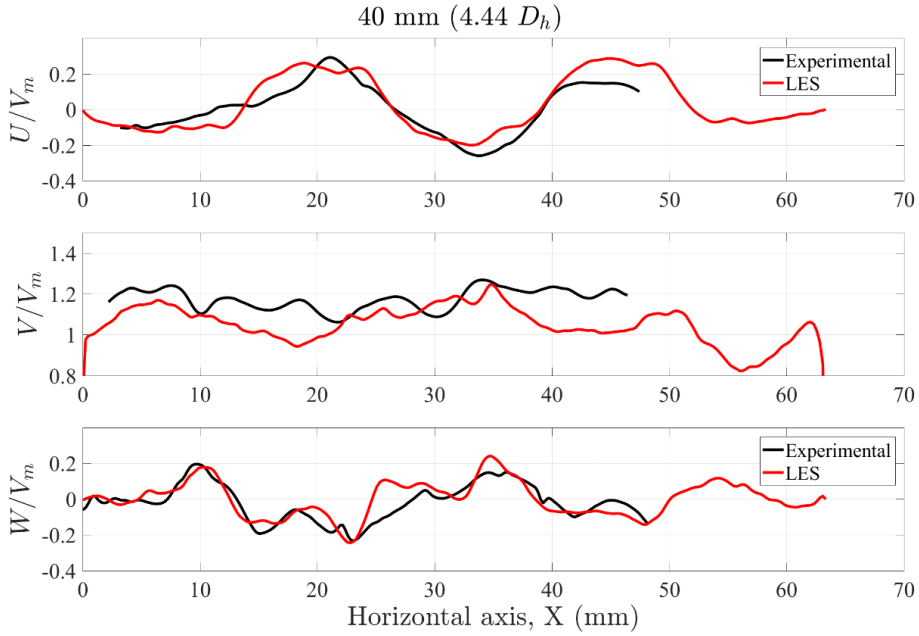

Figure 88: Experimental vs. LES Velocity comparison on plane 1 at 40 mm.

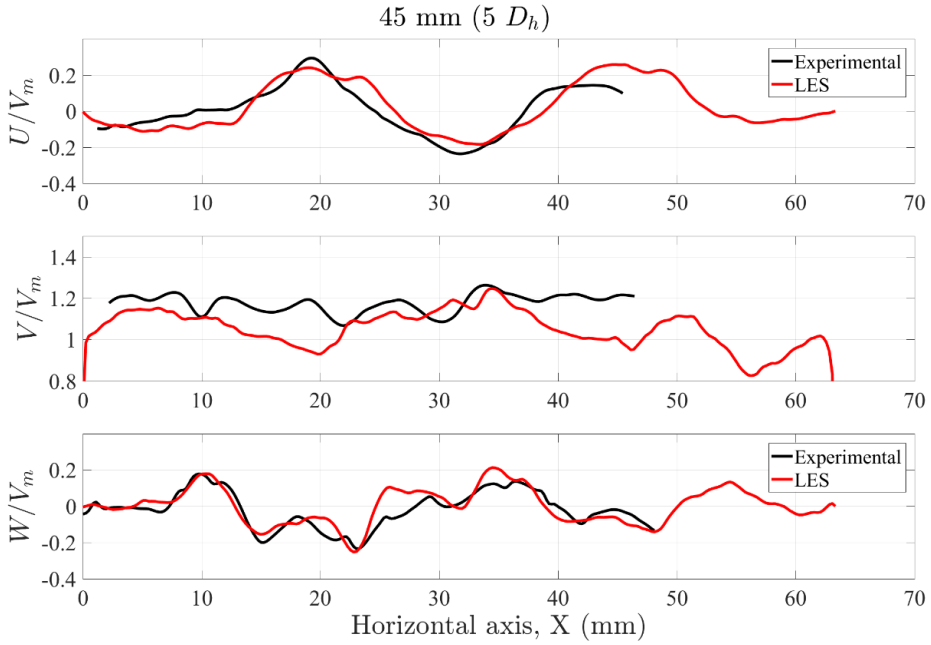

Figure 89: Experimental vs. LES Velocity comparison on plane 1 at 45 mm.

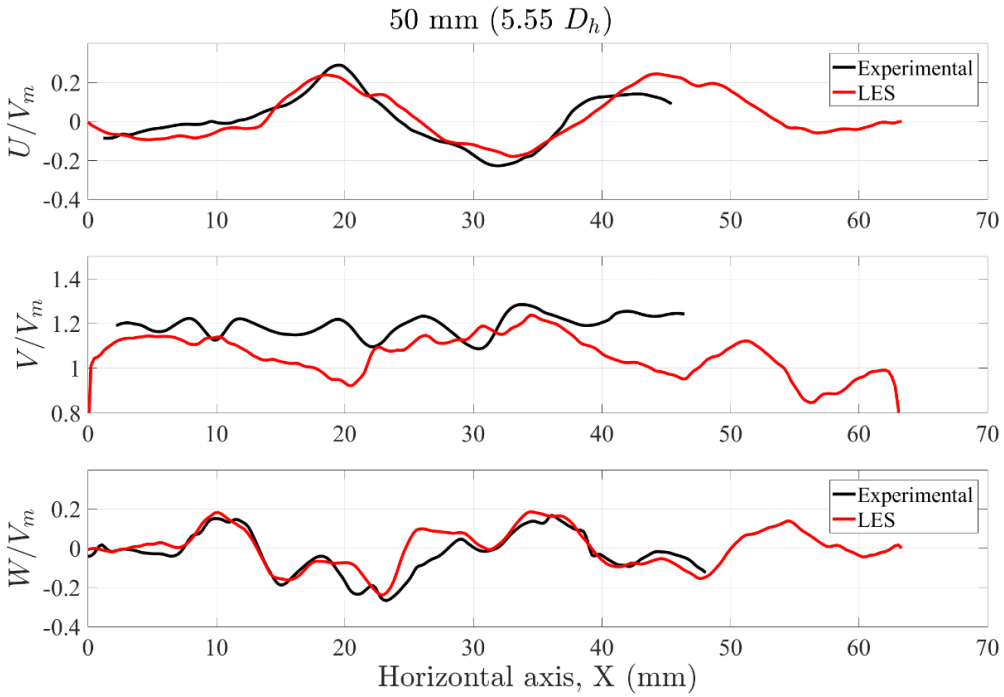

Figure 90: Experimental vs. LES Velocity comparison on plane 1 at 50 mm.

In Figures 91-96 show the root mean squares (RMS) of the velocity components along horizontal axis from both experiment and LES at every 5mm. In general, the magnitude of the values are not performing as good as velocity components. Since statistical values needs more sampling and depend highly on the number of the sampling. On the other hand, lateral components trends are matching with experimental data, even there is a magnitude difference. However, it is not the case for the axial velocity, since the magnitude of the fluctuation is higher in axial direction, which needs even higher number of sampling.

The magnitude of the axial RMS component is getting closer to the experimental results, when the horizontal line moves down, this happens mainly due to the level of the

RMS decreasing in the LES simulation. In fluid mechanics point of view, right after the wings the secondary flows caused higher fluctuations, also it enhance turbulence. So therefore, turbulent kinetic energy also increases and then it decays due to the stabilizations of the secondary flow at the downstream location. Those are directly correlated with RMS, since it is the measure of the turbulence intensity. Physically the RMS values should be decreased at downstream location. Therefore, experimental RMS values at upstream location should be investigated in terms of the sampling frequency and amount of the samples. In conclusion, it can be seen in the axial component of the RMS figures, the characteristic peak of the boundary layer at near wall is captured.

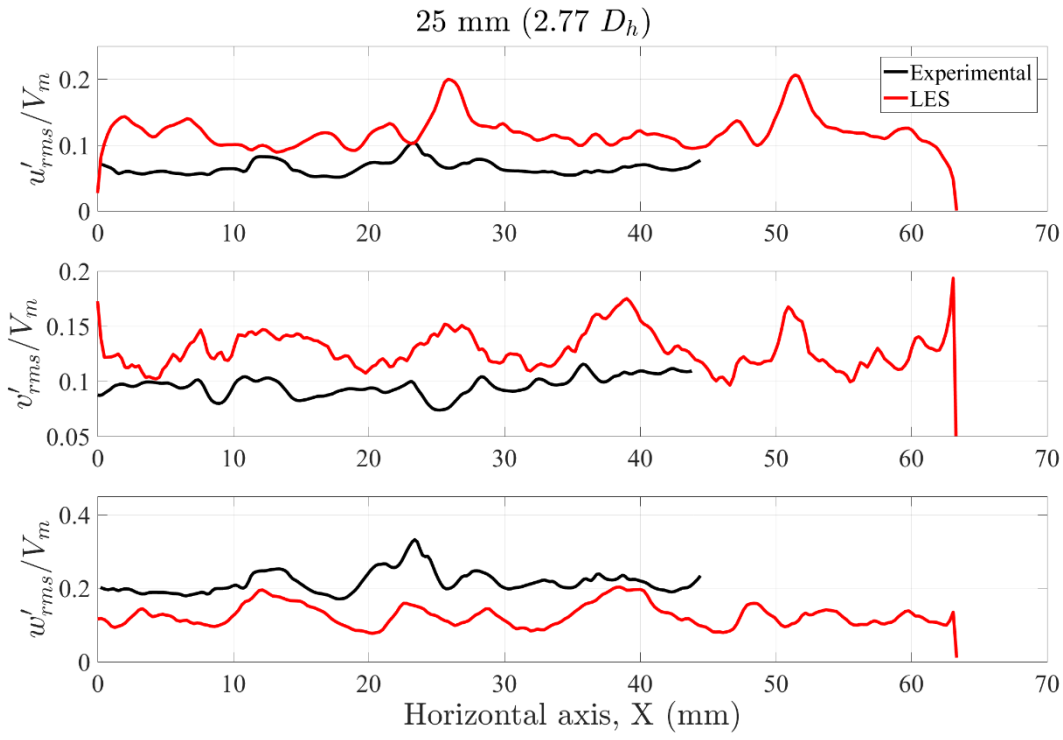

Figure 91: Experimental vs. LES RMS Velocity comparison on plane 1 at 25 mm.

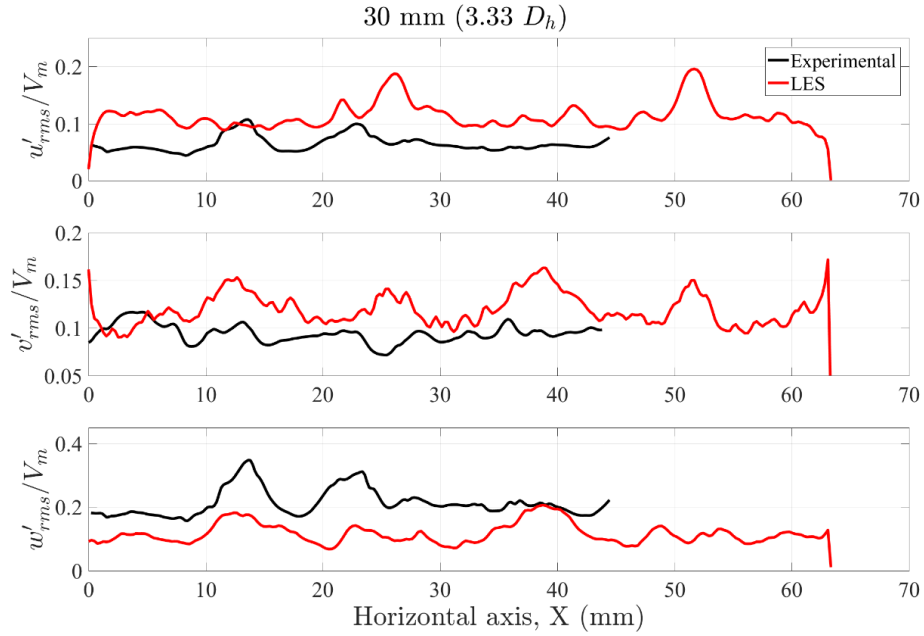

Figure 92: Experimental vs. LES RMS Velocity comparison on plane 1 at 30 mm.

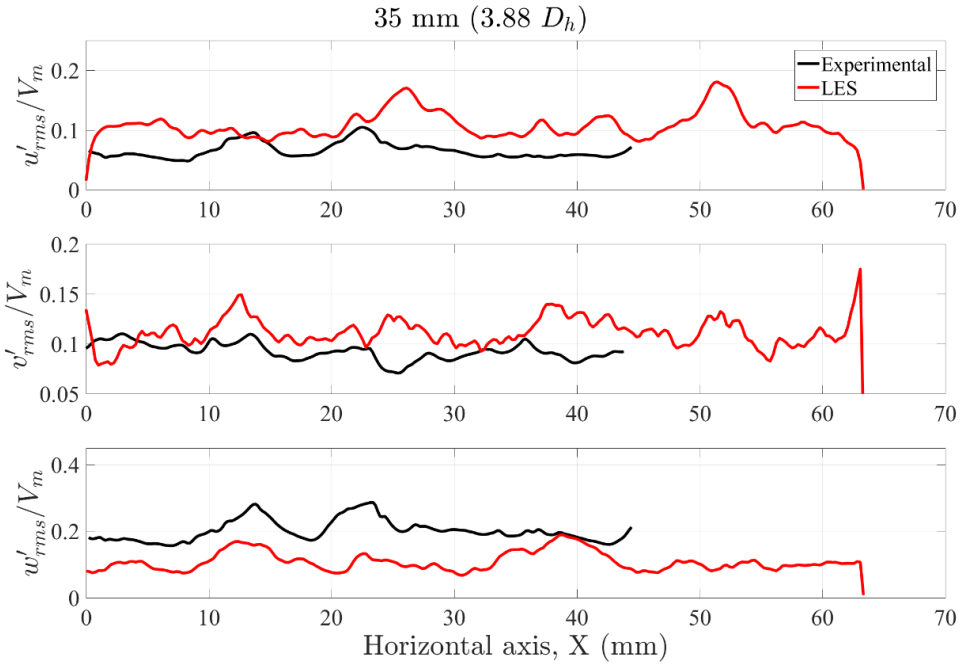

Figure 93: Experimental vs. LES RMS Velocity comparison on plane 1 at 35 mm.

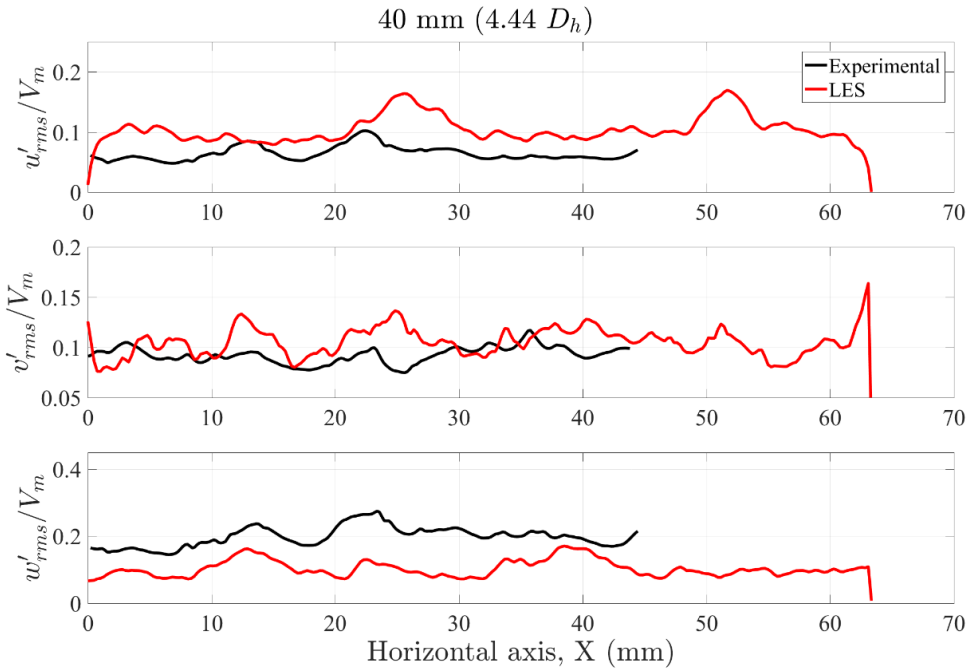

Figure 94: Experimental vs. LES RMS Velocity comparison on plane 1 at 40 mm.

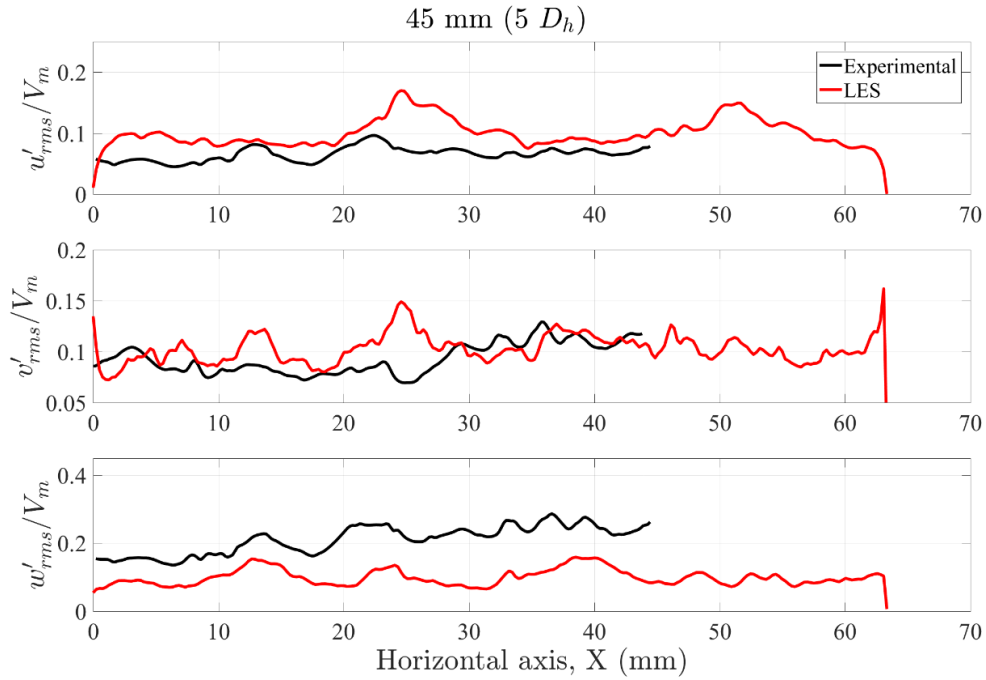

Figure 95: Experimental vs. LES RMS Velocity comparison on plane 1 at 45 mm.

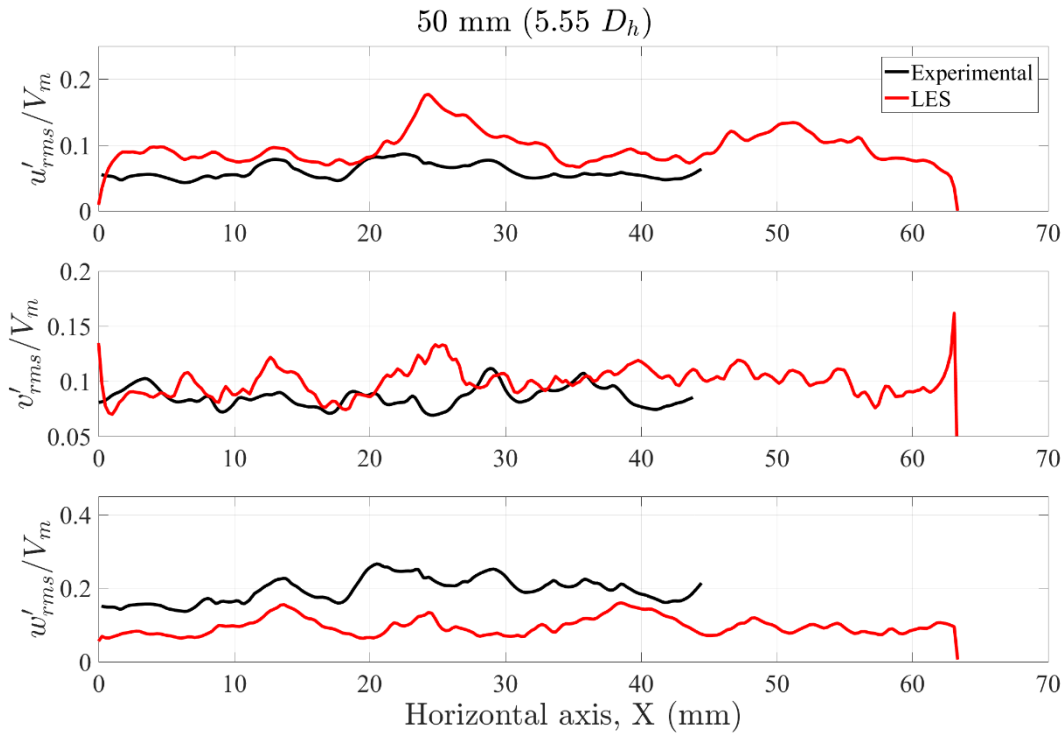

Figure 96: Experimental vs. LES RMS Velocity comparison on plane 1 at 50 mm.

IV.7.2 Qualitative Scalar Plot Comparison

In this part of chapter IV, experimental and numerical results are compared qualitatively on contour plots. Figure 97 is showing measurement planes. Measurement are taken on two vertical planes, experimental measurement starts at 24 mm downstream of the mixing vane and same regions are zoomed in on CFD simulations.

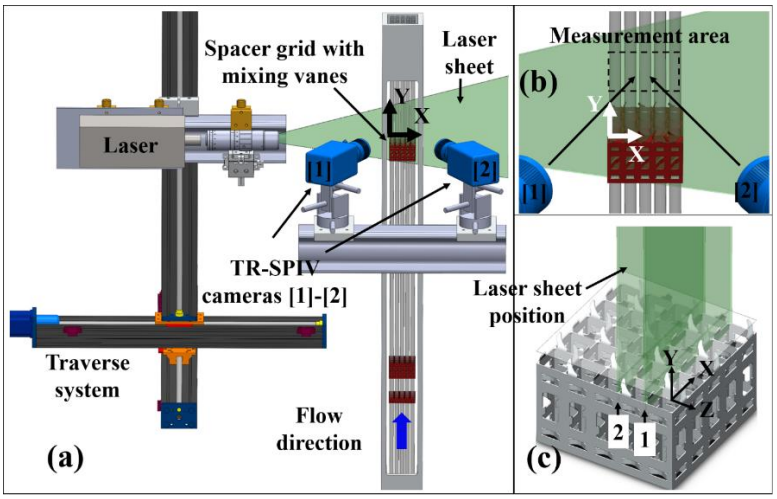

Figure 97: Experimental measurement planes 1-2.

In this part of Chapter IV, experimental and CFD results are compared on the same plane as contour plots. The parameters are not non-dimensionalized, which is it not a problem, since the mean velocities are taken from experimental volumetric flow rate. In Figure 98, time averaged U velocity component for the experiment and simulation are shown on plane 1. As it can be seen flow structures are captured well in both experiment and numerical results. There are uncertainties in the experimental data, specifically on the borders of the measurements.

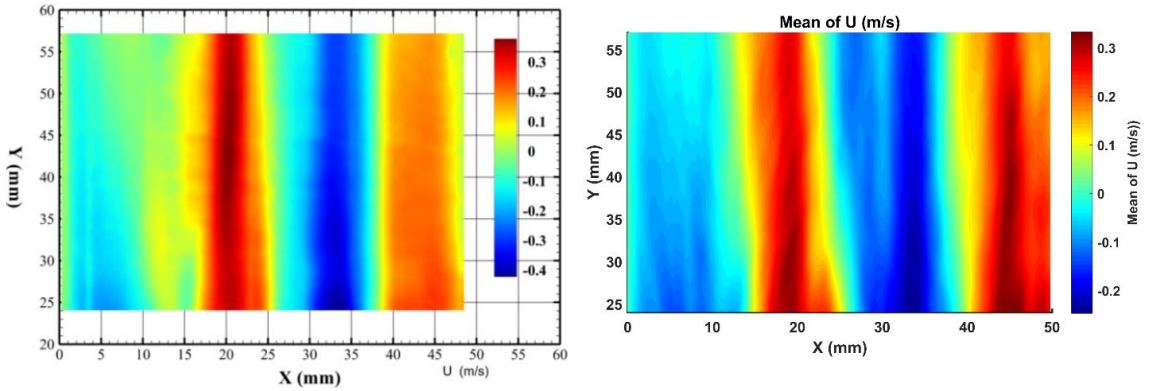

Figure 98: Time averaged U velocity from Exp. (left) and LES (right) on plane 1.

In Figure 99, time averaged V velocity component for the experiment and simulation are shown on plane 1. The magnitude of the axial velocity and gradients of it are very close each other between experiment and CFD, which uncertainty for axial components makes it harder to compare fairly. However columnar structures of the flow are captured in both of them.

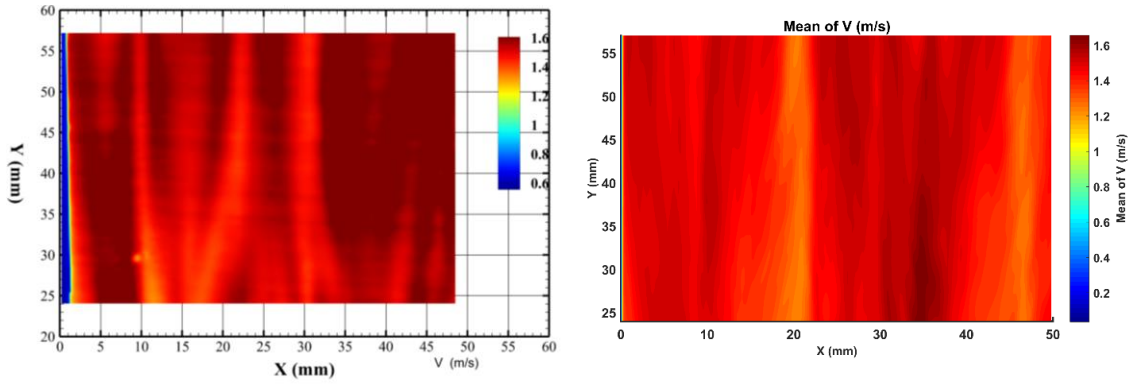

Figure 99: Time averaged V velocity from Exp. (left) and LES (right) on plane 1.

In Figure 100, time averaged W velocity component for the experiment and simulation are shown on plane 1. As it can be seen flow structures are captured well in both experiment and numerical results as in U velocity component. However the convergence of the experimental value is less than U component. Columnar flow structures is a proof that LES is capable to capture actual flow physics with higher resolution than experiments. In Figure 101, the behavior of the turbulence kinetic energy are captured with good agreement.

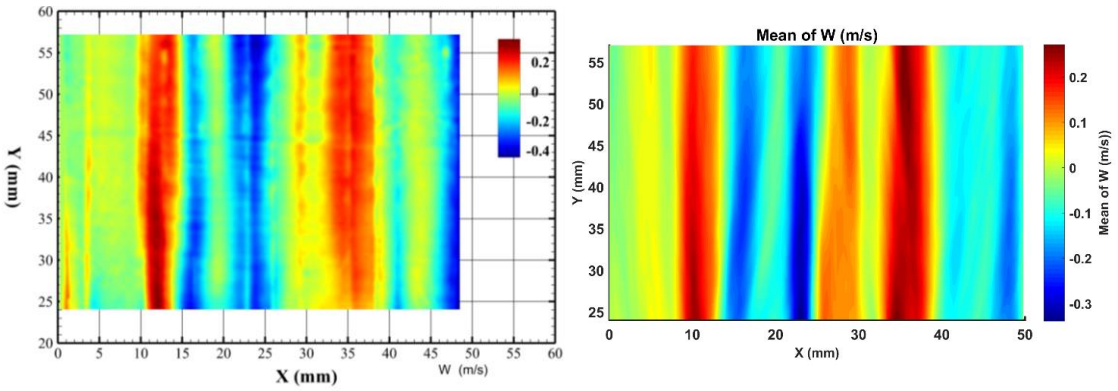

Figure 100: Time averaged W velocity from Exp. (left) and LES (right) on plane 1.

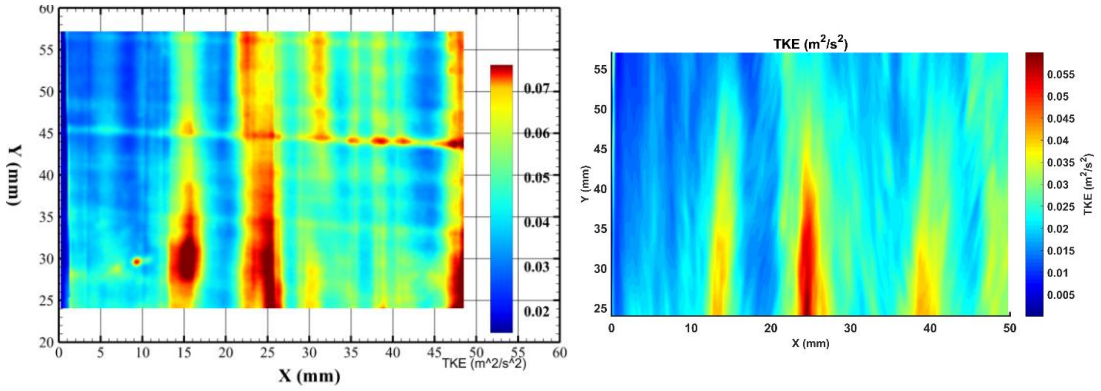

Figure 101: Time averaged TKE from Exp. (left) and LES (right) on plane 1.

In Figure 102, time averaged U velocity component for the experiment and simulation are shown on plane 2. As it can be seen that flow structures are captured in both experiment and numerical results. However, same measurement on plane 1 was giving higher resolution and better match, one of the possible reasons, is that plane 2 is behind of plane 1, so there are more obstacles between measurement plane and camera.

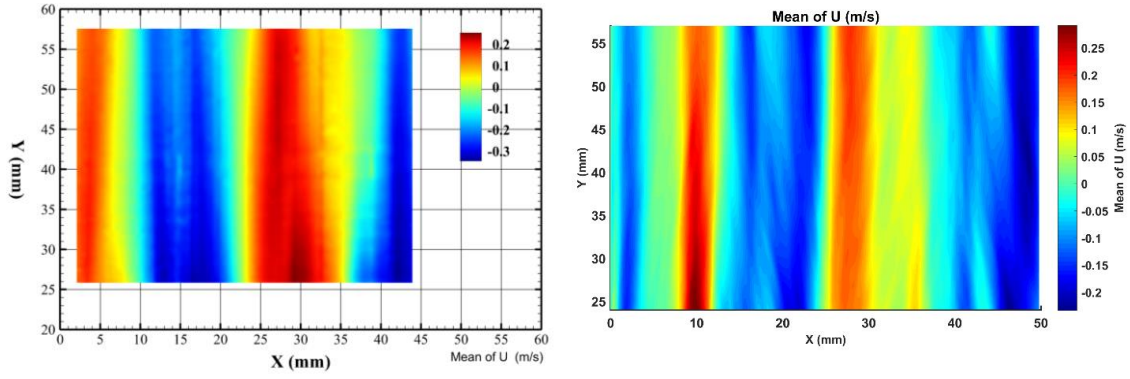

Figure 102: Time averaged U velocity from Exp. (left) and LES (right) on plane 1.

In Figure 103, time averaged V velocity component for the experiment and simulation are shown on plane 2. As it can be seen flow structures are captured in both experiment and numerical results. Specifically, the peak structure is captured in both experiment and simulation around 25 mm on horizontal line.

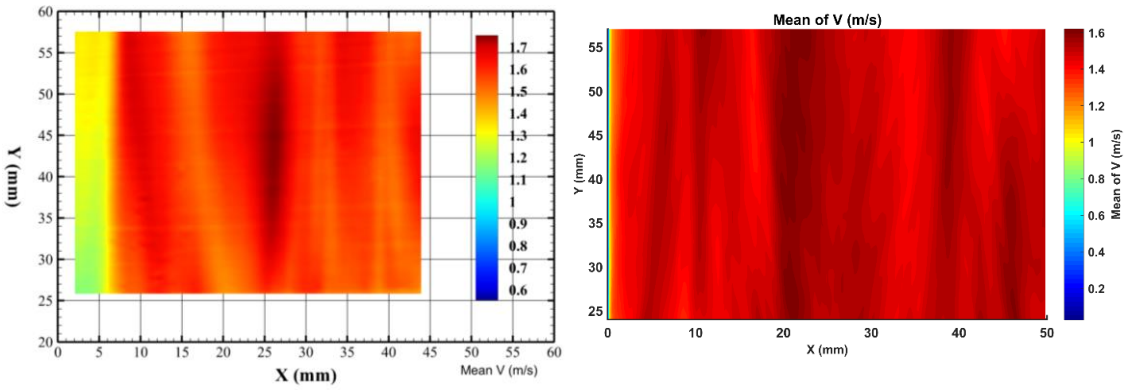

Figure 103: Time averaged V velocity from Exp. (left) and LES (right) on plane 2.

In Figure 104, time averaged W velocity component for the experiment and simulation are shown on plane 2. As it can be seen that flow structures are captured well in both experiment and numerical results. However the convergence of the experimental value is less than numerical results. Moreover columnar flow structures are a proof that LES is capable of capturing actual flow physics with higher resolution than experiment.

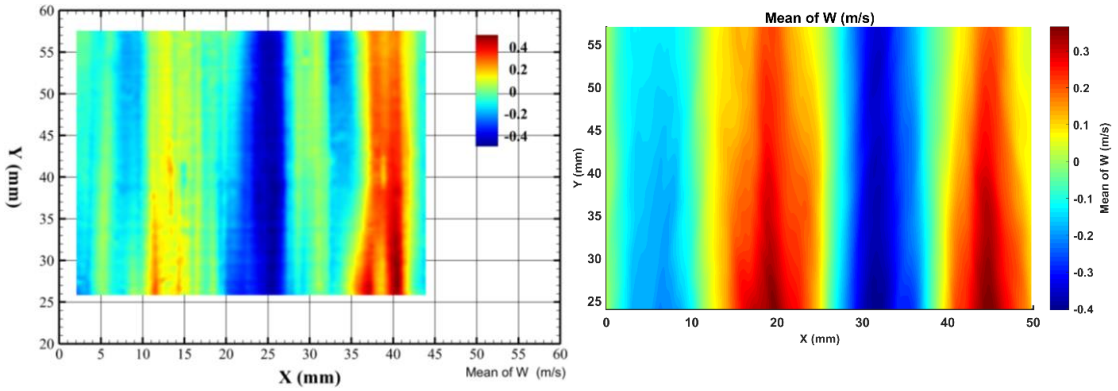

Figure 104: Time averaged W velocity from Exp. (left) and LES (right) on plane 2.

CHAPTER V

CONCLUSION

Chapter II describes a validation study using LES and the Dynamic Smagorinsky SGS model. Additionally, flow structures for the interaction of the buoyant jet and stratified layer is investigated by using numerical techniques such as POD, FFT and vortex identification. Additionally, it is the first LES study performed over a long time period for a transient situation of the type represented in containment level analyses.

The temporal numerical simulation results are compared against the PANDA experimental data for the velocity, temperature and helium concentration. All parameters are found to be in excellent agreement with the experimental results. FFT is applied to check whether enough turbulence scales are resolved in the simulation, with results showing that the inertial subrange is resolved and the grid resolution is sufficient.

After validating the local values using experimental data, more details about interaction of the buoyant jet and stratified layer is investigated by using a POD method. Kelvin-Helmholtz instabilities are captured and scalar POD modes of turbulent mass transfer structures are observed. In the second POD mode of gas concentration, it shows qualitatively similar behavior with buoyancy term, which is used as a source term for turbulent kinetic energy equation of the two-equation models. On the other hand, coherent structures of the vorticity show that most of the coherent vortices are created near jet exit due to shear layer and buoyancy force, while smaller energy vortices spread between jet and stratified layer. Vortices are analyzed further with Q-criterion and Lambda2 criterion

to check their structures. Horseshoe vortices are observed, which have been previously observed experimentally and numerically for buoyant jets.

In terms of computational cost, the LES simulation for such a large domain has been conducted successfully with reasonable amount of computational time by using a supercomputer facility. The LES simulation was performed with 600 cores by using 1.08 million CPU-hours. Specifically, in this study, physical simulation time is the main burden due to the longer transient time.

Finally, the present study focused on the validation study of PANDA experiment, which is a simplified version of a real containment accident scenario. The simplifications are done by considering a simpler geometry and neglecting the effect of the steam condensation. In addition to validation, the interaction of buoyant jet with stratified layer and its flow structures are analyzed. For future research, experimental simplifications could be neglected to analyze realistic accident scenarios.

In Chapter III, as state-of-art CFD simulations are becoming more available by growth of the computational power, sensitivity of models and sources of the uncertainties have to be quantified by using simple benchmark cases to reach higher fidelity multi-scale simulations. In present study effect of the turbulence models, and one of the non-dimensional parameter is analyzed, while the most of the models resulted in well agreement with experimental results, such as RSM, Spalart-Allmaras, and realizable k-ε, some other models showed more deviation than reality. In addition to that, present study shows that, different modeling approach requires different resolution of the mesh even with non-scale resolved models such as non-linear standard k-ε cubic model. Finally, the

general trend of the concentration of the two fluids were predicted very well for the simulations.

In Chapter IV, it is well known that complex structures of the mixing vane generate a strong flow mixing pattern. LES is able to capture all those flow mixing patterns with a compromise on the computational cost. Further high-fidelity experimental and computational data such as Reynolds stress and vorticity will be compared on different planes of the downstream of the mixing vane. Strategy has been presented to achieve higher fidelity CFD simulations for the 5x5 fuel bundle by using the latest state-of-the-art best practices for LES at a Reynolds number of Re=14 000. In the pre-process step, 5x5 bundle was modeled without the mixing vane to obtain fully developed profile to be used for the main simulation. In IV.3, FFT methodology was used to check numerical grid resolution to confirm that inertial subrange is resolved as LES requirement. In IV.4, LES simulation results are used to estimate lower order variables by averaging on the horizontal surfaces along the channel, such as pressure drop and secondary flow intensity. Those lower resolution results can be useful to verify low fidelity sub-channel codes or RANS type of simulations. In addition to low resolution results, Standard k-epsilon and LES results are compared line by line to show the capability and limitations of the two – equation models. The flow structures from LES simulations are plotted on vertical and horizontal planes for velocity magnitude, turbulent kinetic energy and secondary flow structures by using magnitude of lateral velocity components.

In IV.5, Proper orthogonal decomposition (POD) method is applied by using snapshot technique, coherent structures of the turbulent flow are extracted. Lower order

modes of the POD show the dissipation of larger eddies into smaller scale. The energy vs. mode is consistent with general technique behaviors. In IV.6, Dynamic mode decomposition (DMD) is applied for same purpose. Even though both POD and DMD are data reduction techniques, POD is only able to extract the most persistent spatial structures, while DMD is able to extract temporal evaluation of the structures. DMD results in modes with different energy distribution, and this allows to extract energy modes with higher resolution than POD.

In IV.7, the experimental results from stereoscopic-PIV and numerical results from LES are compared, while the velocity results and general structures of the flow are matched with good agreement, this wasn't the case for the second order statistics, possibly due to statistical convergence of the experimental snapshots. Experiences that were obtained in this study from CFD methodology and validation can be used to improve the CFD models currently used for PWRs.

REFERENCES

[1] Z. Liang, M. Sonnenkalb, A. Bentaib, M. Sangiorgi, Status Report on Hydrogen Management and Related Computer Codes, France, 2014.

[2] M. Andreani, K. Haller, M. Heitsch, B. Hemstrom, I. Karppinen, J. Macek, J. Schmid, H. Paillere, I. Toth, A benchmark exercise on the use of CFD codes for containment issues using best practice guidelines: A computational challenge, Nuclear Engineering and Design, 238(3) (2008) 502-513.

[3] D.C. Visser, M. Houkema, N.B. Siccama, E.M. Komen, Validation of a FLUENT CFD model for hydrogen distribution in a containment, Nuclear Engineering and Design, 245 (2012) 161-171.

[4] M.K. Fernandez-Cosials, G. Jimenez, E. Lopez-Alonso, Analysis of a gas stratification break-up by a vertical jet using the GOTHIC code, Nuclear Engineering and Design, 297 (2016) 123-135.

[5] M. Andreani, A. Badillo, R. Kapulla, Synthesis of results of the OECD-PSI blind benchmark exercise on erosion of a stratified layer by a buoyant jet in a large volume, in: OECD/NEA Workshop on CFD code Application to Nuclear Reactor Safety (CFD4NRS-5), ETH Zurich, Switzerland, 2014.

[6] F.S. Sarikurt, Y.A. Hassan, CFD Simulations of Erosion of a Stratified Layer by a Buoyant Jet in a Large Vessel, in: NURETH'16, Chicago, Illinois, 2015, pp. 1237-1250.

[7] F. Sarikurt, CFD Simulations of Erosion of a Stratified Layer by a Buoyant Jet in a Large Vessel, Texas A&M University, College Station,TX, 2015.

[8] J. Kim, E. Jung, S. Kang, Large eddy simulation of hydrogen dispersion from leakage in a nuclear containment model, Int J Hydrogen Energ, 40(35) (2015) 11762-11770.

[9] F.S. Sarikurt, Y.A. Hassan, Large eddy simulations of erosion of a stratified layer by a buoyant jet, International Journal of Heat and Mass Transfer, 112 (2017) 354-365.

[10] C.M. Lee, Y.D. Choi, Comparison of thermo-hydraulic performances of large scale vortex flow (LSVF) and small scale vortex flow (SSVF) mixing vanes in 17×17 nuclear rod bundle, Nuclear Engineering and Design, 237(24) (2007) 2322-2331.

[11] X. Li, Y. Gao, Methods of simulating large-scale rod bundle and application to a 17×17 fuel assembly with mixing vane spacer grid, Nuclear Engineering and Design, 267 (2014) 10-22.

[12] R. Zhang, T. Cong, W. Tian, S. Qiu, G. Su, CFD analysis on subcooled boiling phenomena in PWR coolant channel, Progress in Nuclear Energy, 81 (2015) 254-263.

[13] U. Bieder, F. Falk, G. Fauchet, CFD analysis of the flow in the near wake of a generic PWR mixing grid, Annals of Nuclear Energy, 82 (2015) 169-178.

[14] S.K. Kang, Y.A. Hassan, Computational fluid dynamics (CFD) round robin benchmark for a pressurized water reactor (PWR) rod bundle, Nuclear Engineering and Design, 301 (2016) 204-231.

[15] G. Chen, Z. Zhang, Z. Tian, X. Dong, Y. Wang, CFD simulation for the optimal design and utilization of experiment to research the flow process in PWR, Annals of Nuclear Energy, 94 (2016) 1-9.

[16] S. Cheng, H. Chen, X. Zhang, CFD analysis of flow field in a 5×5 rod bundle with multi-grid, Annals of Nuclear Energy, 99 (2017) 464-470.

[17] STAR-CCM+, STAR-CCM+ User Guide, 2015.

[18] M. Germano, U. Piomelli, P. Moin, W.H. Cabot, A Dynamic Subgrid-Scale Eddy Viscosity Model, Phys Fluids a-Fluid, 3(7) (1991) 1760-1765.

[19] J.L. Lumley, The structure of inhomogeneous turbulent flows, in: A. M. Yaglom, V.I. Tararsky (Eds.) Atmospheric Turbulence and Radio Wave Propagation Nauka, Moscow, 1967, pp. 166–178.

[20] L. Sirovich, Turbulence and the Dynamics of Coherent Structures .1. Coherent Structures, Q Appl Math, 45(3) (1987) 561-571.

[21] S.B. Pope, Turbulent Flows, Cambridge University Press, 2000.

[22] E. Studer, J. Brinster, I. Tkatschenko, G. Mignot, D. Paladino, M. Andreani, Interaction of a light gas stratified layer with an air jet coming from below: Large scale experiments and scaling issues, Nuclear Engineering and Design, 253 (2012) 406-412.

[23] M. Satish, F. Ma, M.R. Islam, Large eddy simulation of a three dimensional buoyant jet, Manuf Eng Div Asme, 16 (2005) 1321-1330.

[24] OECD/NEA CFD–UQ Benchmark Exercise: CFD prediction and Uncertainty Quantification of a GEMIX mixing layer test, ETH Zurich, Switzerland, 2015.

[25] A.M. Krueger, F.S. Sarikurt, Y.A. Hassan, Uncertainty Quantification by Monte Carlo Analysis using CFD Simulations for GEMIX Benchmark Activities, in: ANS Winter Meeting & Expo, ANS Transaction, Las Vegas, Nevada, 2016.

[26] F.S. Sarikurt, Y.A. Hassan, Sensitivity Analysis of RANS Modeling on GEMIX CFD Benchmark Study, in: ANS Transactions, San Francisco, California, 2017.

[27] F.S. Sarikurt, G. Busco, Y.A. Hassan, Toward High Fidelity LES Simulations of 5x5 PWR Fuel Bundle with Mixing Vane, in: ANS Annual Meeting, San Francisco, California, 2017.

[28] G. Busco, F.S. Sarikurt, Y.A. Hassan, A Non-Linear k- Turbulent Model Sensitivity Analysis for Flow Across a PWR Spacer Grid with Mixing Vanes, in: ANS Annual Meeting, ANS, San Francisco , California, 2017.

[29] P.J. Schmid, Dynamic mode decomposition of numerical and experimental data, J Fluid Mech, 656 (2010) 5-28.

[30] C.W. Rowley, I. MeziĆ, S. Bagheri, P. Schlatter, D.S. Henningson, Spectral analysis of nonlinear flows, J Fluid Mech, 641 (2009) 115.